


Topical Review

Advanced atomic force microscopies and their applications in two-dimensional materials: a review

Rui Xu¹, Jianfeng Guo¹, Shuo Mi¹, Huanfei Wen^{2,3}, Fei Pang¹, Wei Ji¹ and Zhihai Cheng^{1,*} 

¹ Beijing Key Laboratory of Optoelectronic Functional Materials & Micro-nano Devices, Department of Physics, Renmin University of China, Beijing 100872, People's Republic of China

² Key Laboratory of Instrument Science and Dynamic Testing, North University of China, Taiyuan 030051, People's Republic of China

³ Key Laboratory of Quantum Sensing and Precision Measurement, Institute of Instrument and Electronics, North University of China, Taiyuan 030051, People's Republic of China

E-mail: zhihaicheng@ruc.edu.cn

Received 14 July 2022, revised 12 August 2022

Accepted for publication 17 August 2022

Published 13 September 2022



Abstract

Scanning probe microscopy (SPM) allows the spatial imaging, measurement, and manipulation of nano and atomic scale surfaces in real space. In the last two decades, numerous advanced and functional SPM methods, particularly atomic force microscopy (AFM), have been developed and applied in various research fields, from mapping sample morphology to measuring physical properties. Herein, we review the recent progress in functional AFM methods and their applications in studies of two-dimensional (2D) materials, particularly their interfacial physical properties on the substrates. This review can inspire more exciting application works using advanced AFM modes in the 2D and functional materials fields.

Keywords: atomic force microscopy, advanced atomic force microscopy, two-dimensional materials, surface and interface

* Author to whom any correspondence should be addressed.



Original content from this work may be used under the terms of the [Creative Commons Attribution 4.0 licence](https://creativecommons.org/licenses/by/4.0/). Any further distribution of this work must maintain attribution to the author(s) and the title of the work, journal citation and DOI.

Future perspectives

Numerous advanced or functional atomic force microscopies have been developed and applied in various research fields, from mapping sample morphology to measuring physical properties. The research and development of AFM-based physical characterization methods require the researchers to have clear natural science concepts and electronic circuit knowledge. The future development direction of AFM-based modes includes the following points: (i) The single physical property measurement method has limitations because the electrical properties are coupled with other properties. Therefore, a method that can explore the mechanical-thermal-electrical-optical coupling is needed. (ii) The functional AFM technology under vacuum conditions needs further improvement. (iii) Optimizing device performance requires understanding the properties of materials under work conditions. A method that can measure physical properties under work conditions is crucial for future research.

1. Introduction

Investigations at the nano or atomic scale are necessary to understand material properties fundamentally. Scanning probe microscopy (SPM) allows direct characterization and construction of structures at the nano and atomic scales [1–4]. In addition, numerous advanced or functional SPM methods, including atomic force microscopy (AFM), have been developed and applied in various research fields [5–8]. SPM detects the near-field interactions between the local probe (or tip) and sample surfaces, such as current and forces, depending on the probe-sample distance and their physical properties (figure 1).

1.1. Scanning tunneling microscopy (STM)

The first kind of scanning probe microscopy, the scanning tunneling microscope, was invented in 1981/1982 by Binnig and Rohrer [3, 4, 9] who went on to receive the 1986 Nobel Prize in physics. STM works using the tunneling effect of quantum mechanics, which states that even if the electron energy is lower than the barrier height, it has a certain probability of passing through the barrier. If the voltage between the tip and sample surface is minimal, we can obtain the exponential dependence of the tunneling current (I) on the tip-sample distance (z), as follows.

$$I \propto V \rho_s(E_F) e^{-2kz}, \quad (1)$$

where ρ_s is the electronic density of states of sample, and $k = \sqrt{2m\varphi}/\hbar$, φ is the work function of the sample. The main characteristic of tunneling current is the exponentially decaying with the tip-sample distance. This exponential dependence causes the extremely high vertical resolution of the STM, which can reach the picometer regime.

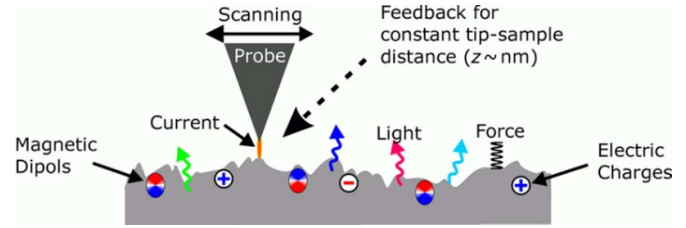


Figure 1. Interactions between the scanning probe microscope probe and the sample surface.

1.2. Atomic force microscopy (AFM)

One disadvantage of STM is that it can be used only on conducting samples as the tunneling current is the measured quantity. Instead of the tunneling current in STM, the ubiquitous interactions/forces between the tip and sample are measured in AFM [10]. AFM can be used on conductor, insulators, semiconductors, polymers, and biology cells.

A qualitative sketch of the force between the tip and sample is given as a function of the tip-sample distance (figure 2(a)). Three different regimes can be distinguished. If the tip is far away from the surface, the force between the tip and sample is negligible. An attractive (negative) force between the tip and sample occurs for closer distances, marked by blue color. For very small distances, a strong repulsive force exists between the tip and sample, marked by the red line.

There are three basic AFM working modes, which are primarily used to obtain the surface topography. The first mode is contact mode (figure 2(b)), which is a static mode. In this mode, the tip contacts the sample surface during scanning, and the interaction force between them is the repulsive force, which is measured by the cantilever deflection signal. The z -feedback loop maintains a constant force between the tip and sample. The corresponding changes in the z -position for maintaining a constant tip-sample distance (i.e. constant force) correspond to the sample surface topography.

The second mode is the amplitude modulation (AM) mode, also known as the Tapping mode (figure 2(c)), which is different from the static mode. The AM mode is a dynamic mode, and the feedback loop is the oscillation amplitude of the AFM probe. Herein, the micro cantilever is forced to vibrate, and the frequency ω_{drive} is its free resonance frequency. When the tip and sample approach each other, the oscillation amplitude at the fixed excitation frequency ω_{drive} will change. The preamplifier converts the deflection signal from the photodiode to a voltage signal proportional to the cantilever deflection. The AC voltage signal has a frequency ω_{drive} and amplitude proportional to the oscillation amplitude of the vibrating cantilever. Using a lock-in amplifier, the amplitude of the AC signal at frequency ω_{drive} is measured. Moreover, maintaining a constant oscillation amplitude corresponds to maintaining a constant tip-sample distance. Thus, the z -feedback signal is used as the height signal to map the topography during data acquisition.

The third mode is the frequency modulation (FM) mode, also called non-contact dynamic mode (figure 2(d)) [11]. In this mode, the resonance frequency shift is measured due to the

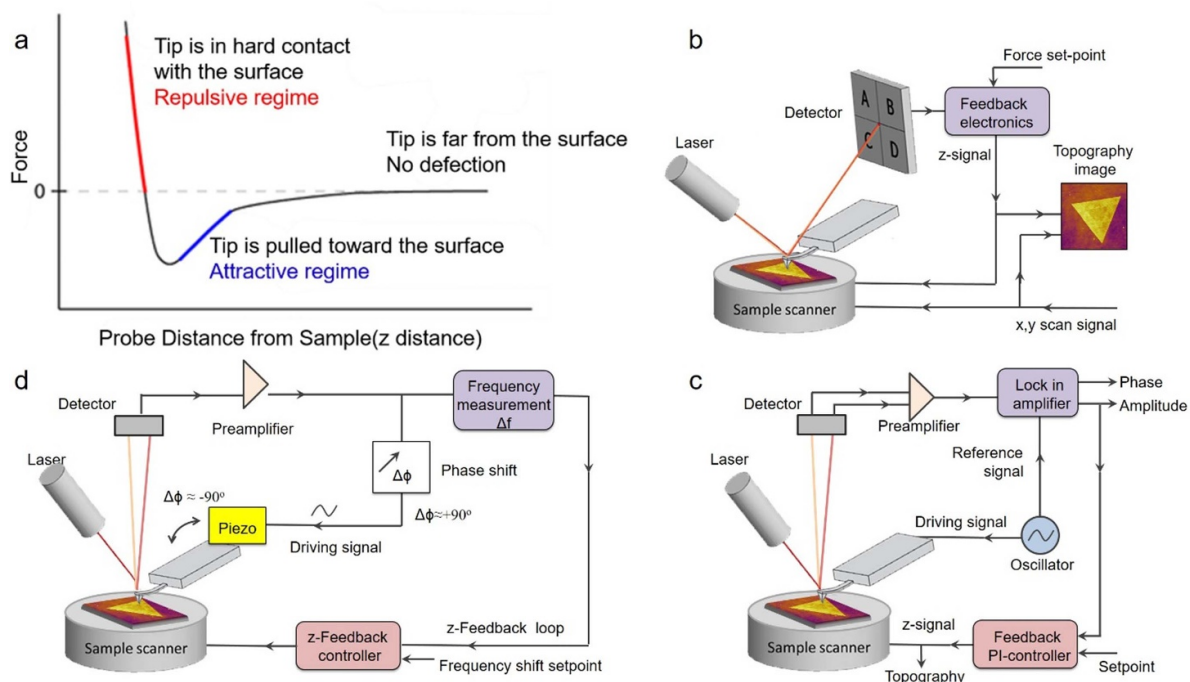


Figure 2. (a) Qualitative behavior of the force between tip and sample as a function of tip–sample distance. (b) and (c) Schematics of atomic force microscopy (AFM) operation: (b) contact mode (static mode), and (c) amplitude modulation mode in dynamic mode. (d) Schematic of frequency modulation detection setup operated in the self-excitation mode. Non-contact AFM.

tip–sample interactions. The z-feedback loop maintains a constant frequency shift of the cantilever resonance frequency as the setpoint. A schematic of the implementation (figure 2(d)) consists of an oscillator loop, to which the measured oscillation signal is fed back (after a phase shift) as the driving signal of the cantilever. Please see details in [1].

1.3. AFM probes

For sensing normal tip–sample forces, the force sensor should be rigid in two axes and relatively soft in the third axis. This property is fulfilled with a cantilever beam. The first cantilevers were made from a gold foil with a small diamond tip attached to it. Later, silicon micromachining technology was employed to build cantilevers in parallel production with well-defined mechanical properties. The first micromachined cantilevers were built at Stanford in the group of Calvin F. Quate. Initially, mass-produced cantilevers were built from SiO_2 and Si_3N_4 . Later, cantilevers with integrated tips were machined from silicon-on-insulator wafers. The most common cantilevers in use today are built from all-silicon with integrated tips pointing in a [001] crystal direction. Figure 3(a) shows the type of cantilevers that are mainly used today: micromachined silicon cantilevers with integrated tips.

In dynamic atomic force microscopy, some requirements for the force sensor are similar to the desired properties of the time-keeping element in a watch: utmost frequency stability over time and temperature changes and little energy consumption. Around 1970, the watch industry was revolutionized with the introduction of quartz tuning forks as frequency standards in clocks. Experimental studies of using

quartz-based force sensors were carried out soon after the invention of the AFM. Tuning forks were used as force sensors in acoustic near-field microscopy, scanning near-field-optical microscope. Figure 3(b) shows a quartz cantilever based on a quartz tuning fork [12]. In contrast to micromachined silicon cantilevers, the quartz forks are large. Hence a wide selection of tips can be mounted on a tuning fork with the mere help of tweezers and a stereoscopic microscope—sophisticated micromachining equipment is not needed.

The tip apex, which is the key sensing element, must be small for the highest spatial resolution. Nowadays, with a CO-functionalized tip attached to a quartz tuning fork sensor, the high resolution structure of 2D materials have been obtained, which provides support for in-depth understanding physical properties of new materials [13–15].

Although CO-functionalized tip was ultrathin and has high resolution, it still not an ideal tip. An ideal tip would be a sharp spike, such as a column of single atom width and infinite length. However, even this is not ideal, considering the force would act on the entire column in addition to the apex atoms. An ideal tip would consist of an isolated atom or a cluster of atoms, which is not realistic.

A more typical tip for basic AFM imaging is usually a cone or pyramid (table 1 and figures 3(a) and (b)), with an apex ratio between 1:4 and 1:10. The tip is a rounded tip, usually approximated by a sphere with a radius of 5–20 nm. The probe is typically made of silicon (figures 3(a)–(c)) or silicon nitride (figure 3(d)) using methods typical for micro-fabrication, including lithography, sputtering, anisotropic etching, or focused ion beam milling. Probes can

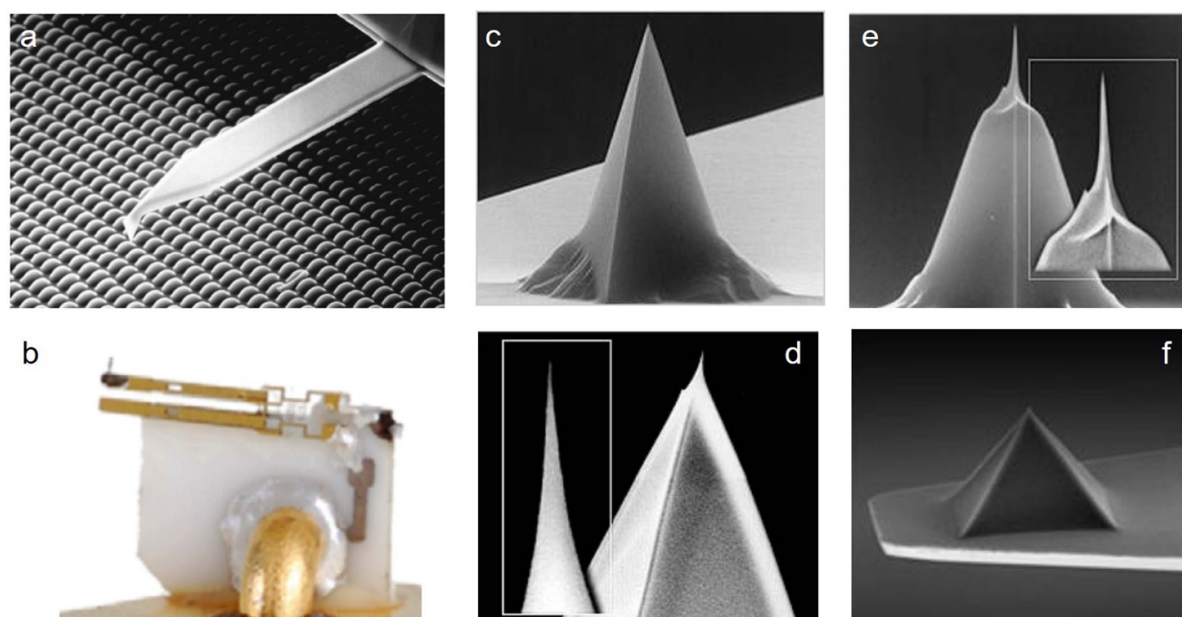


Figure 3. (a) Scanning electron microscopy (SEM) image of a micromachined silicon cantilever with an integrated tip pointing in the [001] crystal direction. (b) Micrograph of a ‘qPlus’ sensor—a cantilever made from a quartz tuning fork [12]. (c)–(f) SEM images of some typical commercial AFM probes: (c) Silicon probe suitable for contact mode. (d) Super sharp silicon probe, suitable for non-contact and tapping modes. (e) High aspect ratio tip. (f) Pyrex-nitride probe. (NanoWorld & PointProbe AFM tip). Reproduced from [12]. © IOP Publishing Ltd. All rights reserved.

Table 1. Dimensions of typical tips. Reproduced from [16]. © IOP Publishing Ltd. All rights reserved.

	Radii of apex (nm)	Cone half-angle ($^{\circ}$)	Length (μm)
Silicon tip	7	<10	10–15
Super sharp silicon tip	2	<10 at last 200 nm of tip	10–15
FIB	<15	<3	>1.5
EBD	~10	~4	up to ~5

be modified by doping and coating thin films to enhance the contrast of a particular analytical method. Figure 3 shows the SEM images of some typical commercial AFM tips. The high aspect ratio tip (figure 3(c)) is suitable for performing measurements on samples with a sidewall angle approaching 90° . The tip has an overall height of 10–15 μm , which allows for measuring highly corrugated samples. At the last few micrometers, the tip exhibits a high aspect ratio portion that is symmetric when viewed from the side and along the cantilever axis. The tip radius is typically 10 nm. The pyrex-nitride probe (figure 3(d)) is hydrophobic and used for biological sample detection.

Cantilevers have been made from silicon and silicon nitride. However, in some cases other materials, such as diamond with outstanding mechanical properties, have been used to obtain specific cantilever and tip properties (table 2).

Two important properties of the cantilevers are their free resonant frequency (f_0) and spring constant (k). Determining the cantilever resonant frequency is straightforward using resonance tuning. However, the determination of the cantilever spring constant is relatively complicated. Currently, the commercial AFM (Asylum Research) provides thermal tune method to quickly determine the f_0 and k of each probe. The resonance frequency range of common probes is listed

figure 4, which provides a reference for probes selecting in the experiments.

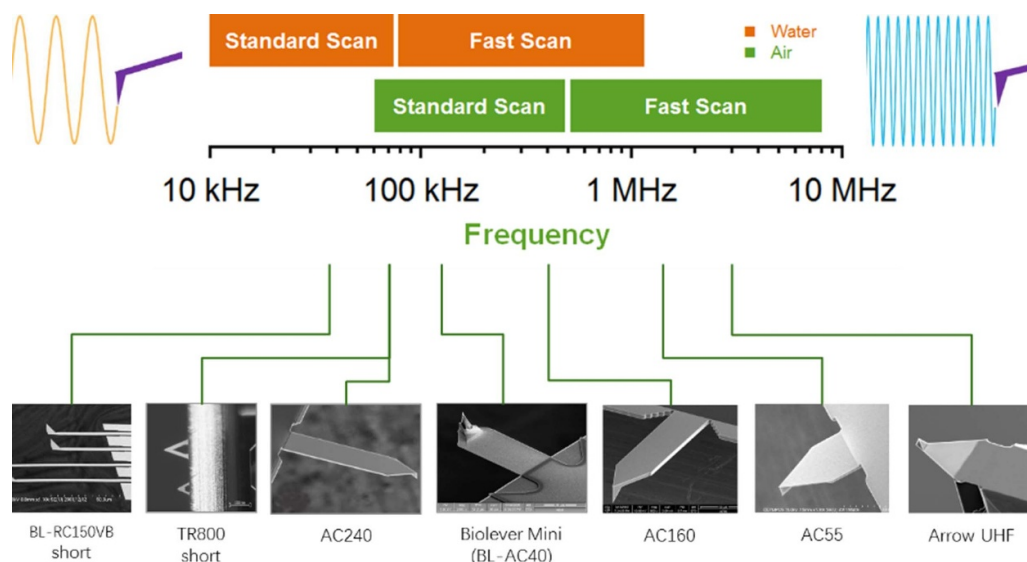
Different from the above basic modes, much more complex AFM probes are needed in the functional AFM modes, like scanning thermal microscope (SThM), scanning near field optical microscopy (SNOM), scanning microwave impedance microscopy (sMIM) and so on. In the following section 1.4, we will introduce probes appropriate for each advanced AFM methods.

1.4. Multi-functional AFM

Numerous multi-functional AFM-based techniques have been developed to characterize the local mechanical properties, electrical properties, optical characteristics and thermal properties of the sample. The methods include the scanning Kelvin probe microscopy (SKPM) and electrostatic force microscopy (EFM) for the surface potential (SP) and electrostatic potential measurement, dual AC mode and contact resonance (CR) mode for the contact stiffness and viscous response detection, scanning thermal microscope (SThM) for the thermal response, and SNOM for the photonic optical characteristics detection. Several typical AFM-based techniques and their applications are presented in table 3.

Table 2. Physical properties of some common materials used for AFM cantilevers. Reproduced from [16]. © IOP Publishing Ltd. All rights reserved.

Material property	Si (001) [a]	Si ₃ N ₄	GaAs (001) [b]	Quartz [c]	Diamond	Al [d]	Polyimide
Mechanical							
Density (g cm ⁻³)	2.329	3–3.3	5.317	2.6	3.5	2.7	1.43[d]
Young's modulus (Gpa)	168.4 for [110] 129 for [100] 80	260–320 [f]	121.5 for [110] 85.5 for [100] 60	73.1 for [110]	1163.6 for [110] 1050.3 for [100] 10 300	27.8	3.0–3.2[d]
Torsional modulus <i>G</i> (Gpa)				31.2			
Poisson ratio	0.27[b]	0.25[f]		0.17[f]	0.1–0.29[f]	0.34	0.41[d]
Hardness (load g ⁻¹)	1150(25)		680(100)		6360 (long)		
Speed of sound <i>v_s</i> (m s ⁻¹)	8430 (long) [b]	9900[c]		5980[d]	17.520[d]	6.360	
Thermal							
Thermal expansion coefficient (μm K ⁻¹)	2.92[b]	2.5–3.3[b]	6.86	0.54	1.0	23.03	50–60[b]
Heat capacity <i>c_p</i> (J kg ⁻¹ K ⁻¹)	700	45.8 J mol ⁻¹ K ⁻¹ [b]	500	670	518	880	
Heat Conductivity (kW ⁻¹ mK ⁻¹)	156[b]	15–45[b]	45.5	1.46	600–2000	237	0.29–0.35[b]
Melting point <i>T_m</i> (K)	1687[b]	1800–1950 [b]	1513		4100[b]	933.47	335–345[b]
Optical and electrical							
Refractive index <i>n</i> at 633 nm	3.4		3.878	~1.46	5.7		
Static dielectric constant <i>ε</i>	11.97[b]		13.18	3.8	5.70[b]		3.4[b]
Gap energy (eV)	1.12(ind.)		1.42	9	10 ¹⁷		
Electrical resistivity <i>ρ</i> (Ωm)	10 ³		10 ⁹ (undoped)	7 × 10 ⁹			

**Figure 4.** Resonance frequency range of probes (Asylum Research).

1.4.1. Friction force microscopy and transverse shear microscopy. FFM and TSM are the derivatives of the contact mode of AFM. They maintain the normal force constant and record the lateral signal between the tip and sample surface (figure 5) [18, 19, 66–68]. The lateral bending or twisting

arises from forces parallel to the sample surface plane and acting on the AFM-tip. In TSM, the scanning direction of a force microscope probe tip is parallel to the cantilever axis, and the lateral deflection or twist of the cantilever is recorded. This mode of operation differs from the better-known FFM

Table 3. AFM Techniques and their Applications.

AFM modes	Signal of detection	Measurement of physical quantity
LFM/FFM	Friction force	Strain domain and strain structure [17]
TSM	Transverse shear force	Crystallographic orientation [18, 19]
Dual AC mode	Amplitude (A_2) and phase (P_2) Response of second mode	Viscous response detection [20]
Multi-harmonic -AFM	Higher harmonic components introduced by the nonlinearity of the tip-sample interaction forces	Interlayer coupling [7] and local variations of the elastic modulus [7, 20]
CR mode	Contact resonance frequency and quality factor	Contact stiffness and viscous response detection [21]
C-AFM	Current	Local conductivity [22–25]
SKPM/KPFM	Electric potential	Surface potential (SP) [26], work function [27], contact potential difference [28], charge transfer [29, 30], surface point defect/adsorbate [31–33], voltage drop [34], and capacitance coefficients [35], Capacitance coefficients [35], SP [36], and dielectric response [37]
EFM	Electrostatic forces	SP [38], work function [39], and mobile charge carriers (MCC) [40]
MH-EFM	Electrostatic forces	Dielectric constant [41, 42], conductivity and permittivity variation [43, 44], charge carrier variations [45], and doping concentration [46]
sMIM	Microwave reflection	Electromechanical response [47, 48], piezoelectric properties [49], and ferroelectric coercive field [50]
PFM	Electromechanical coupling	Image flux lines in superconductors, local detection of magnetic interactions to eddy currents, and magnetic dissipation phenomena [51]
MFM	Near-field magnetostatic interaction	Subsurface defects in solids and dopant distributions in semiconductors [52]
MRFM	Magnetic resonance signals	Mechanical–thermal coupling effect [53]
SThM	Thermal resistance	Magnetic fields [54–57], magnetic textures [58], spin relaxation [59], charge-state control [60], microwave fields imaging [61], living cell temperature imaging [62]
NV center combined AFM	Magnetic signals, electric signals	IR absorption spectra of nanoscale regions, sample temperature increase, distribution of chemical species [63]
AFM-IR	Thermal expansion	Distribution of the electromagnetic radiation [64]
SNOM	Near field optical signal	Molecular vibrational spectra, infrared absorption spectrum of organic samples [65]
Nano-FTIR	Near field optical signal	

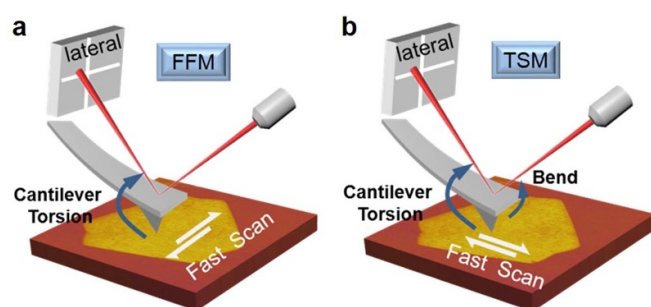


Figure 5. Sketch map of (a) friction force microscopy (FFM) and (b) transverse shear microscopy (TSM). For FFM (TSM), the scan direction of the AFM tip is perpendicular (parallel) to the long axis of the cantilever. The friction (shear) property of the sample is obtained by detecting the cantilever torsion signal.

or lateral force microscopy (LFM) technique in that the scanning direction is perpendicular to the cantilever axis in the FFM/LFM technique [68].

Comparing to FFM/LFM, TSM has enhanced sensitivity to elastic deformation properties and can reveal crystallographic orientation. Owing to the flexibility of 2D materials, friction

can easily drive stretch deformation, leading to in-plane mechanical (shear stiffness) symmetry breaking. In another word, the shear stiffness with uniaxial strain has significant lattice dependent anisotropy, especially for 2D atomic crystals with centrosymmetric structures. Based on normal tension strain-induced shear anisotropy, we have reported that the visualization of crystallographic-orientation-dependent shear deformations in flexible, hexagonal 2D atomic crystals by using TSM. (See details in figure 4 in [18].)

1.4.2. Multi-harmonic and dual AC mode. Conventional dynamic AFM methods focus on the excitation and detection of a single frequency component of the tip motion, usually at the fundamental resonant frequency. Information on sample properties included in other frequency components, such as harmonics, is irreversibly lost, which limits the capabilities of the AFM [5]. High harmonics have been recognized, but their utilization has been limited due to theoretical and experimental complexity [69, 70]. Hence, developing multi-frequency AFM (MF-AFM) technology is imperative, based on simultaneous excitation and/or detection of several frequencies of the probe's oscillation [71, 72].

In conventional AM AFM, the cantilever deflection is given as

$$z = z_0 + A \cos(\omega t - \phi), \quad (2)$$

where A , z_0 , and ϕ are the amplitude, static deflection component, and phase shift with respect to the driving force, respectively. Owing to the presence of multifrequency components (harmonics) introduced by the nonlinear interaction between the tip and sample, the deflection of the cantilever is as follows.

$$z = z_0 + \sum_{n=1}^N A_n \cos(n\omega t - \phi_n), \quad (3)$$

where A_n is the amplitude of the harmonic with angular frequency $n\omega$. Equations (2) and (3) are compatible with a point-mass description of the cantilever. A more precise description is achieved by considering the extended characteristics of the cantilever, with the probe deflection containing contributions from all its eigenmodes (q_j),

$$z = z_0 + \sum_{j=1}^M q_j(t) = z_0 + \sum_{j=1}^M A_n \cos(n\omega t - \phi_n). \quad (4)$$

In equation (4) the eigenmodes have been expressed in terms of the different harmonics (A_n).

For multi-harmonic mode, the amplitude of higher harmonics can be expressed as

$$A_n = S \frac{\omega_0}{k} \sqrt{\left(\int_0^T F_{ts}(d) \cos(n\omega t) dt \right)^2 + \left(\int_0^T F_{ts}(d) \sin(n\omega t) dt \right)^2}. \quad (5)$$

For Q values greater than 5 and $\omega = \omega_0$,

$$S \approx \frac{1}{\pi n^2}, n > 3 \quad (6)$$

where F_{ts} represents the tip-surface force; d is the instantaneous tip-surface separation; and ω_0 is the fundamental resonant frequency.

For dual AC mode, the instantaneous tip position z when interacting is described approximately by equation (7), which neglects the contribution of the other modes and harmonics

$$z = A_1 \cos(\omega_1 t - \phi_1) + A_2 \cos(\omega_2 t - \phi_2), \quad (7)$$

where A_1 , ϕ_1 , and A_2 , ϕ_2 are the oscillation amplitudes and phase shifts at ω_1 and ω_2 , respectively. Thus, the total energy dissipated per cycle E_{dis} can be approximated as the sum of the two eigenmodes

$$E_{dis} \approx E_{dis}(1) + E_{dis}(2) = \frac{\pi k_1 A_{01} A_1}{Q_1} \left[\sin(\phi_1) - \frac{A_1}{A_{01}} \right] + \frac{n\pi k_2 A_{02} A_2}{Q_2} \left[\sin(\phi_2) - \frac{A_2}{A_{02}} \right], \quad (8)$$

where Q_i , k_i , and A_{0i} are the quality factor, force constant, and free amplitude of the i th eigenmode, respectively. The second eigenmode frequency is 6.27 times the first eigenmode frequency, i.e. $n = 6.27$. Equation (8) links the second modal observables, such as A_2 , with nonconservative interactions (E_{dis}).

The schematics of the multi-harmonic AFM and dual AC modes are shown in figures 6(a) and (b), respectively. The typical AFM probes used in dual AC and multi-harmonic AFM mode measurements are shown in figures 6(c)–(f). In multi-harmonic mode, a special harmonic cantilever is fabricated for tuning of its second eigenmode, to six times the first eigenmode to increase the signal to noise level, as shown in figure 6(c). In dual AC mode, the silicon AFM probes (AC240, Asylum Research) (figure 6(e)), having first resonance mode f_{r1} of ~ 76.3 kHz and second resonance mode f_{r2} of ~ 451.4 kHz are used.

High harmonic supports the research on cantilever's dynamic behaviors with high compositional sensitivity and atmospheric resolution. Expressing the tip-sample interaction as a function of high harmonic amplitude or frequency has several advantages. First, the high harmonic method can provide more details and intrinsic characteristics of the sample because it depends on the nonlinear interaction and is measured with zero references. Second, it allows a high spatial resolution, particularly with small oscillation amplitude and low bandwidth reduction [74, 75]. Thus, scanning with a relatively appropriate speed is possible by combining the small-amplitude higher-harmonic AFM with the resonance-enhancement technique. Third, high harmonic can be joined with other MF-AFM methods to develop interesting applications. Measurement innovations facilitate developing AFM and nanoscience. The high harmonic dynamic AFM will be attractive to nano- and pico-analytics in future physics, chemistry, biology, and materials science.

1.4.3. Contact resonance (CR) mode. The CR mode is an advanced AFM technique that measures the resonance peak of the probe and sample system. It offers improved nanomechanical characterization of layered materials compared to the existing techniques [76]. CR-AFM is achieved by introducing a slight vertical modulation to either the cantilever base [77] or sample [78, 79]. The cantilever CR frequency (CRF) and quality factor (Q) change in response to the viscoelastic properties of the sample when the tip is in contact with the sample. It can quantitatively characterize the viscoelastic response of materials with high sensitivity and large dynamic detection range because of the high-frequency operation and resonance enhancement effect [80, 81]. In this study, the detection limit of AFM used was approximately 10 pm; therefore, the excitation amplitude of the tip-sample contact was reduced to the picometer level, i.e. considerably smaller than the interlayer distance of two dimensional (2D) layered materials.

Figure 7 shows the schematic and mechanical model of CR-AFM and related definitions and characterizations for quantitative analysis. CR-AFM is based on the typical contact mode imaging method; the key is the vertical modulation with a

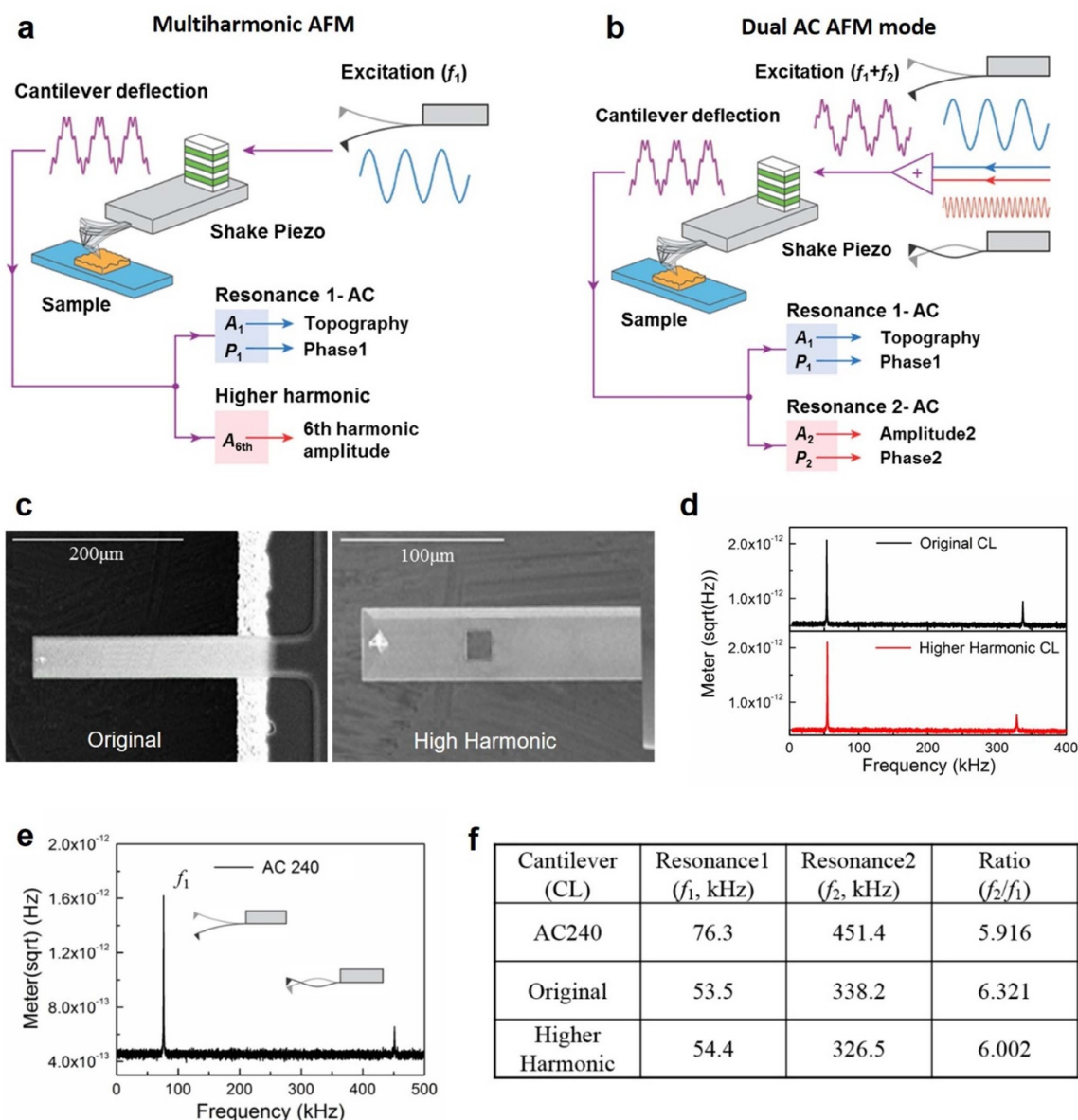


Figure 6. (a) Schematic of the multi-harmonic AFM mode. Recording higher harmonic components introduced by the nonlinearity of tip-sample interaction forces during conventional dynamic AFM imaging while driving the cantilever at its first resonance mode. (b) Schematic of the dual AC AFM mode. The cantilever is simultaneously driven at two eigenmodes (resonant modes), and the amplitude and phase are recorded. (c) SEM images of the original and 6th harmonic probes. (d) Frequency response spectroscopy of the original and 6th harmonic cantilever obtained with the thermal noise spectrum measurement. (e) Frequency response spectroscopy of the AC240 probe obtained with the thermal noise spectrum measurements. (f) Resonance frequencies of the three AFM probes at the first and second resonance mode. Reproduced from [73], with permission from Springer Nature.

slight amplitude introduced to the sample, as illustrated in figure 7(a). The modulation is operated at a high frequency and hence does not affect the contact-feedback imaging; however, the modulation can be coupled to the cantilever deflection that can be extracted for detection. The high-frequency signal is continuously changing with the sample mechanical properties as the tip scans the sample in contact mode, detected by a lock-in amplifier and referred to as CRF and CR amplitude (CRA). Figure 7(b) depicts the mechanical model of the tip-sample dynamic contact in CR-AFM. Because the tip location on the

cantilever directly affects the final measurement, the cantilever is modeled as a distributed mass with spring constant k_L rather than a point-mass approximation. The tip location is considered as a relative position $\gamma = L_1/L$ (with $0 \leq \gamma \leq 1$) from the clamped end. The tip-sample interaction is considered as normal elastic and dissipative (damping) forces, modeled as a spring and dashpot in parallel (i.e. Kelvin-Voigt model). The variables k^* and c indicate the contact stiffness and damping, respectively. The tip-sample stiffness and damping variations are reflected in the CRF and Q of the coupled system, which

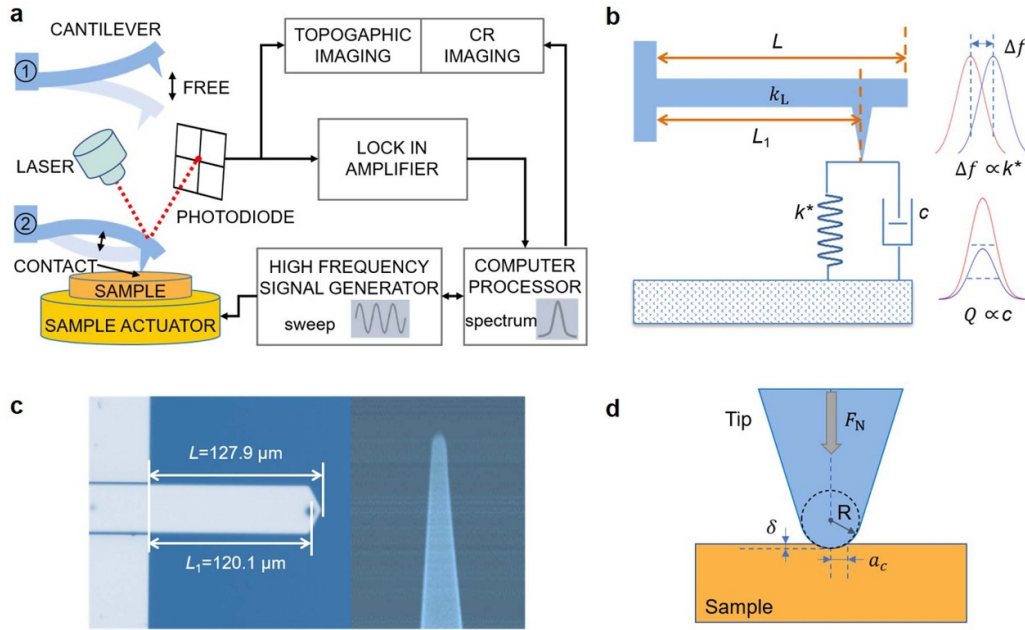


Figure 7. Schematic and mechanical model of contact resonance atomic force microscopy (CR-AFM) and related definitions and characterization of the cantilever used in the experiments for quantitative analysis. (a) Schematic of the CR-AFM experimental setup. (b) Tip–sample contact is modeled as a Kelvin–Voigt mechanical equivalent, where the spring and dashpot represent the contact stiffness (elastic modulus) and viscoelasticity (dissipation), respectively. (c) Close-up view of the tip–sample contact and definitions for quantitative characterization. (d) SEM characterization of the AFM cantilever and tip. Reproduced from [76], with permission from Springer Nature.

can be converted to the sample elastic and loss moduli with right contact mechanic models, respectively. Higher contact stiffness indicates high CRF, and larger viscosity (dissipation) at the tip–sample contact indicates low Q .

Consideration of the cantilever dynamic model is primarily based on the Euler–Bernoulli beam theory. The contact stiffness k^* is calculated using the cantilever stiffness, relative tip position, and resonance wavenumber [21], as described in equations (9)–(12). The relative tip position γ is characterized by SEM, as shown in figure 7(d),

$$\gamma = \frac{L_1}{L} = \frac{120.1}{127.9} = 0.939. \quad (9)$$

The parameter A_n , related to the wavenumber $x_n L$ of the cantilever resonance in free space, is defined by

$$A_n^2 = \frac{(x_n L)^2}{f_n^0}. \quad (10)$$

The wavenumber is denoted as $y_n L$ under the tip–sample coupling condition:

$$y_n L = A_n \sqrt{f_n^{\text{CR}}}. \quad (11)$$

Based on the equations (9)–(11), the contact stiffness k^* can be determined as:

$$k^* = \frac{2}{3} k_L (y_n L \gamma)^3 \frac{1 + \cos y_n L \cosh y_n L}{D}, \quad (12)$$

where

$$D = [\sin y_n L (1 - \gamma) \cosh y_n L (1 - \gamma) - \cos y_n L (1 - \gamma) \sinh y_n L (1 - \gamma)] [1 - \cos y_n L \gamma \cosh y_n L \gamma] - [\sin y_n L \gamma \cosh y_n L \gamma - \cos y_n L \gamma \sinh y_n L \gamma] \times [1 + \cos y_n L (1 - \gamma) \cosh y_n L (1 - \gamma)]$$

The wavenumber $x_n L$ for the flexural mode n is the solution of the characteristic equation $1 + \cos x_n L \cosh x_n L = 0$ for cantilever vibration in free space; the first two roots $x_1 L$ and $x_2 L$ are 1.8751 and 4.6941, respectively.

Using the contact stiffness, the sample modulus can be extracted quantitatively based on contact mechanic models [21], such as the Hertzian (Hertz) contact, Derjaguin–Muller–Toporov (DMT), and Johnson–Kendall–Robert (JKR) models. The two frequently used models in CR-AFM are the Hertz and punch contact models, which depend on the shape of the tip (sphere or punch) [21]. The discussion here is restricted to the Hertz and DMT models as a spherical tip is used in all experiments. The main difference between the two models is the consideration of the adhesion force F_{ad} . Figure 7(c) depicts the Hertz contact of the sphere tip and sample and defines the related quantities (F_N , R , a_c , and δ). The normal contact stiffness of the tip–sample system can be expressed by equation (13), which is related to the contact radius a_c and reduced Young’s modulus E^* .

$$k = 2a_c E^*, \quad (13)$$

$$E^* = \left(\frac{1}{E_t} + \frac{1}{E_s} \right)^{-1}, \quad (14)$$

$$a_c = \left(\frac{3F_N R}{4E^*} \right)^{1/3}, \quad (15)$$

where E_s and E_t are Young's moduli of the sample surface and AFM tip, respectively.

When F_{ad} is considered in the measurement, the DMT model is more accurate. The contact radius a_{DMT} is modified as

$$a_{DMT} = \left(\frac{3(F_N - F_{ad})R}{4E^*} \right)^{1/3}. \quad (16)$$

Finally, the elastic modulus of the test sample is determined from the experimental values of the contact stiffness using equations (16) and (17).

$$E^* = E_{cal}^* \left(\frac{k_{test}^*}{k_{cal}^*} \right)^{-1}. \quad (17)$$

The indentation can be deduced from the DMT model and is described as equation (18),

$$\delta = \frac{3(F_N - F_{ad})}{2k^*}. \quad (18)$$

In regard with the CR-AFM, dual AC resonance tracking, invented by Asylum Research [82], is an exclusive implementation of the CR. It tracks the CR (f_0) by adjusting the two drive frequencies (f_1, f_2) of the cantilever to zero difference amplitudes ($A_2 - A_1 = 0$) by reducing the crosstalk, rather than using the phase as frequency feedback.

1.4.4. Scanning kelvin probe microscopy (SKPM). SKPM is a well-known AFM mode invented by Nonnenmacher and Oboyle [83] for high spatial resolution SP mapping [84]. This technique is also called scanning SKFM [85], KPFM [84], and SKM [86]. Recently, it has been used to investigate the local SP of 2D materials [30, 87–92].

The work function φ and V_{CPD} are significant parameters for understanding the working principle of SKPM. Herein, φ is defined as the energy difference between the Fermi energy and vacuum level (figure 8), and V_{CPD} is defined as the difference in the φ of two materials, as:

$$\varphi_{sample} - \varphi_{tip} = \Delta\varphi = V_{CPD} \cdot e \quad (19)$$

where e is the electric charge; and φ_{sample} , and φ_{tip} are the work function of the tip and sample, respectively.

Figure 8 shows the energy level of the tip and sample surface with no electrical connection. The vacuum levels are related, but Fermi levels are dissimilar. Equilibrium needs Fermi levels to line up at a stable state if the tip-sample is sufficiently close for electrical contact. The Fermi energy level will align by electron current flow and the system will accomplish an equilibrium state (figure 8(b)). If the applied V_{DC} has a similar magnitude as V_{CPD} but with a reverse sign, the applied voltage eliminates F_{el} (figure 8(c)). Thus, when the tip work

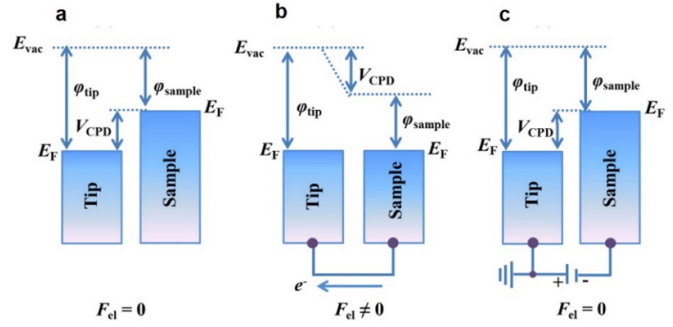


Figure 8. Electronic energy levels between the AFM tip-sample demonstrating the working principle of scanning Kelvin probe microscopy. (a) Tip-sample are separated by a distance d with no electrical contact due to the equal E_{vac} but different E_F level. (b) Tip-sample are in electrical contact and electron transfer from the sample with higher E_F to the one with lower E_F . (c) DC voltage V_{DC} applied between tip-sample readjusts the vacuum level. Reproduced from [91], with permission from Springer Nature.

function is known, the sample work function can be obtained, and SKPM can measure V_{CPD} .

Figure 9 reveals that SKPM operates in the nap mode to measure the sample SP. During the first pass mode, the morphological image is obtained the same as in standard tapping mode. In the second pass mode, the tip is raised on the sample surface by a desired lift height. The mechanical excitation is switched off, and V_{AC} and V_{DC} are applied between the tip-sample [93]. The electrostatic force F_{el} between the tip-sample is given by:

$$F_{el} = \frac{1}{2} \frac{\partial C}{\partial z} \Delta V^2, \quad (20)$$

where $\frac{\partial C}{\partial z}$ and ΔV are the capacitance coupling and voltage difference between the AFM tip and sample, respectively. The total voltage difference between the tip and sample is

$$\Delta V = (V_{DC} - V_{CPD}) + V_{AC} \sin(\omega_e t), \quad (21)$$

where ω_e is the angular frequency of the applied AC voltage. The F_{el} applied to the AFM tip is:

$$F_{el} = \frac{1}{2} \frac{\partial C}{\partial z} \left(\left[(V_{DC} - V_{SP})^2 + \frac{1}{2} V_{AC}^2 \right] + 2[(V_{DC} - V_{CPD}) V_{AC} \sin(\omega_e t)] - \left[\frac{1}{2} V_{AC}^2 \cos(2\omega_e t) \right] \right), \quad (22)$$

where

$$F_{\omega_e} = \frac{\partial C}{\partial z} [V_{DC} - V_{CPD}] V_{AC} \sin(\omega_e t). \quad (23)$$

During SKPM scanning, ω_e is generally set to ω_r (i.e. $F_{\omega_r} = F_{\omega_e}$) to achieve a higher signal-to-noise ratio. The V_{CPD} acquired at minimum F_{ω_r} shows the sample's local [89].

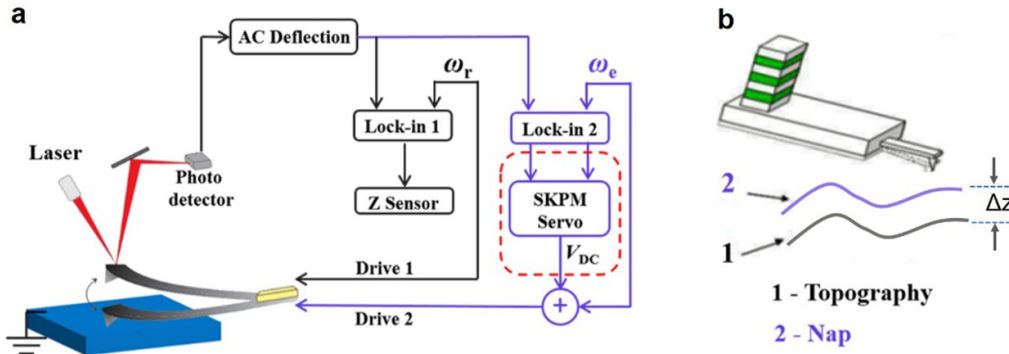


Figure 9. (a) Schematic of the basic setup for scanning Kelvin probe microscopy (SKPM) technique. ω_e is the angular frequency of the applied AC voltage and ω_r is the resonant angular frequency of the cantilever. (b) Drawing map of two scan passes named nap mode. In the first scan, the morphological image is captured using mechanical excitation of the cantilever. The surface potential mapping is acquired in the second scan. The electronic circuit diagram of the first and second scans is given by the black and purple lines. Reproduced from [91], with permission from Springer Nature.

1.4.5. Electrostatic force microscopy (EFM). EFM has multiple branches [94, 95], such as conventional EFM [86, 95], MH-EFM [38, 96–98], dynamic EFM [99], and dynamic contact EFM (DC-EFM). EFM measures the electric field gradient distribution and extracts capacitance changes, electrical potential distribution, and embedded sample conductance by recording long-range electrostatic forces between the tip–sample. In this review, we discuss the principles of conventional EFM and MH-EFM in detail.

1.4.5.1. Conventional EFM. Conventional EFM operates in a two-pass process. During the first scan, the topography image is mapped the same as the standard AC mode. During the second scan, the tip is raised by lift height (usually z is approximately 20–50 nm) to a controllable height z above the sample surface at a specific distance. DC voltage is applied between the tip–sample in lift mode, and the phase shift of the vibrating cantilever is monitored to explore the electrostatic gradient of the sample [91, 95, 100].

1.4.5.2. Multi-harmonic EFM (MH-EFM). In MH-EFM (figure 10), the dual-pass mode detects the topography and electrical properties of the sample. In the first pass, the AFM works similar to the AC mode. In the second pass (lift mode), the short-range repulsive forces and van der Waals forces can be ignored because the tip–sample distance is sufficiently large; meanwhile, an AC voltage of frequency f_ω is applied between the tip and sample, thereby resulting in multi-harmonic electrostatic force F , as follows.

$$F = -\frac{1}{4} \left[\frac{\partial C}{\partial z} V_{ac}^2 + \frac{\partial^2 C}{\partial V \partial z} V_{ac}^3 \cos \omega t + \frac{\partial C}{\partial z} V_{ac}^2 \cos 2\omega t + \frac{1}{2} \frac{\partial^2 C}{\partial V \partial z} V_{ac}^3 (\cos 3\omega t + \cos \omega t) \right]. \quad (24)$$

Accordingly, the second and third harmonic components are given by

$$F_{2\omega} = -\frac{1}{4} \frac{\partial C}{\partial z} V_{ac}^2 \cos 2\omega t, \quad (25)$$

$$F_{3\omega} = -\frac{1}{8} \frac{\partial^2 C}{\partial V \partial z} V_{ac}^3 \cos 3\omega t. \quad (26)$$

Thus, the information corresponding to $\frac{\partial C}{\partial z}$ and $\frac{\partial^2 C}{\partial V \partial z}$ can be obtained by detecting the 2ω and 3ω components, respectively. Further, A_ω is proportional to SP, $A_{2\omega}$ is related to the mobile charge carrier density (MCD), whereas $A_{3\omega}$ reflects the capacitance (or dielectric constant) of the sample [38, 101, 102]. This technology provides an opportunity to explore the electrical response of samples in the kHz range.

1.4.6. Scanning microwave impedance microscopy (sMIM). Scanning microwave impedance microscopy (sMIM) combines microwave technology and AFM. It is a quickly developing technique [103–106] and has demonstrated a broad range of applications, such as detecting electrical properties of various samples (including conductors, semiconductors, insulators, and other functional materials) at the micro/nano scale [107–115]. Presently, this technique has been employed to explore the electrical response of 2D materials, including charge carrier variations, permittivity/conductivity [43, 44], doping density, and dielectric constant [41, 43, 44, 116–118].

During the operation of sMIM, a microwave signal at a high frequency (few GHz) was applied to the tip apex and subsequently transmitted to the sample (figure 10) [115]. Some of the microwave signals pass through, whereas the remaining are reflected off the surface. The reflection coefficient Γ of microwave signals from the contact point measuring the tip–sample impedance mismatch is as follows.

$$\Gamma = \frac{Z_{\text{tip-sample}} - Z_0}{Z_{\text{tip-sample}} + Z_0}, \quad (27)$$

where Z_0 and $Z_{\text{tip-sample}}$ represents the characteristic impedance of the transmission line system and tip–sample, respectively. A cancellation signal suppresses the background to amplify small changes without output saturation. Then, the amplified signal is demodulated by mixer M1. The effective tip–sample impedance can be divided into real and imaginary parts. Standard dielectric sample ($\text{Al}_2\text{O}_3/\text{SiO}_2$) calibrates the

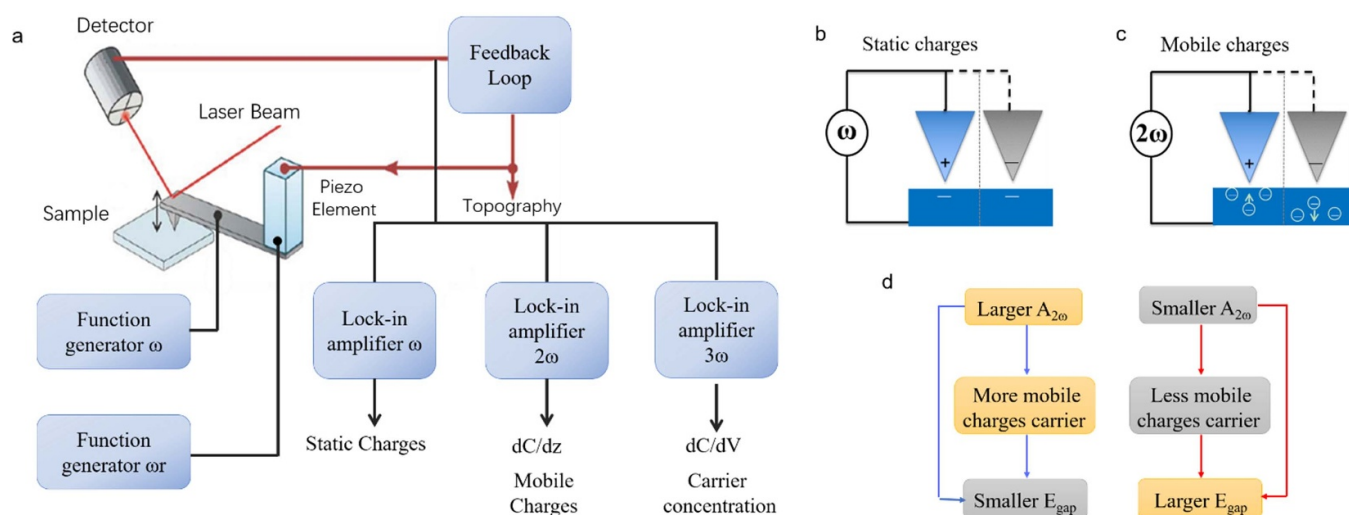


Figure 10. Schematic of multi-harmonic electrostatic force microscopy (MH-EFM). (a) Schematic of MH-EFM experimental setup. A metal-coated tip was used. Two scan passes are needed in this technique. In the first pass, the resonant frequency amplitude of probe f_r is used as feedback to obtain the sample topography. In the second pass (lift mode), an AC bias voltage within the kHz frequency (f_ω) is applied between the tip and sample, and feedback is removed. The amplitude of cantilever vibration at f_ω , $f_{2\omega}$, and $f_{3\omega}$ are obtained by Lock-in amplifiers A_ω , $A_{2\omega}$, and $A_{3\omega}$, respectively. A_ω is proportional to SP, while $A_{2\omega}$ is related to the dielectric constant. The amplitude $A_{3\omega}$ corresponds to the sample carrier concentration. (b) Response of static charges to the charged tip. (c) Response of mobile charges to the charged tip. (d) Relationship between $A_{2\omega}$, mobile charge carriers, and band gap E_{gap} . Reproduced from [91], with permission from Springer Nature.

M1 phase until the output contrast occurs in only one channel (imaginary part of $Z_{tip-sample}$, sMIM-Im). The other channel is the real part of $Z_{tip-sample}$ (sMIM-Re). For semiconductors or insulators, sMIM-Im and sMIM-Re depend on the capacitance (C) and resistance (R) between the tip-sample, respectively, as shown in the inset image lumped element model. Finally, the sMIM-Im and sMIM-Re signal are further modulated by quadrature mixer M2, and dC/dV and dR/dV are obtained.

Figures 10(c) and (d) show the top view and side view of the microwave probe. The main body of the cantilever is made of plasma enhanced chemical vapor deposited (PECVD) Si_3N_4 [105]. The TiW/Au metal tip on the free end of the cantilever is connected to the wire bond pad by a conducting path buried inside two Si_3N_4 layers. Both the front (tip side) and backsides of the cantilever are covered by shield metals, which are electrically grounded in the microwave measurements. The SEM images in figures 10(e) and (f) show the bond pad, the cantilever and the pyramidal metal tip.

We have review the basic principles and instrumentation of sMIM and related scanning microwave microscopy (SMM) in [118], and also discuss its widespread applications in electrical imaging of a number of novel materials and biological systems. Recently, a nice review [119] about sMIM were published, and outlines future opportunities in expanding the capabilities of sMIM. Please check these reviews for further information.

1.4.7. Scanning thermal microscope (SThM). Understanding energy dissipation at the nanoscale level requires probing the temperature fields with micron/nanometer resolution. Scanning thermal microscopy (SThM) [120, 121] can quantitatively map temperature fields or thermal properties

by scanning a sharp SThM probe with a temperature sensor at the tip. This technique has been applied in diverse areas, including microelectronics [122–124], optoelectronics [125, 126], carbon nanotubes [127, 128], and 2D material [53], since the 1990s.

The setup of an AFM-based SThM system is illustrated in figure 11. The combination of the X–Y scan position data along with the force feedback and thermal signals measured by the sensor located either at the tip or on the cantilever provides the raw data of the surface topography and thermal images. The thermal image contrast reflects the change in the amount of heat locally exchanged between the tip and sample. The force feedback control system operates simultaneously but independent of the thermal measurement. The thermal control unit performs real-time thermal signal analysis [129].

Since 1990s, various thermal methods using different thermosensitive sensors or phenomena have been developed. According to the temperature-dependent mechanism, they are classified as thermovoltage [130–132], change in electrical resistance [133–136], fluorescence [137, 138], or thermal expansion [139]. These methods use functional SThM probes, such as metallic or doped silicon. Herein, we introduce two kinds of probes and their corresponding measurement methods.

1.4.7.1. Null-point SThM (NP SThM)—thermocouple type probe. Null-point (NP) SThM [140–142] is based on the thermodynamic principle that the heat flux through the tip-sample thermal contact is zero when the probe tip and sample surface temperatures are identical. Hence, NP SThM measures the unperturbed temperature by the heat flux through the tip-sample thermal contact.

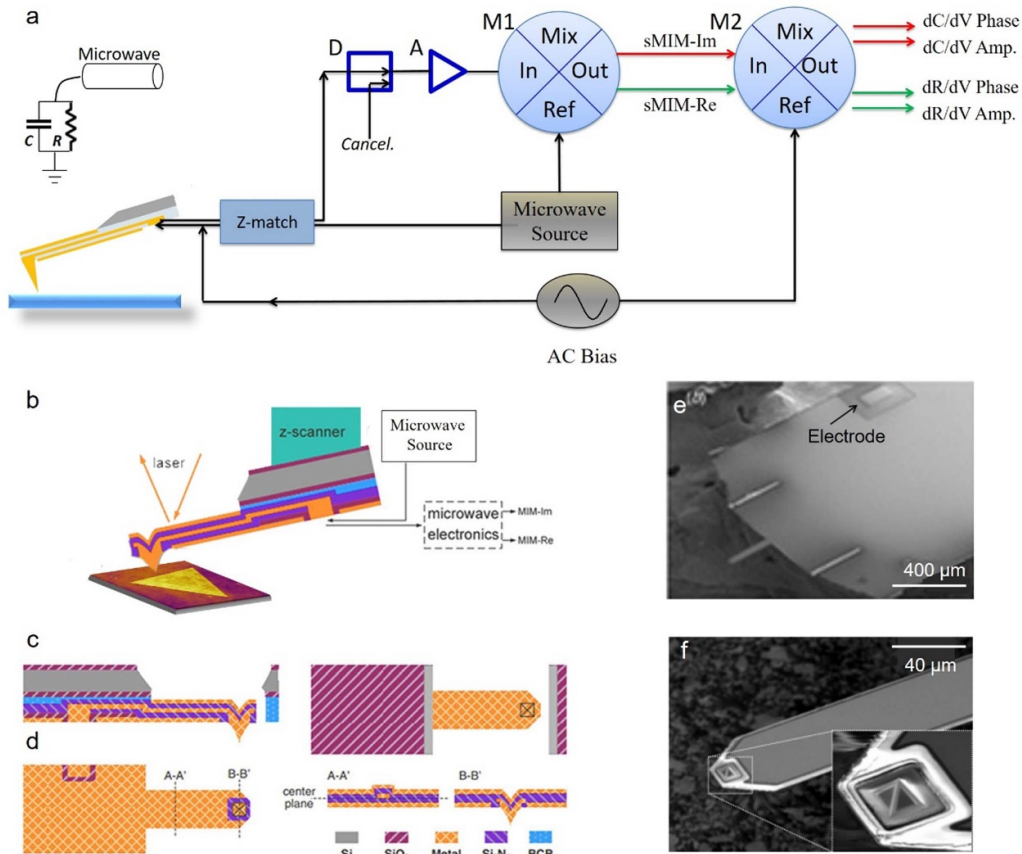


Figure 11. (a) Schematic of sMIM setup. The shielded probe is connected to a microwave source (\sim GHz frequency band). Microwave transmitted into the probe has near-field interactions with the sample, while the reflected microwave is backtracked. The reflected signal is suppressed by the common-mode cancellation through a directional coupler (D), amplified by radio frequency amplifiers (A), and then demodulated by a quadrature mixer (M1). sMIM-Im and sMIM-Re information can be obtained. The signal is further modulated by quadrature mixer M2, and dC/dV and dR/dV are obtained. Inset: schematic of lumped element model. (b) The close-up Schematic of the sMIM probe. (c) The left panels are cross-sectional views and the right panels are top views of the cantilever. (d) Front-view (tip side) of the probe and cross-sectional views of the cantilever (A-A') and tip apex (B-B'). (e), (f) SEM image of sMIM cantilever and tip. The microwave signal was transmitted to the tip through the electrode, marked in (b), to the tip apex. Reproduced from [115]. © IOP Publishing Ltd. CC BY 3.0.

The experimental setup for the NP method is shown in figure 12. The signal-to-noise ratio is maximized by amplifying the thermoelectric voltage extracted from the Wheatstone bridge using a preamplifier and reducing the 60 Hz harmonic noise via a noise filter. The DC thermoelectric voltage is fed into the signal access module and is available with the topographic signal from the atomic force microscope. A DC power supply is used to Joule-heat the sample [141]. The SEM images of the SThM probe used in the experiment are shown in figure 12(b). The cantilever made of silicon oxide, with the lowest thermal conductivity among the materials suitable for nanobatch-fabrication, maximizes the SThM probe sensitivity.

Figure 12(c) shows the principle of quantitative thermal profiling. The SThM probe with a nano-thermocouple junction integrated at the end of the tip, as shown in the inset, is mounted on an atomic force microscope and scans on the same line in the contact and nonthermal contact modes. Thus, the difference between the signals obtained in the two modes is owing to the heat flux through the tip-sample thermal contact. Considering the governing equation for the temperature

distribution and boundary condition [143], the local temperature of the sample T_s is given as

$$T_s(x) = T_c(x) + k_{\text{slope}}(T_c(x) - T_{nc}(x)), \quad (28)$$

where k_{slope} is a dimensionless constant determined through the measurement process in figures 12(d) and (e). Moreover, T_c and T_{nc} are obtained from the temperature sensor integrated at the tip when scanning in the contact and nonthermal contact modes, respectively.

1.4.72. Scanning probe thermometry-doped Si resistor probes. Figure 13(a) shows a typical thermal probe made of a high-doped silicon cantilever with a low-doped silicon heater region. As the heater region is thermosensitive, an electric current to the probe controls and monitors the temperature of the integrated heater region. Changes in the ambient thermal resistance (TR) can change the heater region temperature (ΔT_{probe}) and are monitored through the voltage value of the probe (V_{probe}). In the tip-sample system, the total TR (TR_{total}) measured by SThM between the tip and sample consists of

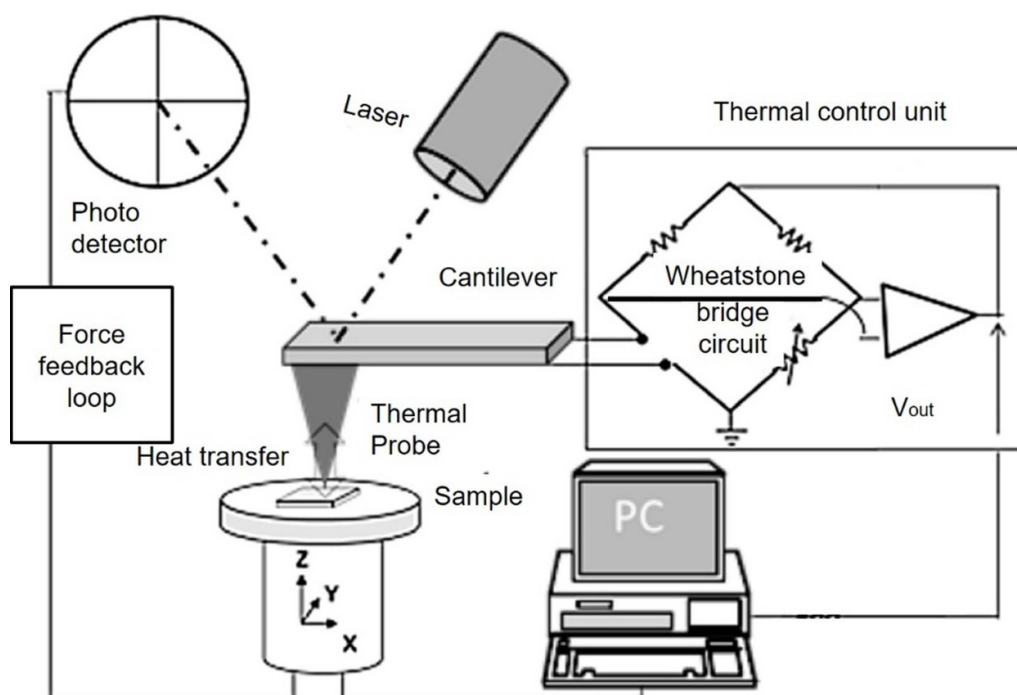


Figure 12. Setup of an AFM-based scanning thermal microscopy (SThM) system. A thermal control unit delivers the output signal V_{out} and a balanced Wheatstone bridge maintains the probe mean temperature at a constant value [129]. John Wiley & Sons. [© 2015 WILEY-VCH Verlag GmbH & Co. KGaA, Weinheim].

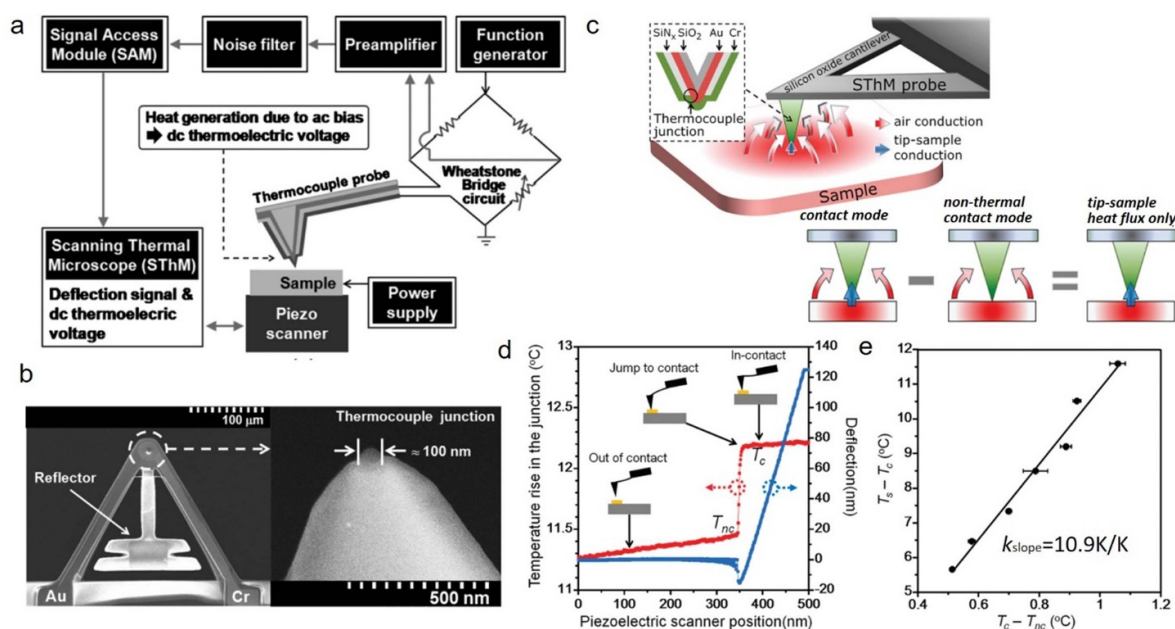


Figure 13. (a) Schematic of the experimental setup for the null-point SThM. (b) SEM images of the SThM probe. Diameter of the thermocouple junction integrated at the apex of the tip is approximately 100 nm, and the tip radius is approximately 50 nm. (c) Principle of quantitative thermal profiling. (d) As the tip approaches the sample, the tip temperature rises gradually due to the heat transfer through the air. When the tip contacts the sample, the tip temperature jumps from T_{nc} to T_c due to the heat flux through the tip-sample contact. (e) Temperature jumps at different sample temperatures. The slope of the graph, k_{slope} , is 10.9 K K^{-1} for this particular probe. Reprinted from [141], with the permission of AIP Publishing. Reprinted with permission from [143]. Copyright (2011) American Chemical Society.

the tip TR (TR_{tip}), contact TR (TR_{contact}), and spreading TR of the sample (TR_{sample}), as shown in figure 13(b).

The circuit diagram of the local thermal analysis (ZThermal) module is shown in figure 13(c). The electric resistance of the reference electrical resistor is known ($R_{\text{ref}} = 4000 \Omega$), and the total voltage (V_{total}) and probe voltage (V_{probe}) can be exerted or detected. The electric resistance of the probe is thermosensitive, and the relationship of the electric resistance (R_{probe}) versus temperature ($\Delta T_{\text{probe}} = T_{\text{probe}} - T_{\text{air}}$) is shown in figure 13(d). The maximum electric resistance is observed at 550 °C. Below 550 °C, the electric resistance of the probe corresponds to a specific temperature, as follows [53]:

$$R_{\text{probe}} = \frac{V_{\text{probe}}}{V_{\text{total}} - V_{\text{probe}}} R_{\text{ref}} \sim \Delta T_{\text{probe}} \quad (29)$$

The thermal power generated by the thermal probe can be calculated as follows:

$$P_{\text{probe}} = \frac{V_{\text{probe}}^2}{R_{\text{probe}}}. \quad (30)$$

We introduce the design idea of NP SThM [144] and the quantized thermal transport characterization [145] and use the thermal tip-sample approach curve to calculate TR. The model assumes that when the tip abruptly contacts the sample, the thermal circumstance and heat transfer coefficient (h) of the thermal tip in the air do not change. However, before contact, the heat ($Q_{\text{air,off}}$) generated by the thermal tip dissipates into the air, whereas after contact, a new thermal flow channel is opened and a part of the heat (Q_{sample}) diffuses into the sample. Thus, the heat transfer equation can be given as

$$\text{Off contact: } P_{\text{off}} = Q_{\text{air,off}} = A \cdot h \cdot \Delta T_{\text{off}}, \quad (31)$$

$$\begin{aligned} \text{On contact: } P_{\text{on}} = Q_{\text{air,on}} + Q_{\text{sample}} = A \cdot h \cdot \Delta T_{\text{on}} \\ + \frac{1}{TR_{\text{total}}} \cdot \Delta T_{\text{on}}, \end{aligned} \quad (32)$$

where A is the superficial area of the tip; and P_{off} and P_{on} are the heat power generated by the thermal probe before and after contact, respectively. Thus, the total TR can be deduced as:

$$\frac{1}{TR_{\text{total}}} = \frac{P_{\text{on}}}{\Delta T_{\text{on}}} - \frac{P_{\text{off}}}{\Delta T_{\text{off}}}. \quad (33)$$

Based on the thermal tip-sample approach curve (figure 13(e)), the total thermal resistance can be solved using the tip voltages of points A and B, combined with equations (29)–(33).

Although the SThM method has been calibrated and quantified in air conditions, two main limitations exist. One is the spatial resolution due to the liquid film existing at the tip-sample interface, and the other is the difficulty in quantitative measurements due to the parasitic air conduction between the sample and SThM probe. However, the ultra-high vacuum (UHV)-based SThM technique enables the

quantitative measurement of thermal maps with ~ 15 mK temperature resolution and ~ 10 nm spatial resolution [146].

SThM opens new avenues for investigating physical phenomena in the quantum regime. In this review, we will mainly focus on the applications of SThM at the interface and surface of 2D materials.

2. Applications of AFM in surface/interface of 2D materials

Following the discovery of graphene [147], considerable research has been focused on 2D materials [148, 149]. Transition metal dichalcogenides (TMDCs) have emerged as an important 2D-layered material owing to their superior characteristics [149]. Several desirable properties emerge at monolayer limits, the most notable of which is the presence of a direct bandgap [149, 150]. From the perspective of spatial resolution, AFM has obvious advantages in studying the ultrafine structure of 2D materials. Moreover, the multi-functional AFM technology, which was extended from AFM, can realize high-resolution and physical and chemical properties quantitative characterization of materials. It is playing an increasingly important role in characterizing the local electrical, mechanical and thermal properties of 2D materials at the nanoscale level [17–19, 53, 151–153]. This section discusses recent studies on surface/interface of 2D materials using AFM.

2.1. Mechanical engineering of surface/interface

Tuning the material band structure by subjecting it to strain is an important strategy to enhance the electronic device performance. Diverse methods have been proposed for introducing strain in 2D materials, including the bending of films on elastic substrates [10, 11, 16], stretching of films using atomic force microscope probes [17–19], and thermal expansion mismatch [20–23]. Our review mainly focuses on the stress application methods discussed in sections 2.1.1 and 2.1.2.

2.1.1. Thermal strain. The thermal expansion coefficient (TEC) mismatch is a convenient method to produce controllable strain in TMDCs [155, 156]. Owing to the high temperatures when synthesizing TMDCs, the TEC-mismatch between the substrate and 2D semiconductor can control the strain in the synthesized 2D materials, as shown in figure 14. The tensile (compressive) strains accumulate on the TMDCs when the substrate TEC is less (greater) than that of the 2D material. Moreover, relaxed samples are obtained if the TEC of the substrate and 2D material match. The thermal strain-engineered behaviors of chemical vapor deposition (CVD)-grown triangular MoS₂ and WS₂ flakes were reported by our group and will be summarized in this section.

2.1.1.1. Edge dependent strain behaviors. We consider a micrometer or larger-sized 2D layer as a continuum where the atomic details are averaged, and the classical elasticity theory governs, as illustrated using the six-fold hexagonal 2D material in figure 15(a). However, a close examination

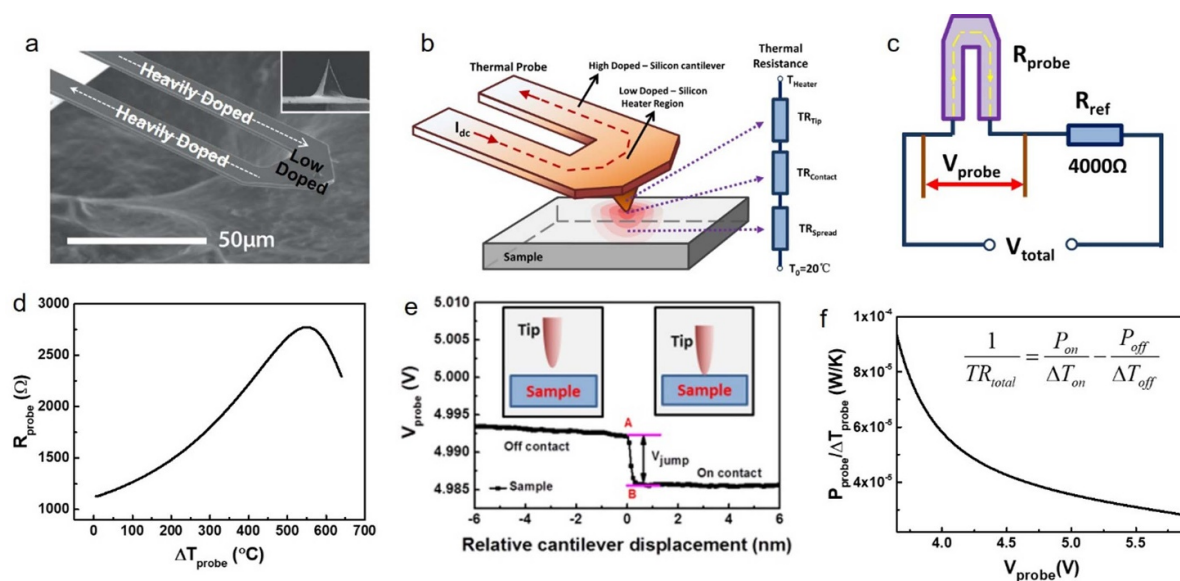


Figure 14. (a) SEM image of a doped silicon probe. (b) Schematic of the principle of thermal probe. (c) Circuit diagram of the local thermal analysis module. (d) Probe electric resistance (R_{probe}) vs. temperature ($\Delta T_{\text{probe}} = T_{\text{probe}} - T_{\text{air}}$) curve. (e) Demonstration of the thermal tip-sample approach curve. (f) Thermal conductivity (the reciprocal of thermal resistance) vs. tip voltage curve. Thermal conductivity (resistance) is negatively (positively) correlated with the probe voltage. Reproduced from [53] with permission from the Royal Society of Chemistry.

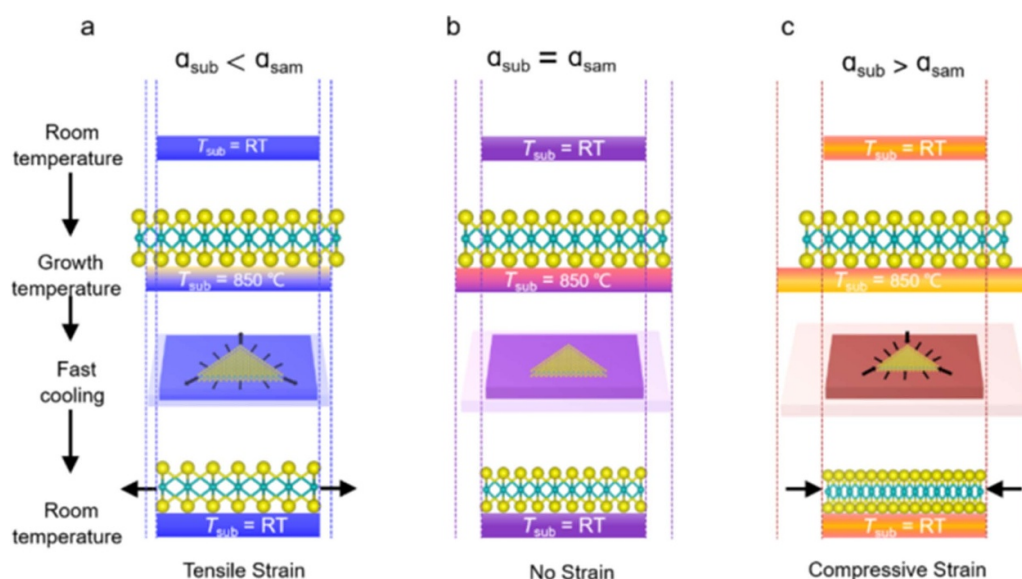


Figure 15. Strain-engineered transition metal dichalcogenides (TMDCs) using the thermal expansion coefficient (TEC)-mismatch. (a)–(c) Process schematic through which 2D materials realize strain via the TEC-mismatch between the substrate and TMDC. (a) Tensile strain is achieved when the substrate TEC is less than that of the 2D material, (b) relaxed samples are achieved when the TEC of the substrate and 2D material match, and (c) compressive strain is achieved when the substrate TEC is greater than that of the 2D material. Reprinted with permission from [154]. Copyright (2022) American Chemical Society.

of the hexagonal flake at the nanoscale level, e.g. monolayer WS_2 , under strain (figure 15(b)), shows that the two inequivalent edges can make the local elastic modulus non-uniform. The hexagonal flake is divided into six regions because of its C_3 symmetry and the two different edges. We denote these regions using the edge type as Zigzag (ZR) and Klein regions (KR).

Figures 15(c) and (d) depict typical topographies of the WS_2 monolayer showing a uniform hexagonal shape. Local SP

and surface MCD were measured using SKPM and DH-EFM, as presented in figures 15(e) and (f), respectively. The local SP of the WS_2 flake shows six domains, categorized into two SP levels with 8 meV difference. Given the relation between the MCD and bandgap (E_{gap}), we deduce that the local bandgap is larger in ZR than in KR, i.e. $E_{\text{gap}}(\text{Z}) > E_{\text{gap}}(\text{K})$ (figure 16).

The CR mode characterizes the out-of-plane modulus by recording the resonance frequency shift of the probe-sample system (figure 17). Based on the model explained in

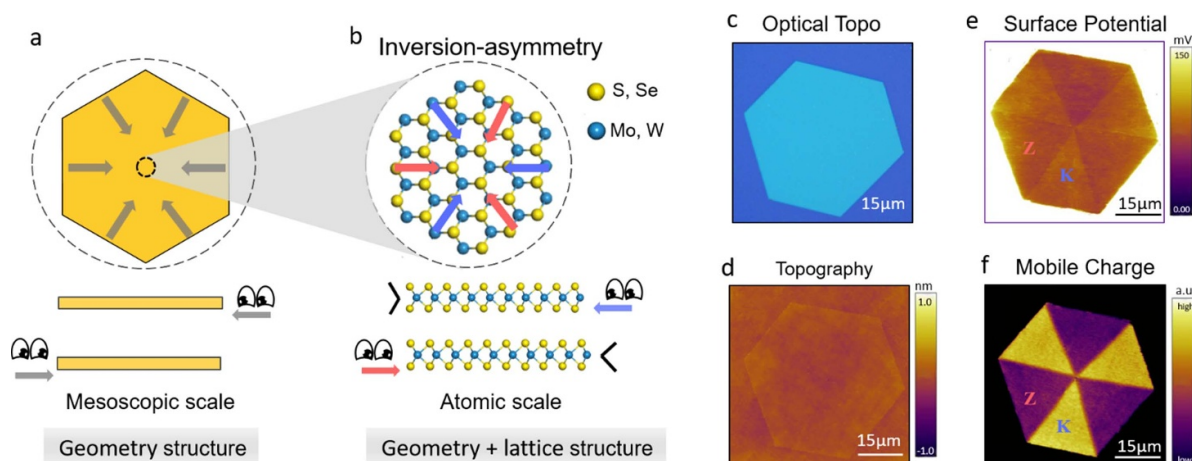


Figure 16. (a) Top (upper panel) and side (lower panel) views of a 2D film at a mesoscopic scale where the edges are identically treated, showing a six-fold symmetry (see cartoon eyes and arrows). (b) Corresponding top and side views at the atomic scale show two completely distinctive edges and a three-fold symmetry. (c). (d) Typical optical and AFM topography of WS₂ layer on SiO₂/Si substrate. (e) Corresponding local SP images using SKPM. (f) Mobile charge carrier density (MCD) image of WS₂ taken in dual harmonic-EFM (DH-EFM). (f) Friction force image of WS₂ flakes. Reprinted with permission from [151]. Copyright (2020) American Chemical Society.

section 1.4.3, we estimate the elastic modulus ratio in KR and ZR as ~ 1.002 . The topographies of WS₂ (figures 17(b) and (c)) show uniform contrast but different elastic modulus (figure 17(e)). The out-of-plane elastic modulus of ZR was significantly smaller than that of KR, which is consistent with the Density Function Theory (DFT) results (figure 17(a)). Furthermore, the ZR and KR energy dissipation differences are resolvable through CR (figure 17(f)).

The friction force between the tip and sample is often affected by the out-of-plane, in-plane, and buckling modulus of a sample (figure 17(g)), which are difficult to measure. Therefore, FFM was employed here to measure the friction force by imaging the lateral torsion of the cantilever through contact scanning along the perpendicular direction. Figures 17(h) and (i) show the friction force images of the WS₂ flake. The friction force of KR is larger than that of ZR, probably because of the smaller in-plane and larger out-of-plane moduli of KR. Thus, the micron-sized triangular KR and ZR explicitly show different measured mechanical properties in terms of elastic modulus, energy dissipation, and friction force.

2.1.1.2. Size dependent strain behaviors. The strain behaviors of TMDCs with different sizes have been studied by several groups [157–160]. Strain domains with triple symmetry have been observed in samples having a relatively small size ($< 50 \mu\text{m}$) and less strain. In contrast, the mechanical behavior of WS₂ monolayers at $\sim 100 \mu\text{m}$ scale is more complex. Triangular TMDC flakes of size $5\text{--}45 \mu\text{m}$ (figures 18–20) and WS₂ flakes larger than $90 \mu\text{m}$ (figure 21) are summarized here.

After the CVD growth, the fast-cooling process introduces tensile strain into the synthesized MoS₂ flakes (figures 18(a) and (b)). Figures 18(c) and (e) show the large-scale optical images of the as-grown triangular MoS₂ flakes at different SiO₂/Si substrate regions. Two kinds of flakes are displayed in

the close-up optical image (figures 18(f)–(i)). In figures 18(f) and (g), the specific geometrical shape has complete curved edges and sharp corners (less than the traditional 60° ; therefore named as sharp-corner flake). In figures 18(h) and (i), the specific geometrical shape has partially curved edges at the middle regions (named as vein-like flake) and corner angles of $\sim 60^\circ$. The statistical results of the measured sharp-corner and vein-like MoS₂ flakes are shown in figure 18(d). In general, the vein-like flakes are relatively larger than that of sharp-corner flakes. The critical size is estimated at $\sim 17 \mu\text{m}$.

Advanced AFM techniques further investigate the strain-engineered structure and property of MoS₂ flakes. The AFM topography image of the triangular sharp-corner MoS₂ monolayer shows no specific features within the flake, as shown in figure 19(a). In contrast, FFM (figure 19(b)) reveals three sharp corners (marked II) with distinctive strain-induced features from the central region (marked I). Moreover, the strain at the corners (II) is different from that at the central region (I).

According to the previous theoretical works, the tensile (compressive) strain can decrease (increase) the band gaps of the MoS₂ monolayer [161]. The DH-EFM qualitatively evaluates the strain-induced local MCD, which depends on the band gaps of MoS₂ flakes. A higher MCD is observed at the sharp corners than in central regions within the triangular flakes (figure 19(c)), indicating a smaller bandgap at the corners under a larger tensile strain. The sMIM mode measures the electronic properties of the sharp-corner MoS₂ flakes (figure 19(d)) and confirms a higher electronic conductivity at the sharp corners. The results indicate that the sharp corners suffer larger tensile strain than the central regions.

The strain-engineered structure and properties of the vein-like MoS₂ flakes were further investigated in comparison with the sharp-corner flakes (figures 19(e)–(h)). The distinctive strain-induced features were observed using FFM (figures 19(f) and (g)), with three straight lines originating

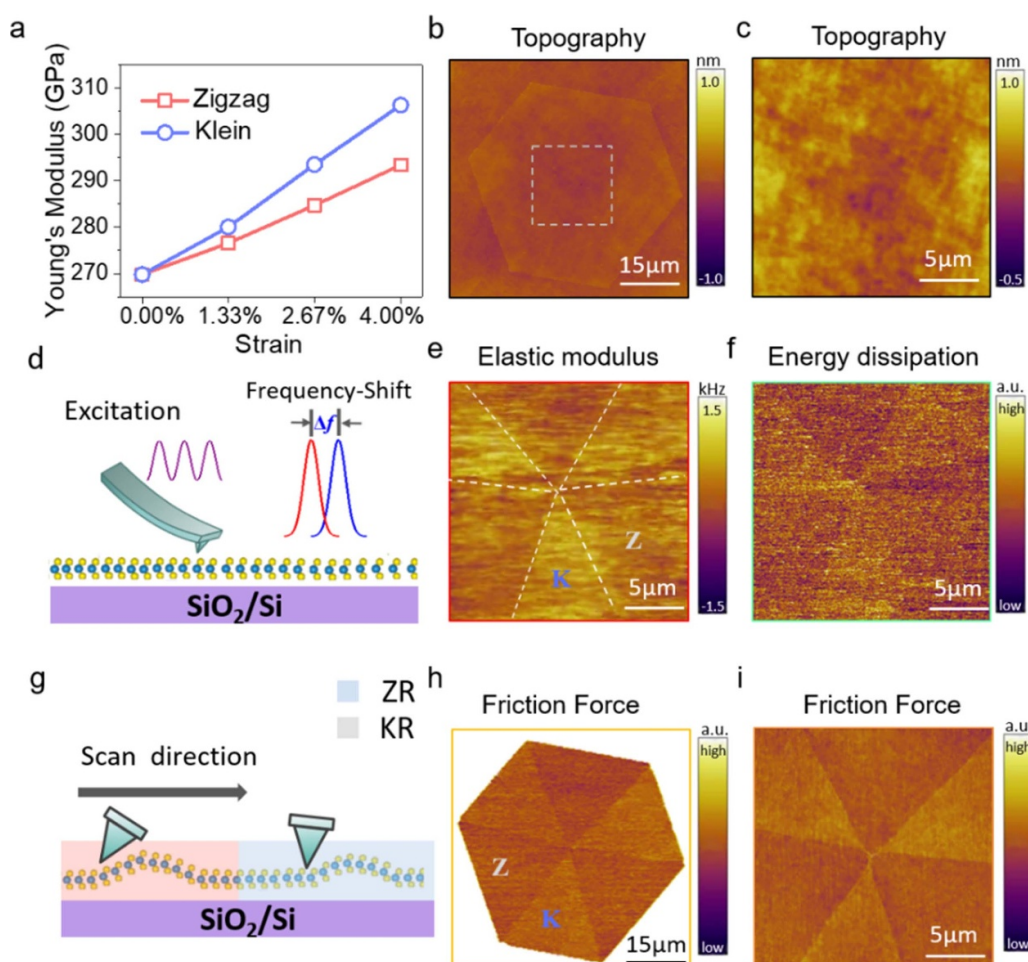


Figure 17. Mechanical properties of hexagonal WS₂ flakes. (a) Young's modulus calculated by Density Function Theory (DFT). (b) AFM topography of the WS₂ layer on the SiO₂/Si substrate. (c) Close-up AFM topography of the central area of the WS₂ layer. (d) Sketch map of contact resonance mode. (e), (f) Elastic modulus and (e) energy dissipation (f) in CR mode. The corresponding topography is shown in (c). (g) Sketch map of FFM. (h), (i) Friction force image of WS₂ flakes. The corresponding topography is shown in (b) and (c). Differences in the mechanical property of ZR and KR stem from the C₃ atomic arrangement and inherent non-equivalence at the KR and ZR triangle vertexes. Reprinted with permission from [151]. Copyright (2020) American Chemical Society.

from the center to the corner apex. Figure 19(g) shows the enlarged central region, with a hierarchical hexagonal ripple pattern around the central triangle. In DH-EFM (figure 19(h)), the highest mobile charge densities were observed at the three straight lines starting from the flake center, in contrast to the medium and lowest charge density at the ripple areas and corners, respectively. Thus, the three straight lines suffer larger tensile strain than the ripple areas.

Kim *et al* [158] presented nanoscale photoluminescence (PL) spectroscopy images of triangular CVD-grown WS₂ monolayers of different sizes under different temperatures and excitation power (figure 20(a)). Intense PL emissions were observed around the edges of individual WS₂ grains. Meng *et al* [162] reported the SPs and work functions of strained WS₂ flakes of 20 μm size. In the interior regions, work functions are much larger than those of the unstrained regions (figures 20(b) and (c)). The strain domain distribution displays a three-fold symmetry in figures 18–20. However, the strain domains were more complex when the TMDC flakes increased to ~90 μm.

The monolayer WS₂ flakes were also prepared via CVD and underwent fast-cooling to introduce thermal strain (figure 21(a)). The magnitude of the tensile thermal strain within the WS₂/SiO₂ flakes depends on the TEC-mismatch and flake size. Here, the WS₂ monolayer (size ~100 μm) was split into different forms by several cracks, and the cause of the crack formation was studied using finite element analysis (FEA). The von Mises stress is a critical principle to characterize the yielding and fracture of materials; a point subject to a higher von Mises stress is the starting point of failure. The von Mises stress distribution of a triangular WS₂ flake with a hexagon nucleation center is shown in figure 21(b). Strong stress concentrations are generated at the vertices of the hexagon nucleation center (marked by arrows), which initiate cracks that extend outward to release the stress. Because the stress in the corner regions of the WS₂ layers is much larger than that in the edge centers, the cracks tend to extend toward the corner regions. Several cracks (broken lines) were found in the strained WS₂ flakes, and these cracks split the WS₂ flakes into six-splitting forms (figure 21(c)).

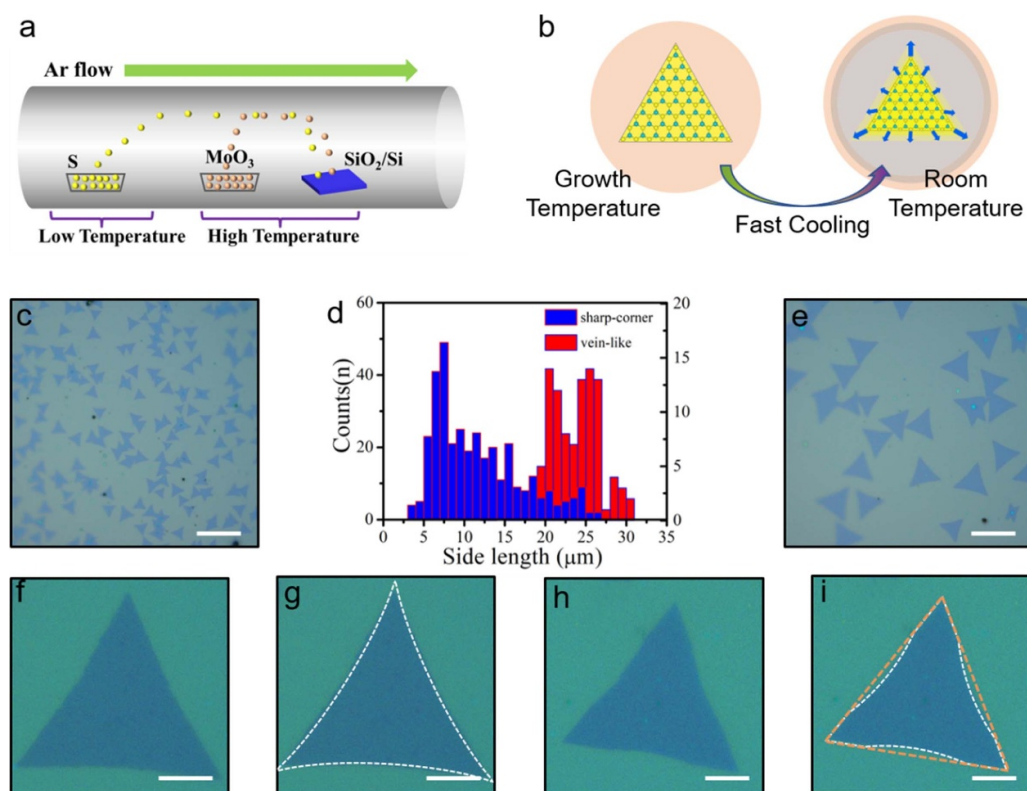


Figure 18. Sample preparation of triangular MoS₂ flakes and the introduction of tensile strain. (a) Schematic of traditional low-pressure chemical vapor deposition (CVD) growth process. (b) Introduction of tensile strain applied by the underlying substrate during the fast-cooling process. (c), (e) Size-dependent large-scale optical images of (c) sharp-corner and (e) vein-like MoS₂ flakes. (d) Statistical results of the measured sharp-corner and vein-like MoS₂ flake size. Optical images of (f) and (g) sharp-corner MoS₂ flake and (h) and (i) vein-like MoS₂ flake. Scale bars: (c) and (e) 30 μm; (f)–(i) 5 μm. Reproduced from [153]. © IOP Publishing Ltd. All rights reserved.

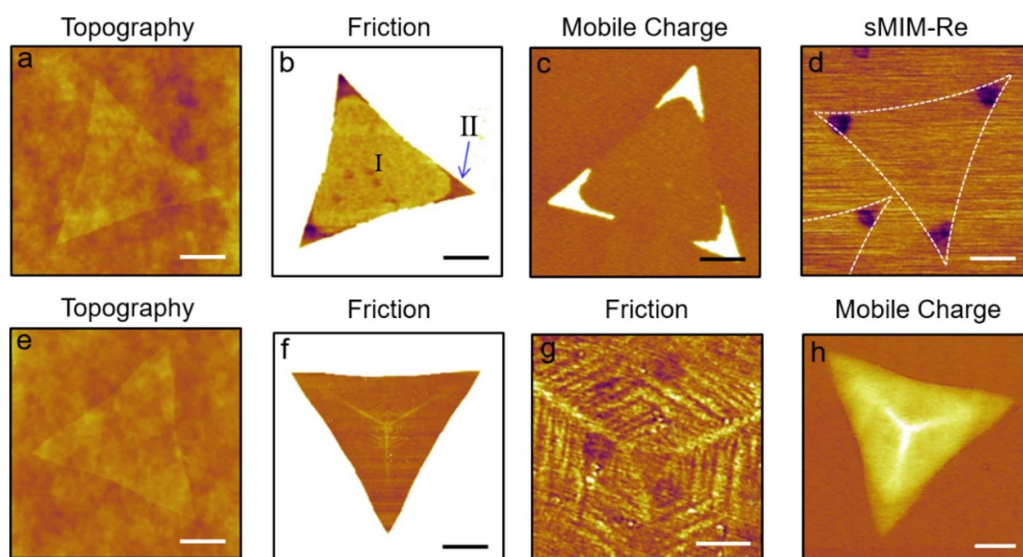


Figure 19. (a)–(d) Strain-engineered structures and properties. (a) AFM topography, (b) FFM friction, (c) mobile charge density and (d) sMIM images of sharp-corner MoS₂ flake on the SiO₂/Si substrate. (e) AFM topography, (f), (g) FFM friction, (h) mobile charge density image of vein-like MoS₂ flake on the SiO₂/Si substrate. Scale bars: (a)–(c) 6 μm; (d) 2 μm; (e) 5 μm; (f) 8 μm; (g) 3 μm; (h) 5 μm. Reproduced from [153]. © IOP Publishing Ltd. All rights reserved.

The electrical properties of the triangular-shaped six-splitting WS₂ monolayers were examined. Figure 21(d) depicts AFM topographies of the WS₂ monolayer with

no visible height difference within the flakes. The surface MCD measured using DH-EFM shows several nanopatterns, such as the unclosed and closed rings, within

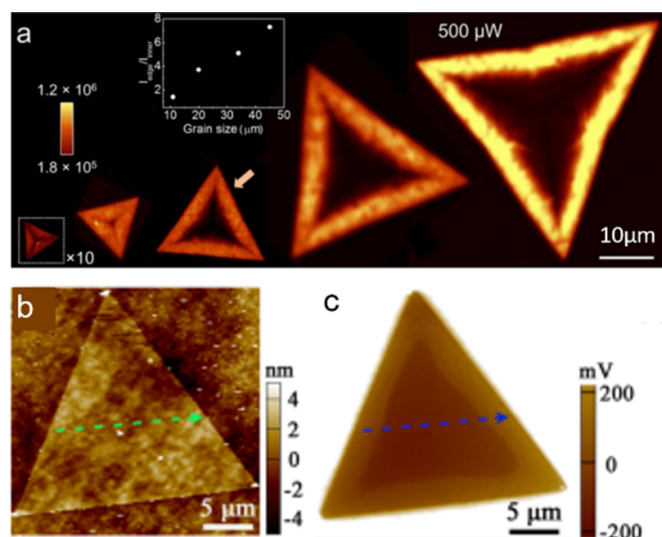


Figure 20. (a) Photoluminescence (PL) intensity maps of triangular WS_2 monolayers of lateral sizes from ~ 6 to $45 \mu\text{m}$. Reprinted with permission from [158]. Copyright (2016) American Chemical Society. (b) AFM image of a typical triangular WS_2 flake on SiO_2/Si substrate. The sample was prepared by CVD and underwent a fast = cooling process. (c) KPFM SP map of the triangular WS_2 flake in panel (b). Reprinted from [162], with the permission of AIP Publishing.

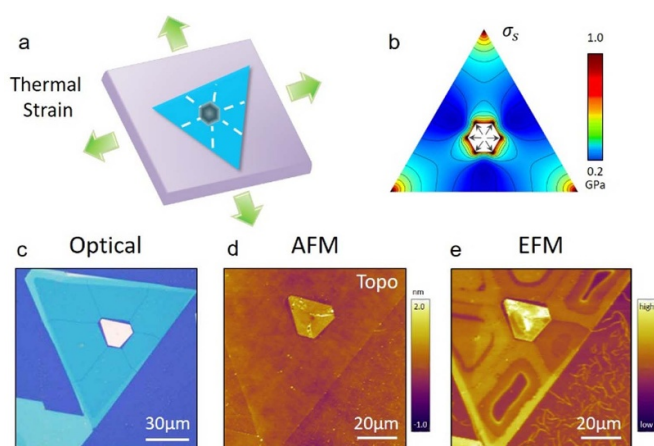


Figure 21. (a) As-grown sample rapidly cooled to room temperature (25°C) from the growth temperature to introduce uniform strain into the sample. (b) von Mises stress of the WS_2 flake with the hexagon nucleation center simulated using finite element analysis (FEA). The black lines in (b) are stress isolines, almost perpendicular to the boundary edge. (c), (d) Optical and AFM topography of the six-splitting WS_2 layer on the SiO_2/Si substrate. (e) MCD image of the WS_2 using DH-EFM. Reprinted with permission from [154]. Copyright (2022) American Chemical Society.

each part of the six-splitting WS_2 monolayer (figure 21(e)), thus suggesting nonuniform local electrical properties. Additionally, the band gap, frictional, viscosity, and elasticity characteristics of the different strain regions were investigated. The nanopattern should enable the flexible designing of more sophisticated devices based on 2D materials.

2.1.1.3. Geometry dependent strain behaviors. The strain-induced hierarchical ripple nanostructures, modified by the MoS_2 shapes, were also observed in MoS_2 flakes. Therefore, the structural evolution of these hierarchical nanoripples is further discussed based on the geometry and thickness of MoS_2 flakes.

The shape of the MoS_2 flakes can be modified by controlling the S/Mo ratio and growth temperature, as shown in figure 22(a). The most common triangular flakes are obtained at a high S/Mo ratio and low growth temperature. When the S/Mo ratio is reduced, and growth temperature is increased and triangular flakes with multi-apex corners are obtained, as shown in figures 22(b)–(g). The optical image of each flake shows a uniform contrast. Furthermore, a second layer can grow at the center of these triangular flakes and exhibit a perfect triangular shape. Herein, both 2H- and 3R- MoS_2 bilayer polytypes were obtained, as shown in figures 22(h) and (i). After CVD at high temperature, the isotropic tensile strain was applied on the triangular MoS_2 flakes through the substrate during fast-cooling. The tensile strain is due to the TEC mismatch between the MoS_2 flakes (10^{-5}K^{-1}) and SiO_2/Si substrate (10^{-7}K^{-1}) and may induce the out-of-plane ripples due to the Poisson instability of MoS_2 layers. Considering the geometry of MoS_2 flakes, the strain at the three corners is larger than in other regions.

Figures 22(j)–(o) show two typical triangular MoS_2 monolayer flakes with one small (figures 22(j)–(l)) and three large (figures 22(m)–(o)) dual-apex corners. Here, triangular flakes with multi-apex corners have been determined as single crystalline using TSM. The distinctive strain-induced features observed using the FFM mode, as shown in figures 22(j) and (m), exhibit a three-fold radial pattern from the center of triangular MoS_2 monolayer flakes. The symmetry of the features is affected by the strain distribution within the flakes and the geometry of MoS_2 layers. In the close-up FFM images (figures 22(k) and (n)), the hierarchical ripple nanostructures (marked II in figure 22(n), named ripple regions) distinctively differ from the flat regions (marked I), as observed in these strain-induced features. The indiscernible nanoripples in AFM topographies exhibit ripple heights of less than 1 nm. Additionally, the nanoripple areas exhibit lower friction signals owing to the strain-modified mechanical properties of MoS_2 films.

Moreover, the in-plane strain within these MoS_2 films can modify the local electronic properties. The tensile (compressive) strain can decrease (increase) the bandgap of MoS_2 films [163]. Therefore, DH-EFM was further employed to evaluate the local MCD and bandgaps of MoS_2 films qualitatively. As shown in figures 22(l) and (o), a higher MCD is observed in the hierarchical ripple areas than in the flat regions within the triangular flakes, thus indicating a reduced bandgap in these ripple structures under a tensile strain.

Figures 23(a)–(d) show a small part of the FFM images for the hierarchical ripple structures with varied multi-apex corners. The hierarchical ripple structure size is determined by the size of triangular flakes, whereas their strain-induced properties are controlled by the opening angle α or width d of the multi-apex corners [17].

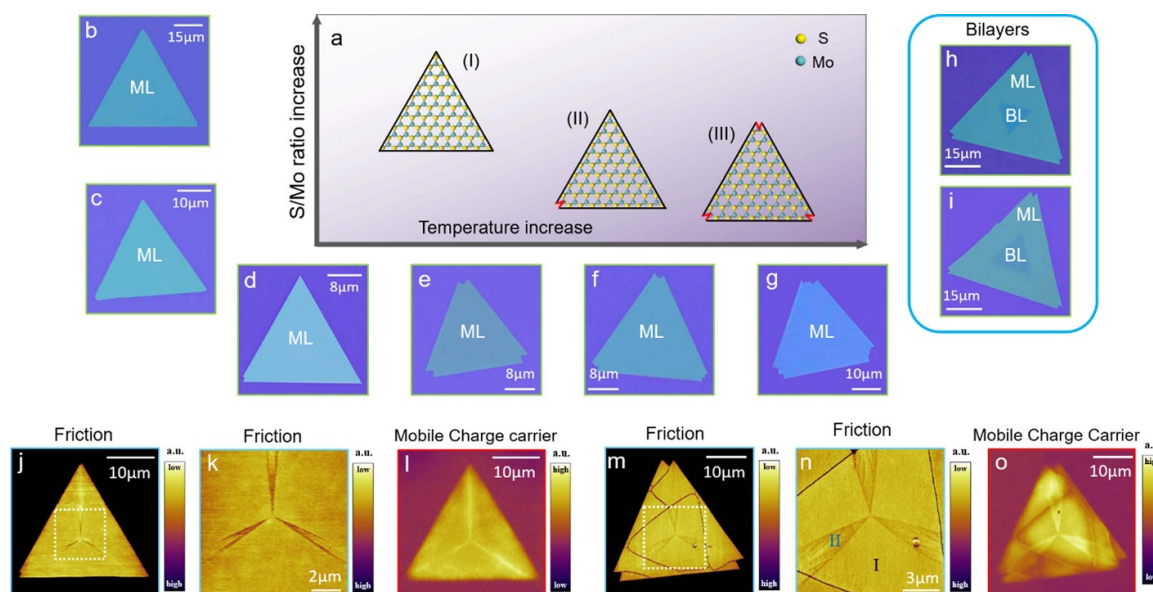


Figure 22. (a) Schematic shape evolution of MoS₂ flakes with various S/Mo ratios and growth temperatures. (b)–(h) Optical topographic images of a series of triangular flakes with multi-apex corners. (j), (k) Friction and (l) MCC images of the MoS₂ flake with small dual-apex corners. The corresponding optical image is in (d). (m), (n) Frictional and (o) MCC images of the MoS₂ flake with larger dual-apex corners. The corresponding optical image is in (e). Reprinted from [17], with the permission of AIP Publishing.

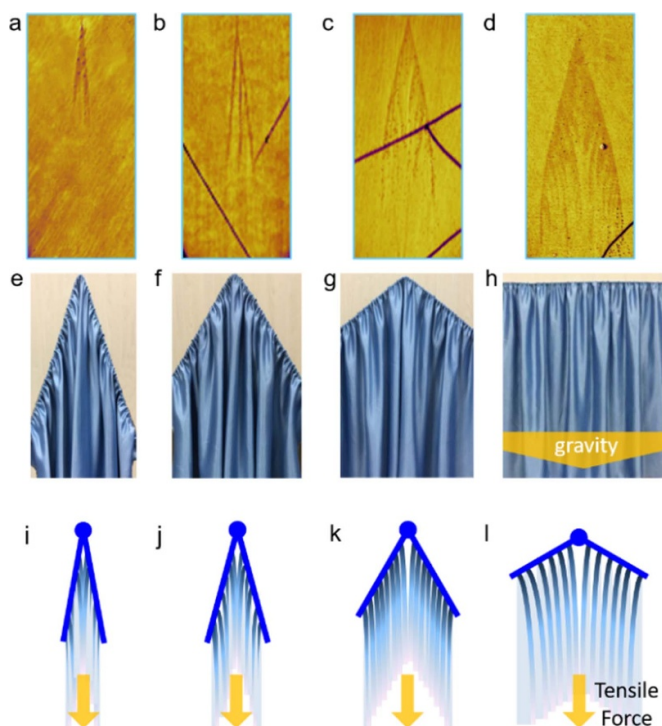


Figure 23. Formation mechanism of hierarchal ripple structures. (a)–(d) FFM images of the hierarchal ripple structures in MoS₂ with different opening angles. (e)–(h) Evolution of hierarchal ripples in a silk curtain when the confined edges are gradually bent. These ripples are generated through the longitudinal tensile strains applied by the gravity of itself. (i)–(l) Schematic for elucidating the formation and evolution of hierarchal ripples. Reprinted from [17], with the permission of AIP Publishing.

The universal self-similar hierarchy of ripples can be observed within the thin sheets or films when under tensile strain and boundary edge confinement [164–167]. This

curtain effect is demonstrated in our experiment, shown in figure 23(h). These ripples are primarily along the longitudinal direction (same as the direction of gravity) and perpendicular to the boundary edges. Wrinklon is the localized transition zone where two ripples merge, which is a building block for these hierarchical ripple patterns. To further understand their structural evolution, we gradually bent the boundary edge, as shown in figures 23(e)–(g). When bent to a ‘^’ shape, the ripples fail to orient along the longitudinal direction but are affected by the bent edges. The ripples near the edges orient perpendicular to the bent edges. In contrast, the ripples farther from the edges gradually bend along the longitudinal tensile direction of gravity while retaining hierarchy. The hierarchical ripples in the bent curtains are relatively similar to those in the triangular MoS₂ flakes. Based on their inherent similarities, a simple diagram is proposed to elucidate their formation mechanism (figures 23(i)–(l)).

2.1.2. Strain applied through the AFM probe in contact mode

2.1.2.1. Strain-induced in-plane anisotropic shear behaviors (crystallographic orientation imaging). Xu *et al* [18] reported in-plane shear stiffness anisotropy under uniaxial normal tension strain in monolayer MoS₂ and experimentally verified the shear characteristic based on friction-driven stretch deformation during the TSM contact scan.

For TSM, the scan direction of the AFM tip is parallel to the cantilever axis, and the lateral torsion of the cantilever is recorded. For a flexible film weakly bound onto a rigid substrate, the film puckers locally during contact scan by the AFM tip. When the tip moves the puckered region forward, the puckered geometry causes the film to relax at the front edge and stretch at the rear area of the tip simultaneously

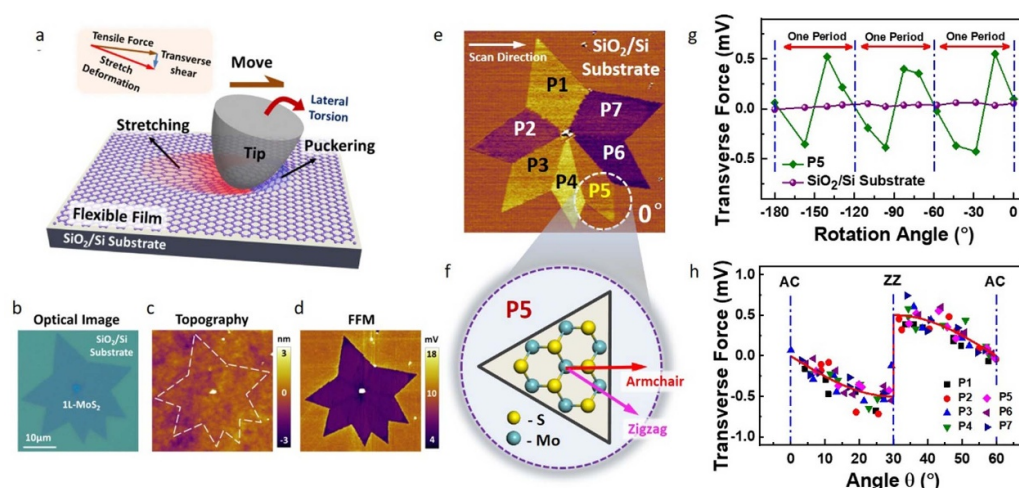


Figure 24. (a) Schematic for TSM and stress distribution originating from stretch deformation. Friction can drive the stretch deformation of a film, and the TSM signals originate from the noncollinearity between the stretch force and deformation direction. If there is strain-induced anisotropic shear deformation, TSM signals will not be zero. (b) Optical image, (c) AFM topography, (d) FFM image, and (e) TSM image of a star-shaped monolayer MoS₂ flake sample. In (e), (f), crystallographic labels for AC and ZZ orientations. Every domain of star-shaped monolayer MoS₂ is given an identifier from P1 to P7. (g) Shear signal vs. rotation angle curves obtained by randomly selecting P5 domains with the SiO₂/Si substrate. (h) Scatterplot diagram of shear signal vs. crystallographic orientation using the AC orientation as the reference direction of 0°. All the data points are translated into one period of 60°. Reprinted from [18], with the permission of AIP Publishing.

(figure 24(a)), which breaks the original in-plane mechanical isotropy of the hexagonal 2D atomic crystal. FFM can characterize anisotropic stretch deformation and friction energy dissipation for an elastically anisotropic film. Such friction-driven stretch deformation will cause the stretch force direction to deviate from the deformation direction. The intersection angle creates an additional transverse shear component that generates lateral torsion of the cantilever and is the source of TSM signals. On an isotropic surface, the transverse shear signal is zero.

The star-shaped monolayer MoS₂ flake was characterized using AFM (figures 24(c)–(e)). We can observe remarkable contrasts of the star-shaped domains in the TSM image (figure 24(e)) but not in the corresponding FFM (figure 24(d)) and topography (figures 24(b) and (c)) images. FFM fails to distinguish the frictional and elastic anisotropies of the domains probably because of its low sensitivity.

For TSM characterization with a series of clockwise rotations, the periods of 60° of the shear signals are presented (figure 24(g)), thereby implying consistency with the hexagonal symmetry of MoS₂. More precisely, the scatterplot diagrams of shear signal vs. crystallographic orientation for the seven domains (figure 24(h)) exhibit the same distribution regularity, which confirms that the anisotropic shear deformations accurately correspond to crystallographic orientation.

TSM characterization is useful for crystallographic orientation imaging of monolayer samples and characterization of bilayer samples, such as bilayer MoS₂ and graphene [19]. Due to the van der Waals (vdW) interactions between the top and bottom layer, the adhesion and puckering effect occur primarily between the AFM tip and top layer as the AFM tip

approach, contact, and move on the top layer (figures 25(a) and (b)). Figures 25(c) and (d) show the optical and AFM topography images of the bilayer MoS₂ flakes. The bilayer areas are marked by white dashed lines.

Figure 25(e) shows the FFM images of the bilayer MoS₂ flake. No crystalline differentiated contrast is observed on top and bottom layer grains. The friction signal on the bilayer area is slightly lower than that on the monolayer area. Figure 25(f) shows the TSM images of this bilayer MoS₂ flake. The top (P₂₁ and P₂₂) and bottom layer grains (P₁₁ and P₁₂) are clearly resolved in the TSM image. The P₂₁ and P₁₁ grains are in a near-pristine 2H stacking. P₂₂ shows an almost identical shear signal as P₁₂ due to their pristine 2H stacking with the same but inversion-asymmetry crystallographic orientation. As the vdW interaction between the top and bottom MoS₂ layer is less than the bonding between the bottom MoS₂ layer and substrate, the difference between shear signals (trace and retrace) of the top layer is larger than that in the bottom layer. The top layer grains are stacked over the bottom layer grains. Whereas no shear contrast is observed within the top layer grains. This result demonstrates that the puckering effect occurs primarily on the top layer, and the corresponding puckering-induced shear signal in the bottom grains should be small.

The top layer-dependent crystallographic orientation imaging of 2D materials enables the crystallographic orientation imaging of bilayer films with TSM. Our research will be beneficial in understanding the nanomechanical behaviors of 2D systems and providing a convenient and powerful approach to facilitate nondestructive crystallographic orientation characterization of 2D atomic crystal systems.

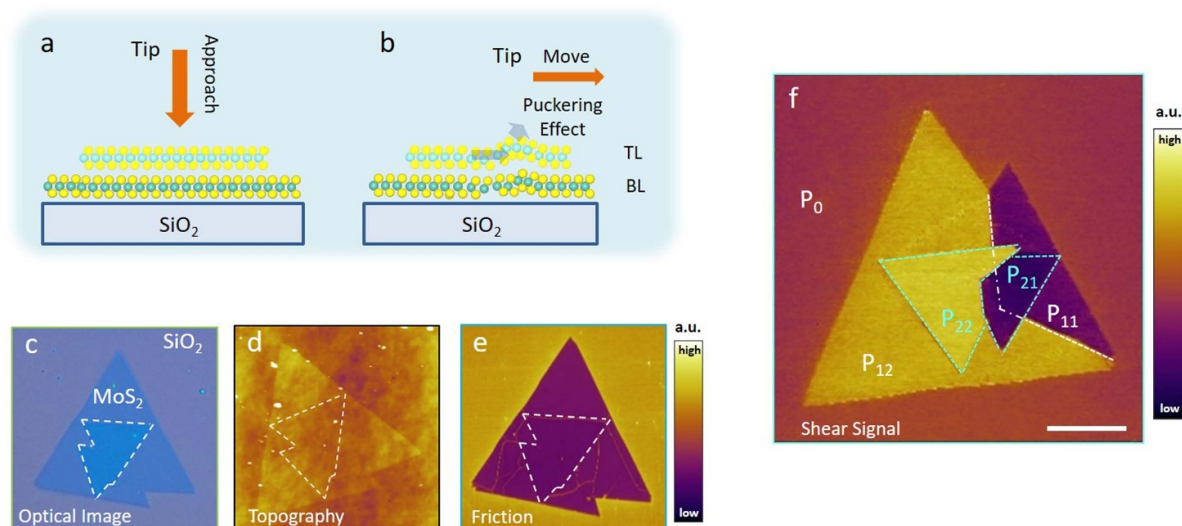


Figure 25. (a), (b) Schematic of the puckering effect occurring on the top layer (TL) of MoS₂ rather than the bottom layer (BL). (c) Optical, (d) AFM topography, (e) FFM, and (f) TSM images of bilayer MoS₂ on the SiO₂/Si substrate. The different MoS₂ grains are marked as P₁₁ and P₁₂ for the bottom monolayer and P₂₁ and P₂₂ for the top layer. P₀ is the amorphous SiO₂/Si substrate. Reproduced from [19], with permission from Springer Nature.

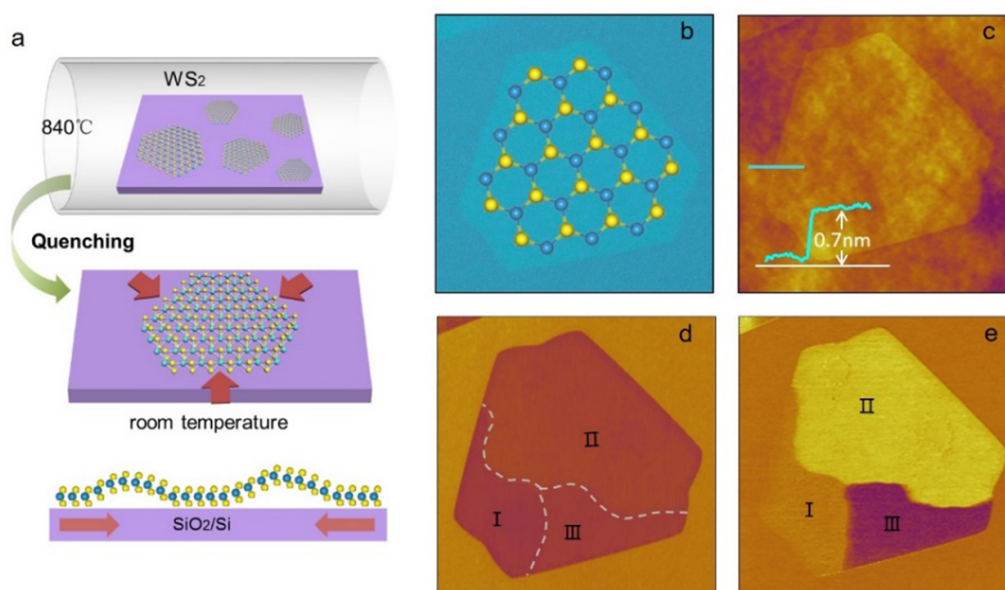


Figure 26. (a) Schematic of CVD growth and cooling process. The in-plane strain is applied onto the WS₂ flake via the underlying amorphous SiO₂/Si substrate. (b) Optical and (c) AFM topography images of the WS₂ flake, scan size: 25 μm \times 25 μm . The cyan line shows the height of the WS₂ monolayer flake. (d) FFM and (e) TSM images of the WS₂ flake. The three rippling domains were marked I, II, and III. Reprinted with permission from [156]. Copyright (2021) American Chemical Society.

2.1.2.2. Strain-induced rippling and manipulation. The strain-engineered rippling structures were reported in TMDCs by several groups. Ripples can strongly influence electronic properties by inducing effective magnetic fields and changing local potentials [168–172]. Here, the nanoscale ripples introduced by the in-plane thermal strain are reported. Using the TEC mismatch between the TMDCs and growth substrate, we can apply built-in strain in TMDCs layers, as shown in figure 26(a).

Figures 26(b) and (c) show the optical and AFM topography images of the typical WS₂ monolayer single-crystal

flake. The quasi-hexagonal shape of WS₂ flakes results from the S/W ratio and growth temperature. In the single-crystal WS₂ monolayer flake, three contrast domains are vaguely and distinctly visualized in the FFM and TSM images (figures 26(d) and (e)), respectively. In the FFM image (figure 26(d)), the dashed line distinguishes the three zigzag-orientated rippling domains with three-equivalent directions. The domains were formed by artificial AFM manipulations based on the pristine WS₂ flake (figure 27).

Figures 27(a)–(c) show the three TSM images of the WS₂ flake with an artificially manipulated single rippling domain.

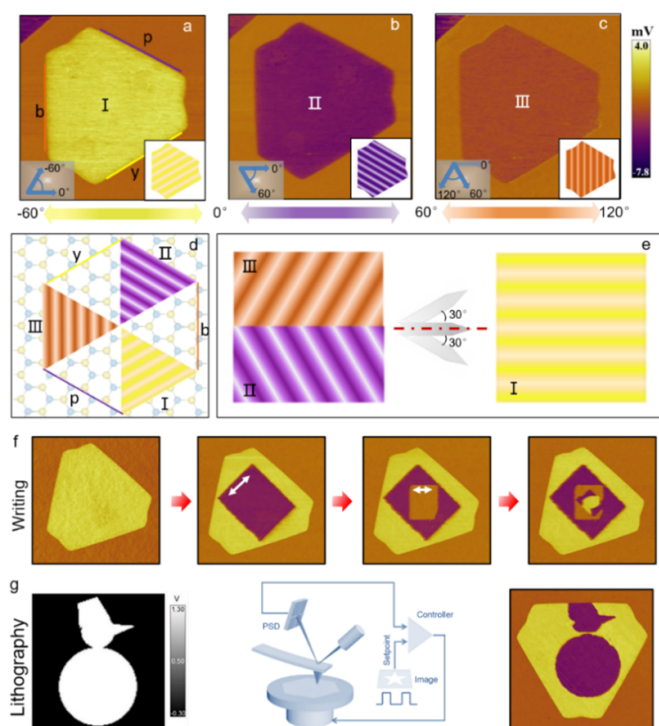


Figure 27. Manipulation of ripple orientation on the monolayer WS_2 flake. (a)–(c) TSM images of single rippling domain in the monolayer WS_2 flake. The insets show the AFM manipulation directions and schematic of the ripple lines in the WS_2 flake. In (a), three straight zigzag edges, labeled y (yellow), b (brown), and p (purple), are parallel to the ripple direction in domains I, II, and III, respectively. (d) Schematic illustrating the three rippling domains with the ripple line orientated along the zigzag crystallographic direction of WS_2 . (e) Schematic of the AFM manipulation directions for the ripple transformation from II and III to I. (f) TSM image of WS_2 monolayer flake with single rippling domain. Three sequential TSM images show the AFM manipulation process in the WS_2 flake in (f). White arrows illustrate the corresponding writing direction. (g) ‘Snowman’ rippling domain pattern formed by the home-modified AFM lithography. The setpoint (i.e. loading force) of the contact AFM scanning is pixel-dependent according to the pre-defined grayscale image. Reprinted with permission from [156]. Copyright (2021) American Chemical Society.

The ripple orientation is illustrated in the inset, and the direction of rippling domain I is horizontal (0°). The AFM manipulation was systematically performed as follows: first, repeated (forward and backward) scanning in contact mode was performed with a certain manipulation scan direction and large loading force (~ 400 nN) on the entire flake. Next, the TSM image was obtained in the horizontal scan direction with a small loading force (~ 0.1 nN) to check the result of the previous manipulation. By incrementally changing the manipulation direction from 0° to 180° , three rippling domains with different contrasts were obtained, labeled type I, II, and III. The ripple direction of type I (II and III) domain was further aligned along the y (b and p) zigzag edge of the WS_2 flake using the angle-dependent TSM images. In our experiments, the rippling domain of type I, II and III can only form by the manipulation directions within the angle interval of $(-30^\circ, 30^\circ)$, $(30^\circ, 90^\circ)$ and $(90^\circ, 150^\circ)$, respectively.

Figure 27(e) describes the conclusion of manipulations: the manipulation is controlled primarily by the angle interval of the target zigzag-orientated ripple lines direction and manipulation directions. The types II or III rippling domain could be transformed to type I using AFM manipulation when the angle interval between manipulation direction and type I ripple direction range from -30° to 30° . Decreasing the angle interval allows successful manipulation using relatively fewer manipulation repeating times and smaller loading force. The direction of the rippling domain is the same if the angle interval between manipulation and pristine ripple direction is less than 30° .

The AFM manipulation based on the above manipulation principle (figures 27(f) and (g)) has fabricated numerous distinctive rippling domain patterns in the monolayer WS_2 flake. Figure 27(f) shows the procedure of writing a matryoshka-like rippling domain pattern. More complicated patterns were ‘painted’ using the AFM lithography method (figure 27(g)). The single rippling domain was first prepared on the entire WS_2 flake and then formed within the flake using contact AFM scanning several times in the home-modified lithography AFM mode.

The artificial rippling domain patterns were stable in the ambient condition and can be imaged after several weeks. Furthermore, the rippling strongly influences the electronic properties of 2D materials by introducing effective periodical local pseudo-magnetic fields and electrical potentials [168, 173]. This strain-engineered ripple and artificially-manipulated rippling domain could further investigate the exotic electron behaviors in the 2D limit.

2.1.2.3. Nanoscratching using AFM probe. It is important to explore the fracture mechanics properties of 2D materials deposited on the substrate. To date, experimental research on fracture mechanics has been conducted on 2D materials, such as the nanoindentation test on exfoliated graphene [174] and MoS_2 [175], and nanoscratch test on graphene, MoS_2 , and h-BN [176].

The comparison of Young’s moduli and breaking strengths of several materials are summarized in table 4. The strength of monolayer MoS_2 is exceeded only by carbon nanotubes and graphene. For a complete cognition of fracture behavior and to deepen the understanding of different fracture stages, nanoscratch with progressive and constant force is conducted, as in figure 28.

Ye *et al* [177] applied a progressive series of forces to perform a scratch along a linear routine on the single-layer MoS_2 , as shown in figure 28(a). The normal load increased from 50 to 70 μN in 20 μm . The experiment result is presented in figures 28(b) and (c), which correspond to the optical image and morphology of the sample after scratch test, respectively.

There is no distinct phenomenon in the sample when the normal load is less than 50 μN , and crack modes in the front and middle exhibit distinctive differences. Two novel crack forms can be triggered according to the magnitude of normal loads. Figure 28(d) shows the middle of the fracture where periodical serrated cracks can be found, thereby implying an anisotropic brittle fracture of the single-layer MoS_2 .

Table 4. Comparison of young's moduli and breaking strengths for several engineering materials. Reprinted with permission from [175]. Copyright (2011) American Chemical Society.

Material	Young's modulus E_{Young} (Gpa)	Breaking strength $\sigma_{\text{max}}^{\text{eff}}$ (Gpa)	Breaking strength/ Young's modulus (%)
Stainless steel ASTM-A514	205	0.9	0.4
Molybdenum	329	0.5–1.2	0.15–0.36
Polyimide	2.5	0.231	9
PDMS	0.3–0.87	2.24	2.5
Kevlar 49	112	3	2.6
Monolayer MoS ₂	270	16–30	6–11
Bulk MoS ₂	238		
WS ₂ nanotubes	152	3.7–16.3	2.4–10
Carbon nanotubes	1000	11–63	1.1–63
Graphene	1000	130	13

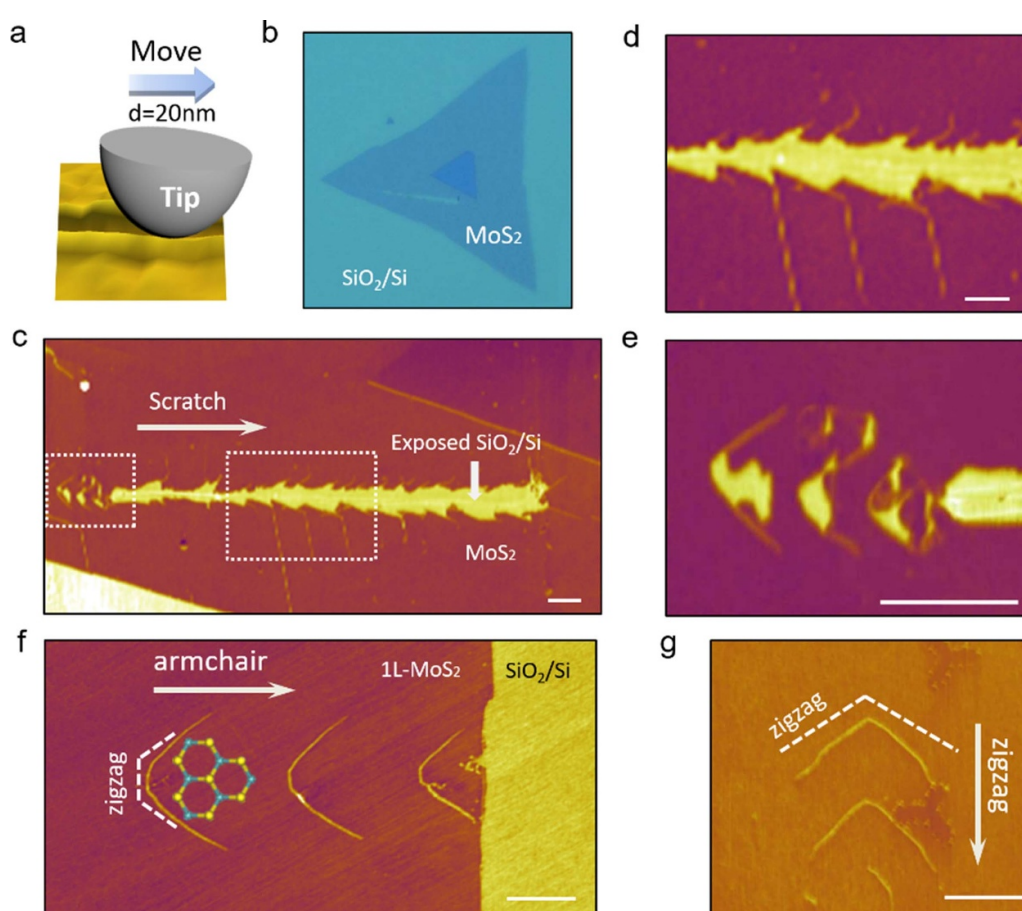


Figure 28. Fracture induced by nanoscratch on single-layer MoS₂. (a) Schematic of nanoscratch using AFM. The apex radius of ~ 10 nm was chosen, which is not too sharp to pierce the film easily nor too blunt to peel such a huge film. (b) Optical image of MoS₂ film after scratch. (c) FFM image of the scratched domain with distinctive crack morphology. Normal load increases from 50 to 70 μN . (d), (e) Close-up of the domain in white dashed frame in (c). In (d), periodical zigzag cracks along the scratch path. In (e), the forefront of the whole fracture. (f) FFM image of a string of cracks along the armchair direction. The scratch is from left to right, as shown by the arrow. The head shape of the crack is flat. (g) String of cracks along the zigzag direction, from up to down. The head shape of the crack is angular. Reproduced from [177]. © IOP Publishing Ltd. All rights reserved. In (c)–(e), scale bars here are 1.0 μm . In (f), (g), scale bars here are 0.5 μm .

Figure 28(e) shows the close-up image of the fracture front, wherein a so-called ‘semi-circular crack’ was generated only under a certain critical load (~ 50 μN).

Under a critical load (~ 50 μN), with an extremely slow scan velocity, arrays of semi-circular cracks were generated,

as shown in figures 28(f) and (g). Figures 28(e) and (f) correspond to nanoscratch tests along the high-symmetric crystallographic orientations (armchair and zigzag). The size and distance between adjacent semi-circular cracks of the two crystallographic orientations are similar. However, the head

shape of cracks along the armchair is flat, whereas that along the zigzag is angular with 120° at the top. Thus, all the directions of the head cracks are consistent with zigzag orientation in this mode. Such a unique crack form originated from the special local stress distribution around the AFM tip [177].

In summary, semi-circular and periodical zigzag cracks in the fracture were generated according to the different loading force, and both present anisotropy in the generation and propagation progress that is helpful for the design of reliable and protective nanoelectronic devices.

2.2. Interfacial charge transfer

Understanding charge generation, transfer, and diffusion between 2D materials and their supporting substrates is important for their potential applications. Lu *et al* [178] observed significant N-doping in thin MoS₂ films on SiO₂, dominated by charge traps at the sample – substrate interface by STM. Further, the charge trapping and its effects on the characteristics of the MoS₂ field-effect transistors and photodetection devices were investigated [179, 180]. Liu *et al* [181] claimed to generate anomalously high DC using a sliding Schottky nano-contact in a sliding semiconductor-metal contact (on MoS₂ multilayers/Ag).

Kim *et al* [182] investigated the triboelectric charges of a graphene/SiO₂ system and found trapped triboelectric charges at the air–SiO₂ interface underneath the graphene that act as ghost floating gates. KPFM was used to measure the SP before and after triboelectrification (figures 29(a)–(c)). Figure 29(b) shows the initial equipotential state of the CVD graphene before rubbing. Figure 29(c) shows the SP after rubbing the central square; the rubbed region has a ~ 50 mV higher SP than the unrubbed region. Such potential variation may not be attributed to charges stored in the graphene as electric charges are localized for long times only in insulating materials. Some generated charges tunnel through the monolayer graphene and are locally trapped on the underlying insulator. The trapped charges act as an immaterial (made of charges-only and not of a conductor) bottom floating gate and locally change the polarity and density of charges in the graphene and its work function. The ghost floating gates effectively control the carriers within graphene because of the thin graphene and comparably thin air gap.

ΔV_{TT} is defined as the SP taken with reference to the average SP of the unrubbed region. Figure 29(d) shows the averaged ΔV_{TT} along the black dashed line of figure 29(c) taken after 0 and 72 h of rubbing. It is observed that the potential variation is well preserved even after 72 h. Figure 29(e) shows the averaged ΔV_{TT} as a function of time:

$$\Delta V_{TT}(t) \propto 4\text{mV} \times e^{\frac{-t}{\tau_{\text{short}}}} + 46\text{mV} \times e^{\frac{-t}{\tau_{\text{long}}}}. \quad (34)$$

In practice, in addition to a small term of shorter time constant ($\tau_{\text{short}} \sim 3$ h and 21 min), there is a dominant term with higher initial amplitude and exceptionally long time constant ($\tau_{\text{long}} \sim 278$ h). Herein, τ_{long} is more than two orders of magnitude than that of the standard triboelectrification. The immaterial ghost gates effectively control the charges inside the

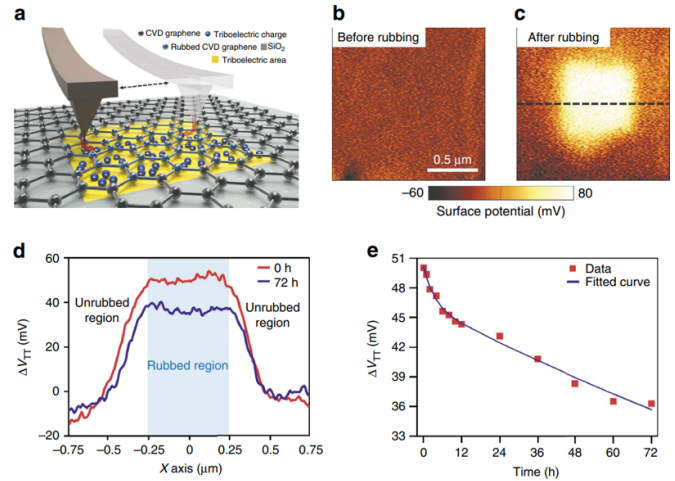


Figure 29. (a) Schematic of the friction process and KPFM measurement system. KPFM image of graphene (b) before and (c) after rubbing. (d) Potential difference generated by tunneling triboelectrification, ΔV_{TT} , along the blue dashed line in (c) after 0 and 72 h; ΔV_{TT} is well preserved even after 72 h. (e) ΔV_{TT} as a function of time. The best fit (blue line) is the sum of two decaying exponential terms, each with its own time constant. Reproduced from [182]. CC BY 4.0.

graphene owing to the thin 2D materials and sub-nanometer insulating air gap.

Recently, the charges transfer and diffusion of the MoS₂/SiO₂ interface through contact and frictional electrification were investigated systematically *in-situ* using SKPM and DH-EFM (figure 30). In the contact electrification process, the contact voltages applied by the tip and the positive or negative charges can be transferred to MoS₂/SiO₂ with the PtSi-coated AFM tip. The micro-process of contact electrification in the MoS₂/SiO₂ system is shown in figure 30(a). This process can be divided into two steps: first, the biased tip is in contact with the center of MoS₂ and forms an equipotential MoS₂ flake. Second, the generated interface dipole moments act as floating gates. The image charges on SiO₂ can be induced by the charges on MoS₂ flakes by considering the air gap between them. The joint action of charges on MoS₂ and their image charges forms the dipole moments at the MoS₂/SiO₂ interface. The effect of these interface dipole moments is evident in the DH-EFM images.

The decay process of the charges on MoS₂/SiO₂ is monitored by the SP evolution, as shown in figures 30(e)–(i). Figure 30(e) shows the SP of the uncharged sample. We simultaneously applied -4 V on MoS₂ and SiO₂ to compare the decay process of charges on MoS₂/SiO₂ with that on SiO₂. Figures 30(f)–(i) show a series of SP images taken in the same areas after tip contact sample. The apparent area of charged regions becomes larger and the intensity becomes weaker.

Figure 30(b) shows the evolution of SP value with time. The discharge process of MoS₂/SiO₂ is much longer than that of the SiO₂ surface. The decay time τ is obtained using $\Delta_{SP} \propto V_0 \times e^{\frac{-t}{\tau}}$, where Δ_{SP} is defined as the SP taken with reference to the average SP of the intact SiO₂ region. V_0 is a constant, which equals the initial SP difference Δ_{SP0} [182, 183]. The

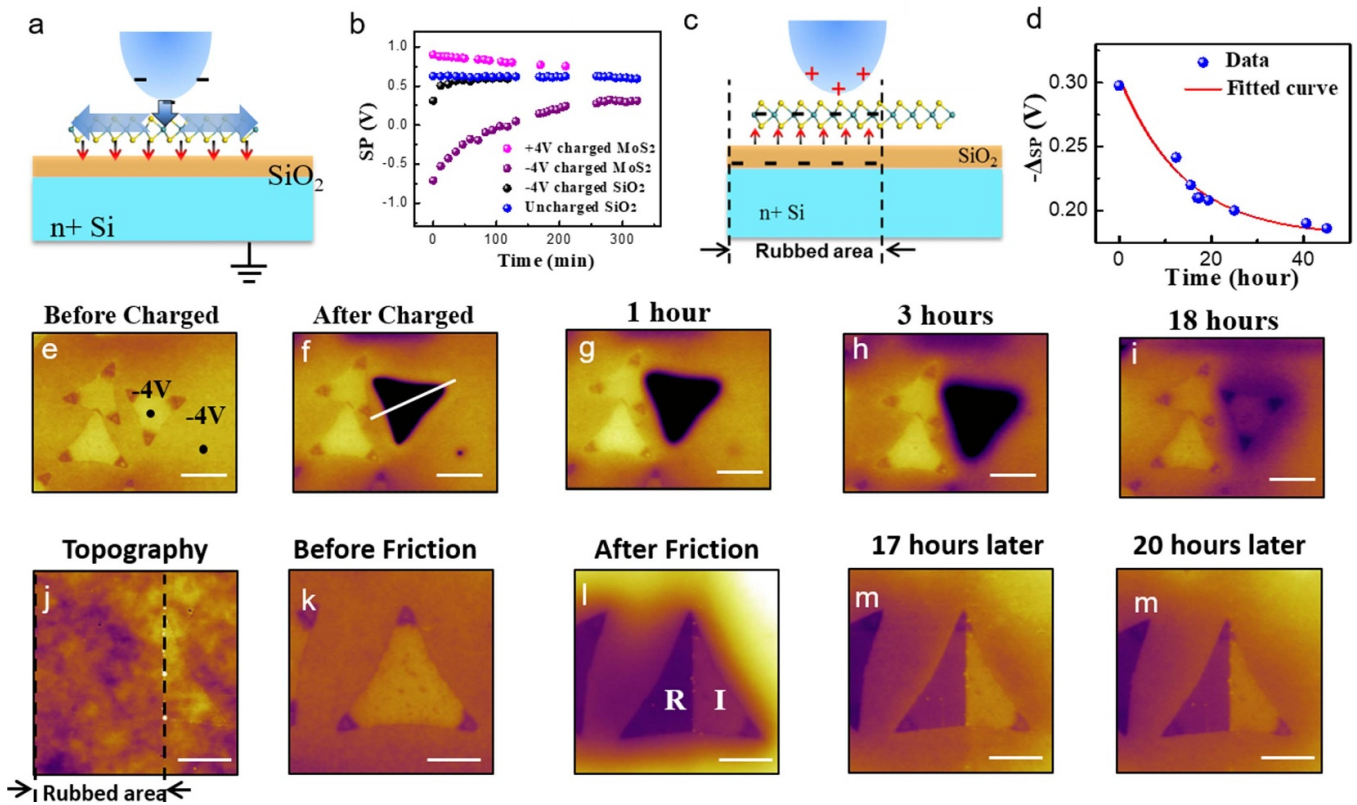


Figure 30. (a) Schematic of charge transfer with tip and MoS₂/SiO₂ contacting. (b) Profiles of SP vs. time. (c) Schematic of charge transfer between the tip and MoS₂/SiO₂ with tip friction on MoS₂/SiO₂. (d) Profiles of ΔSP vs. time. (e) MoS₂ SP before charging. Contact voltages applied by the AFM tip are marked. (f)–(i) Series of SP images taken in the same region after biased tip contacting MoS₂. (e)–(i) Scale bars are 5 μ m. (j) AFM topography of MoS₂ on SiO₂/Si substrates after rubbing. Rubbed area is marked. (k) SP images of the neutral sample. (l)–(n) AFM images of MoS₂ layer after triboelectrification, showing a sharp edge between rubbed (marked R) and intact (marked I) MoS₂. (j)–(m) Scale bars are 4 μ m. Reproduced from [30]. © IOP Publishing Ltd. All rights reserved.

decay time of -4 and $+4$ V charged MoS₂/SiO₂ is ~ 1.98 and 2.42 h, respectively. Overall, the τ for the MoS₂/SiO₂ areas is one order of magnitude larger than that of the contact electrification SiO₂ surface.

The longer τ on MoS₂/SiO₂ confirms that the transferred charges are trapped at the MoS₂/SiO₂ interface because the discharge process is related to the water molecules and atmospheric ions [184]. When the charge is trapped at MoS₂/SiO₂ interface, the water molecules cannot effectively contribute to deelectrification due to the MoS₂ layers. The discharge process of interfacial charges depends primarily on the charge transfer in SiO₂ bulk. Hence, τ is larger in the MoS₂/SiO₂ system. Furthermore, τ depends on the sign of charged voltages. Thus, the τ of $+4$ V charged flake is larger than that of the -4 V charged flake owing to the different charge diffusion coefficients of positive and negative charges in SiO₂/Si.

Additionally, the characterization of frictional electrification on MoS₂/SiO₂ was studied (figures 30(j)–(m)). Figure 30(j) shows the topography after rubbing. Figures 30(k) and (l) show the SP image of the sample before and after rubbing. The contrast between R and I areas can be observed even after 80 h. The rubbed areas are negatively charged. The

Fermi surface of tip is higher than that of SiO₂ and MoS₂, thus resulting in electron transfer from tip to sample. The nonuniform SP on SiO₂ substrate may originate from the charged impurities from the air deposited on the substrate.

The corresponding schematic of charge transfer is shown in figure 30(c). The ΔSP of rubbed MoS₂ area vs. time is plotted in figure 33(d). The τ is ~ 14.10 h for the rubbed MoS₂/SiO₂. The charge decay time of the MoS₂/SiO₂ interface is one (or two) order of magnitudes larger than that of the SiO₂ surface. The longer τ confirms the transferred charges are trapped at MoS₂/SiO₂ interface. Due to the screen effect of MoS₂ layers, water molecules or other atmospheric ions cannot effectively contribute to deelectrification, thereby resulting in a longer τ of interface charges [30].

In addition to the semiconductor/insulator interface, the metal/insulator (M/I) interface was also investigated (figure 31). The charges transfer at M/I interface (figure 31(a)) is as follows. Electron flows from the material with higher Fermi level E_F (smaller work function φ) to the one with lower E_F (larger φ). Electron is trapped at the insulator surface when the work function satisfies $\varphi_I > \varphi_M$. The interfacial dipole moments (indicated by red arrows) collect at the M/I interface owing to the air gap between the insulator

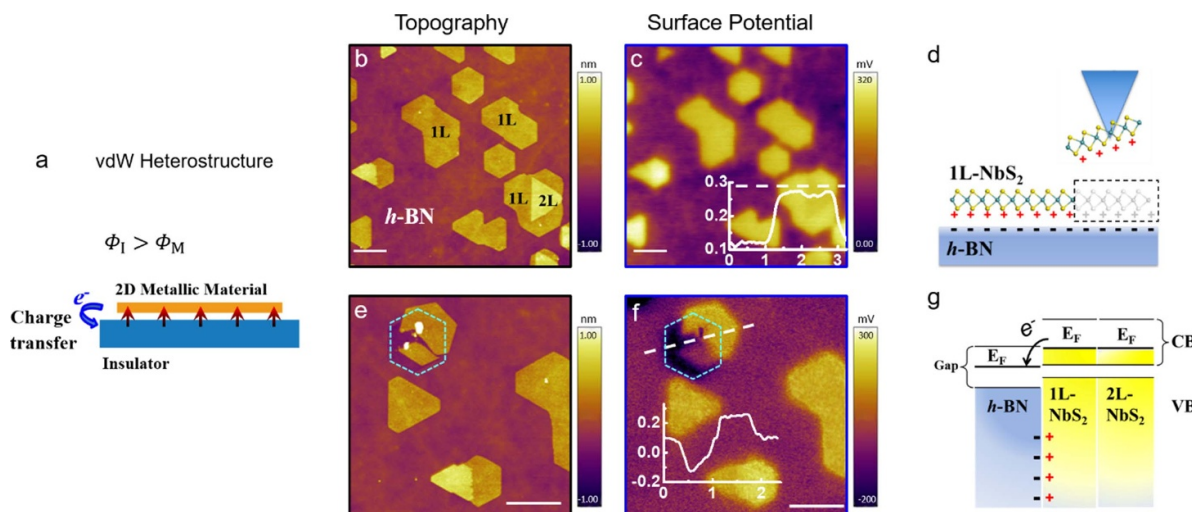


Figure 31. (a) Charge transfer between the 2D metal layer and insulator. (b), (c) AFM topography and SP of NbS₂/BN using SKPM. Inset: SP profiles along dash lines in (c). (d) Schematic of post-exposed *h*-BN surface preparation. Post-exposed *h*-BN surface is the *h*-BN surface covered by NbS₂ in the growth process but exposed after peeling the NbS₂ using AFM tips. NbS₂ layers framed by the dashed box stand for the stripped part before peeling. Charge distribution at the 1L-NbS₂/BN interface and post-exposed *h*-BN surface is also shown. (e) AFM topography after partly peeling NbS₂, the dash hexagon shows the position of the NbS₂ layer before peeling. (f) SP image of the post-exposed *h*-BN surface. Inset: SP profiles along the dash lines in (f). (g) Schematic energy band diagram of NbS₂/BN showing electron transfer from 1L-NbS₂ to *h*-BN. Scale bars are 1 μ m. Reproduced from [92]. © IOP Publishing Ltd. All rights reserved.

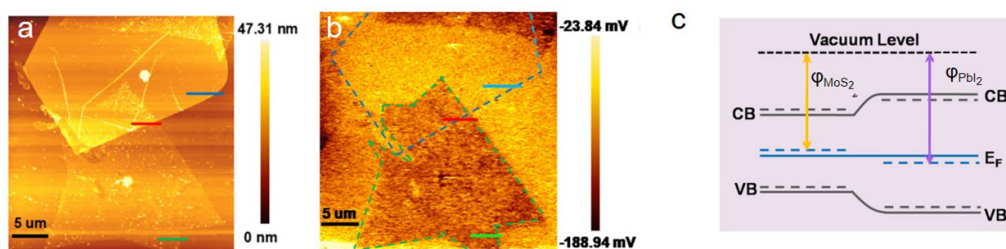


Figure 32. (a) AFM and (b) KPFM images of the MoS₂/PbI₂ heterostructures. (c) Schematic of band energy of MoS₂/PbI₂ heterostructures. Reproduced from [185], with permission from Springer Nature.

and 2D metal. The NbS₂/BN heterostructure was obtained using CVD on SiO₂/Si substrate to identify the M/I interface charge transfer.

Figure 31(b) shows the topography of CVD-grown NbS₂/BN heterostructures. The NbS₂ layers grow on the *h*-BN substrate in a layered fashion with atomic smoothness. We call the initial growth layer the first layer (1L-NbS₂) and the following layers the second (2L-) and third (3L-) NbS₂ layer [92]. Figure 31(c) shows that the 1L-NbS₂ SP is larger than that of *h*-BN and 2L-NbS₂ by ~ 130 and 10 mV, respectively. The SP difference between 1L-NbS₂ and *h*-BN indicates charge transfer between NbS₂ and *h*-BN interface, as demonstrated in figure 31(g).

An AFM probe was used as a manipulator to peel part of NbS₂ flakes to obtain post-exposed *h*-BN surface and ‘see’ the interfacial charge transfer (figure 31(d)). A vertical knocking was applied on the NbS₂ layers with AFM tip in AC (tapping) mode. The NbS₂ layer is broken into several small lamellas with sufficiently strong vertical tapping, and the post-exposed *h*-BN surface is obtained, as shown in figure 31(e). Figure 31(f) shows the post-exposed *h*-BN surface SP as ~ 236 mV, lower than that of pristine *h*-BN. The negative

charges accumulate at the post-exposed *h*-BN surface considering the neutral pristine *h*-BN surface.

Ding *et al* [185] used SKPM to characterize the SP of MoS₂/PbI₂ heterostructures. In figure 32, a significant change in SP in the interlayer between MoS₂ and PbI₂ suggest interface charge transfer and electron transfer from MoS₂ to PbI₂.

To summarize, SKPM and advanced EFM aid the study of interfacial electrons transfer and diffusion. The material properties can be adjusted by interface engineering and motivate further directive studies on the heterointerface of heterostructures.

2.3. Interface intercalation

Interfacial engineering, such as molecule or ion intercalations, can modify properties and optimize heterostructures and their device performances. For example, Bediako *et al* reported that lithium-ion intercalation at individual atomic interfaces motivates using vdW heteroepitaxy to realize new engineered functional interfaces for energy conversion and storage by manipulating the ion storage modes and ‘job-sharing’ characteristics of hybrid electrodes [186].

Moreover, the intercalation of atoms and molecules has been studied for h-BN monolayers [187, 188] and other 2D materials, such as graphene [189], to modify the materials' properties. Yamasue *et al* synthesized hydrogen-intercalated graphene on a 4H-SiC(0001) substrate. Hydrogen intercalation at the interface eliminates covalent bonds and the original quasi-(6 × 6) corrugation, which indicates the conversion of the buffer layer into a second graphene layer by terminating Si bonds at the interface.

As water is an anomalous liquid, the water intercalation at the interface of heterostructures has attracted considerable attention. Lee *et al* [190] reported that H₂O intercalating between graphene and mica increases the friction between the tip and substrate depending on the water and graphene layer thickness. Figure 33 illustrates the water intercalated single-layer graphene (SLG) and bilayer graphene (BLG) on mica. The topography and friction images in figures 33(c) and (d) show the regions of mica, SLG + zero water layers (0 W), SLG + first water layers (1 W), and SLG + second water layers (2 W). The brighter contrast in figures 33(b) and (d) suggests high friction. The FFM images show increased friction by the water layer intercalation between graphene and mica. The friction enhancement in BLG is less visible than that in SLG but is higher than that on the BLG + 0 W on mica, as shown in figures 33(d) and (f). Figure 33(g) shows a schematic of varied friction over graphene layers with and without intercalated water using an AFM tip. Additionally, they reported that D₂O intercalation decreases friction at the H₂O-intercalated graphene on mica because the low rate of frictional kinetic energy dissipation at the interface affects the phonon contribution.

Hong *et al* [191] investigated the effects of the trapped interfacial ice-like water layer on the charge transfer between graphene and SiO₂/Si substrate by recording the SP changes induced by partial removal of the water layer upon *in-situ* heating. Figures 34(a)–(d) illustrate the *in-situ* AFM height images of the graphene–interfacial water layer–SiO₂/Si sandwich system at different temperatures. No noticeable change is observed below 40 °C (figure 34(b)), whereas the interfacial water layer is partially removed at 80 °C (figure 34(c)). A further increase in temperature removes the interfacial water layer (figure 34(d)). Interfacial water molecules fail to penetrate the impermeable graphene sheet, allowing the water molecules at the graphene edge to easily escape upon heating (figure 34(e)). The same height of 0.37 ± 0.02 nm is measured for the interfacial water layer (figure 34(g)), which indicates an ice-like single water layer underneath the graphene. The contrast in the SP map between the 1L₁WL and 1L₀WL graphene regions shows the effects of the interfacial water layer on graphene SP (figure 34(f)). The work function of graphene is calculated by $\varphi_G = \varphi_{\text{tip}} - eV_{\text{CPD}}$, where φ_{tip} and V_{CPD} are the work functions of the AFM tip and contact potential difference between the AFM tip and graphene measured by SKPM. The SKPM mapping shows electronically modified graphene by the ice-like water layer as the electron density transfers from graphene to the water layer, resulting in graphene hole-doping.

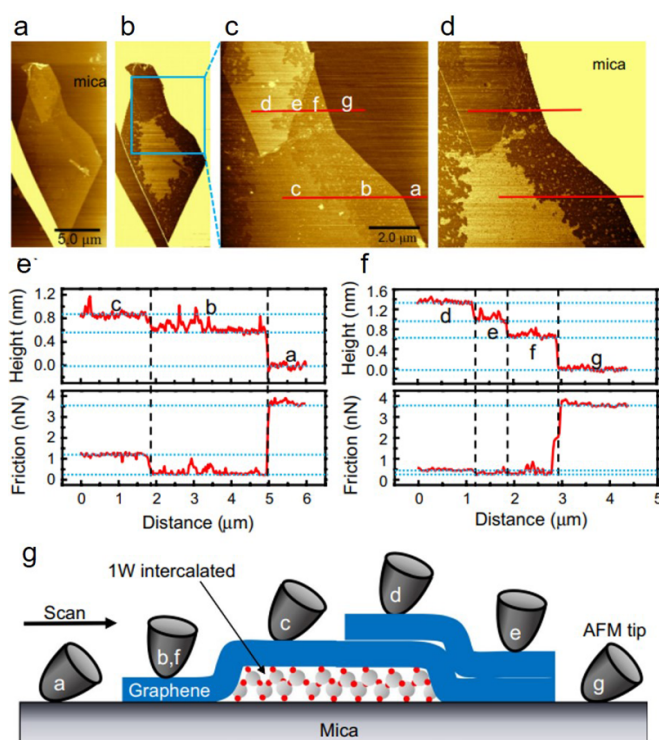


Figure 33. (a), (b) Topography and friction images ($11 \mu\text{m} \times 24 \mu\text{m}$) of water-intercalated graphene on mica after mechanical cleavage in air. (c), (d) Magnified topography and friction images ($7 \mu\text{m} \times 7 \mu\text{m}$) from the blue box in (b), where the labels represent a bare mica, b SLG, c SLG + 1 W, d BLG + 1 W, e BLG, f SLG, and g bare mica. (e), (f) Section line of the height and friction along the red lines in (c) and (d). (g) Schematic showing the variable friction behavior using an AFM tip, depending on the sublayer composition. Labels (a)–(g) in the tips match areas (a)–(g) in (c). Reproduced from [190], with permission from Springer Nature.

The water layers confined between hydrophobic/hydrophobic interfaces under ambient conditions have been studied by our group [73]. A special folding few-layers graphene film was elaborately prepared (figure 35(a)) to form a hydrophobic/hydrophobic interface. We precool the sample with constant temperature and humidity equipment for several hours before placing the sample in a warm and high humidity condition to realize H₂O intercalation at the whole interface. Because the MF-AFM amplitude (A_{MF}) can reflect the local mechanical properties of the sample and has subsurface detection capability (figure 35(b)), the internal interfacial intercalation water phases were further visualized with two MF-AFM modes: multi-harmonic and dual AC AFM.

The subsurface information obtained through nanomechanical coupling between the tip and sample helps distinguish between the two types of water phases via the higher harmonic $A_{6\text{th}}$ detection (figure 35(d)). Essentially, the elastic modulus increases for higher $A_{6\text{th}}$ values. The corresponding histogram in figure 35(e) is extracted from figure 35(d). The larger (smaller) elastic modulus areas, corresponding to the bright (dark) areas in $A_{6\text{th}}$, represent the solid (liquid)-like phase of the intercalation water layers.

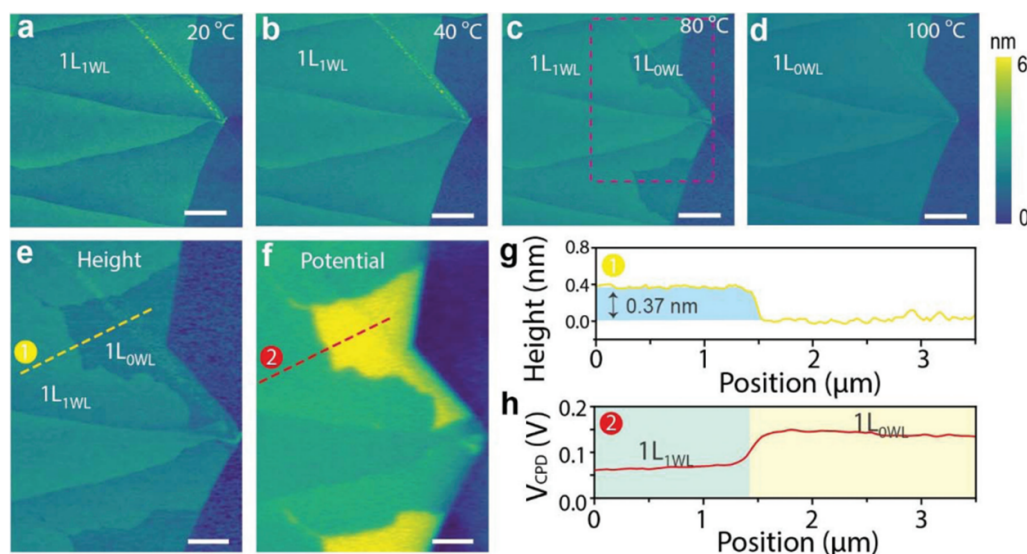


Figure 34. (a)–(d) Recorded *in-situ* AFM height images of graphene supported on SiO₂/Si substrate from room temperature (25 °C) to 100 °C. The scale bars are 2 μm. (e) Magnified AFM height image and (f) corresponding SP recorded by SKPM at 80 °C. The scale bars are 1 μm. (g) Height and (h) V_{CPD} line profiles measured along the yellow and red dashed lines marked in (e) and (f), respectively. Reproduced from [191] with permission from the Royal Society of Chemistry.

Figure 35(g) shows the A₂ images of the water intercalated sample and the corresponding histogram distribution in figure 35(h). Two kinds of water structures coexist at the folding graphene interface. The higher A₂ (brighter contrast) indicates the strong repulsive (rigid) and less dissipated tip–sample forces, which reflects the solid-like phase. In contrast, the dark areas with lower A₂ reflect a liquid-like phase considering their soft and dissipative nature.

The experimental data of A_{6th} and A₂ demonstrate coexisting solid- and liquid-like water phases at the interface. The internal interfacial structures affect the solid and liquid layers, which confirm intercalated water layers at the interface. The distribution rates of the two phases are almost the same in the A_{6th} image. However, in the A₂ image, the distribution rates are ~60% for solid- and ~40% for liquid-like phases. This discrepancy arises because the tip–sample force is weaker in multi-harmonic mode (passive MF-AFM mode) than in dual AC mode (active MF-AFM mode).

Depending on the density, the liquid phase is divided into low-density liquid (LDL) and high-density liquid (HDL). Considering the fragility indices, LDL ($m = 14$) is a ‘superstrong’ liquid whereas HDL ($m = 20$ – 25) is relatively weak. Combining the MF-AFM data analysis and above discussion, phases of liquid water were determined using elastic modulus. LDL has a larger elastic modulus (solid-like phase) than the HDL (liquid-like phase).

Figure 36 shows the water molecules’ intercalation at the M/I interface and related metal–insulator transition (MIT) of the first layer (1L) NbS₂ in NbS₂/BN heterostructure. The sample was first precooled and then detected by AFM to monitor the H₂O molecule’s intercalation into the interface. Sequential AFM topography snapshots are shown in figures 36(a)–(d). Initially, partial H₂O molecules gather around 1L-NbS₂, whereas some islands of H₂O molecules

discretely distribute on the *h*-BN surface (figure 36(a)). H₂O molecules epitaxially grow from the intercalated H₂O layer and discretely distributed island until the *h*-BN surface is covered by water layers (figures 36(b)–(d)).

The water patches and films appear as one/two puckered bilayers of ice-I_h in the section lines of the same area (figure 36(e)) [92, 192]. The 2L-NbS₂ height remains unchanged before and after water adsorption. We conclude that except at the intercalation at NbS₂/BN interface, the interface between 1L- and 2L-NbS₂ is free from water owing to the absence of charge transfer and dipole moments between the two layers.

The electrical properties of water-intercalated samples were further investigated using DH-EFM and sMIM. Compared to the mobile charge carrier (MCC) images of the pristine sample (figure 36(h)), 1L-NbS₂ is ‘invisible’ and has an identical signal with the insulating H₂O/BN surface after water intercalation, as highlighted by the dotted lines in figure 36(i). This indicates the MIT of the 1L-NbS₂ layer when intercalating the H₂O layer at the 1L-NbS₂/BN heterointerface. The 2L-NbS₂ layer can be observed in MCC images, which indicates the preserved metallic state of 2L-NbS₂ by the buffering effect of the 1L-NbS₂ layer. Additionally, figure 36(j) shows that the SP of water-intercalated NbS₂/BN heterostructures is ~120 mV lower than that at H₂O/BN surface.

sMIM images of pristine and water intercalated samples are shown in figures 36(k)–(n). Compared to the metallic behavior of the pristine sample (figures 36(k) and (l)), the 1L-NbS₂ disappears (figure 36(n), marked by the white dash line) and shows electrical insulation. The 2L-NbS₂ continues to show the metallic state, consistent with the MCC image. This confirms MIT of the 1L-NbS₂ layers when intercalating the H₂O layer at the 1L-NbS₂/BN interface.

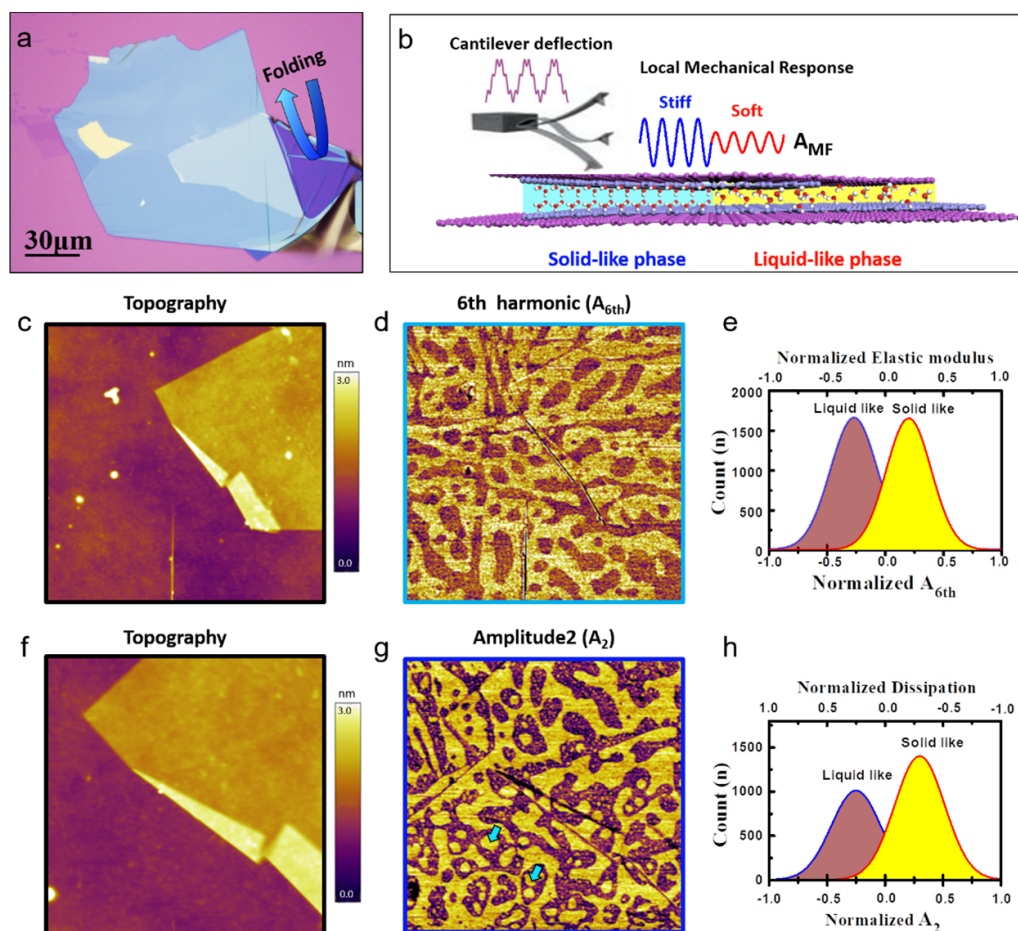


Figure 35. (a) Optical microscopic image of the mechanically exfoliating folding few-layers graphene flake on SiO₂/Si substrate. It can encapsulate water molecules because of its mechanical strength and chemical stability. (b) Basic principle of MF-AFM. The MF-AFM amplitude (A_{MF}) reflects the local mechanical properties (e.g. elastic modulus and viscoelasticity) of the sample and has subsurface detection capability. MF-AFM observes the different phase structures of intercalated water layers. (c), (d) Topography and A_{6th} image of water intercalated sample in multi-harmonic mode. Scan size: 30 μm . (e) Histogram distribution of A_{6th} /elastic modulus extracted from (d). Arbitrarily units (a.u.) qualitatively describe A_{6th} /elastic modulus of the interfacial water layer. (f), (g) Topography and A_2 image of the water intercalated sample in dual AC mode. Scan size: 15 μm . (h) Histogram distribution of A_2 /dissipation extracted from (g). Reproduced from [73], with permission from Springer Nature.

Dollekamp *et al* [193] tuned the friction of graphene by changing the size and vibrational modes of the intercalated molecules. They replaced water with larger alcohol molecules of different vibrational modes, e.g. stretching the C–C and C–O bonds. The extra vibrational modes contribute to the higher friction in methanol, ethanol, and 2-propanol compared to an intercalated double water layer, which scales with their size. In addition, the single-layer graphene has higher friction than bilayer and trilayer graphene.

To summarize, interfacial intercalation can tune the local physical properties of the sample by changing the environmental conditions and intercalated interface molecules. These results suggest manipulating the electronic/mechanical properties of 2D materials for diverse applications.

2.4. Interfacial thermology

Thermal measurements require nanoscale spatial resolution and high sensitivity. SThM can successfully determine the

thermal conductivity, k , of samples [194]. For example, the in-plane k of a residue-free suspended graphene bridge was measured using NP-SThM with spatial resolution reaching 50 nm [144]. The temperature profile of suspended graphene bridges was measured and fitted with the 1D heat transfer equation to obtain k . Hwang and Kwon [195] used NP-SThM to obtain the in-plane k of suspended graphene disks of radius 50–3680 nm.

In addition, the thermal transport of heterostructures could be studied by SThM. The heater-sample thermal contact resistance (R_X) of graphene/MoS₂ heterostructure is given in figure 37(a). The sample has areas of bare SiO₂/Si (SOS), graphene on SiO₂ (GS), MoS₂ on SiO₂ (MS), and MoS₂ on GS (MGS). The contrast in the R_X image demonstrates the following trend from low to high thermal resistance areas. $R_X(\text{GS}) < R_X(\text{SOS}) < R_X(\text{MGS}) < R_X(\text{MS})$. This is because the interfacial thermal resistance plays a role in thermal transport in addition to the layer thermal conductivity [196]. The MS interface exhibited an R_X between 4×10^{-8} and

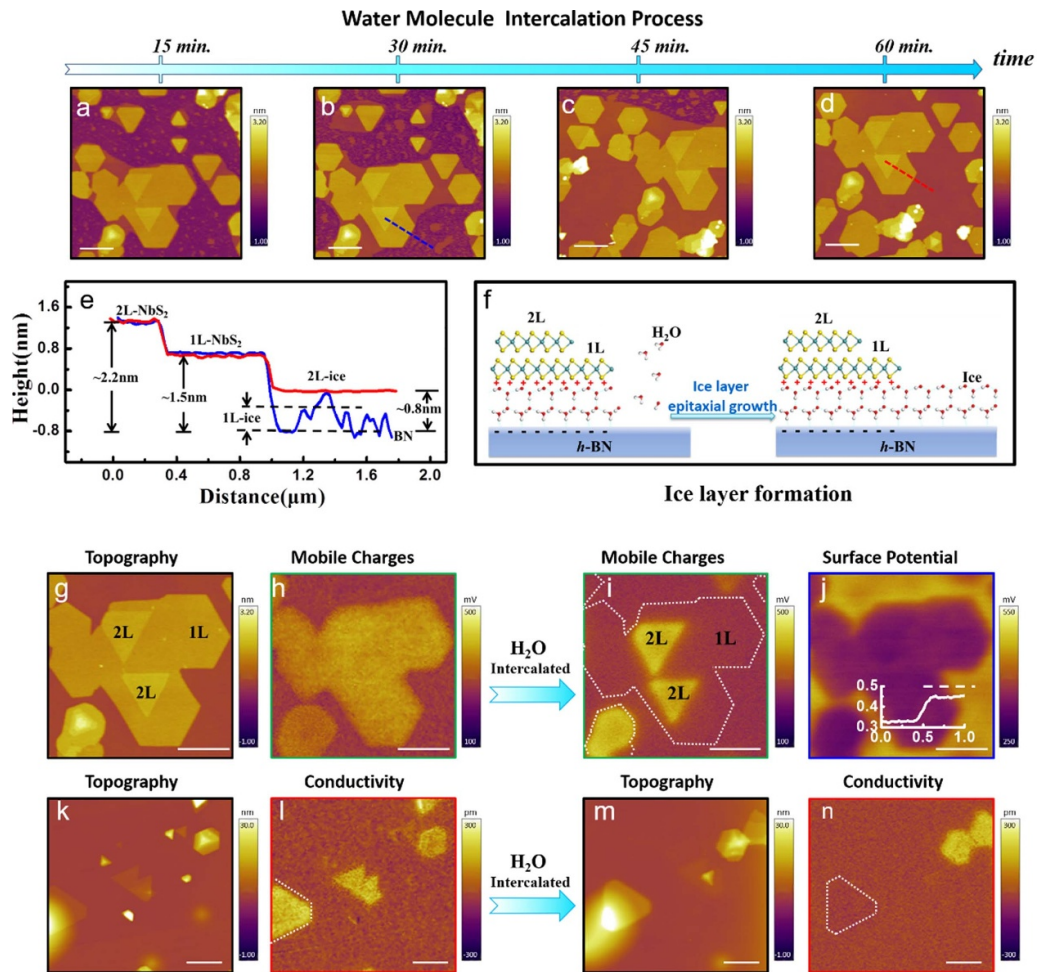


Figure 36. (a)–(d) Water molecules intercalate at the interface and grow on the sample surface. (e) Section lines during (blue line) and after (red line) water intercalation. (f) Schematic of evolution process and structure diagram of water molecule intercalation at the 1L-NbS₂/BN heterointerface. (g), (h) AFM topography and MCC images of pristine NbS₂/BN heterostructures. (i), (j) MCC and SP images of water-intercalated heterostructures. (k)–(n) Topography and conductivity images of (k), (l) pristine and (m), (n) water-intercalated NbS₂/BN heterostructures using sMIM mode. Scale bars are 1 μm . Reproduced from [92]. © IOP Publishing Ltd. All rights reserved.

$2.27 \times 10^{-6} \text{ m}^2 \text{ KW}^{-1}$ [197, 198], which is higher than that of GS (between 5.6×10^{-9} and $2 \times 10^{-8} \text{ m}^2 \text{ KW}^{-1}$) [199]. Thus, the thermal resistance of GS is increased by one order of magnitude by adding MoS₂ top layer, thereby providing pathways for increasing the efficiency of thermoelectric applications using vdW materials.

Additionally, the spatial distribution of temperature rise within the lateral heterostructure was studied [201]. The optical and AFM images (figure 37(c)) of a MoS₂–WS₂ lateral heterostructure confirm a single monolayer sample. The compositional heterogeneity of this device is illustrated by the Raman map in figure 37(d). SThM maps the temperature rise spatial distribution within the monolayer TMDC devices during a high electrical power dissipation through a lateral interface (figures 37(e) and (f)). The results directly demonstrate that lateral heterojunctions between MoS₂ and WS₂ fail to impact the heat dissipation distribution, whereas GBs of MoS₂ considerably localize heating in the device.

Special physical phenomena could be observed when applying SThM. Xu *et al* [53] observed a novel mechanical-thermal coupling effect in monolayer/bilayer MoS₂, and WS₂ films; essentially, puckering deformation can enhance interfacial TR (figure 38). Figure 38(a) shows the FFM images of monolayer/bilayer MoS₂ with increasing normal forces. Figure 38(b) shows the corresponding friction signals vs. normal forces. The AFM tip's normal force applied to the sample surface can controllably modulate the magnitude of puckering deformations, which facilitates corresponding frictional and thermal response detection. Corresponding to the FFM images, the *in-situ* dynamic TR images of the monolayer/bilayer MoS₂ sample are shown in figure 38(c). The lighter contrast stands for a larger TR. Under normal forces, the dynamic TRs of the monolayer/bilayer MoS₂ sample is enhanced. The corresponding relative dynamic/static TR vs. normal force (relative to the substrate with no puckering effect) are drawn in figure 38(d). Compared with the static TRs, the dynamic

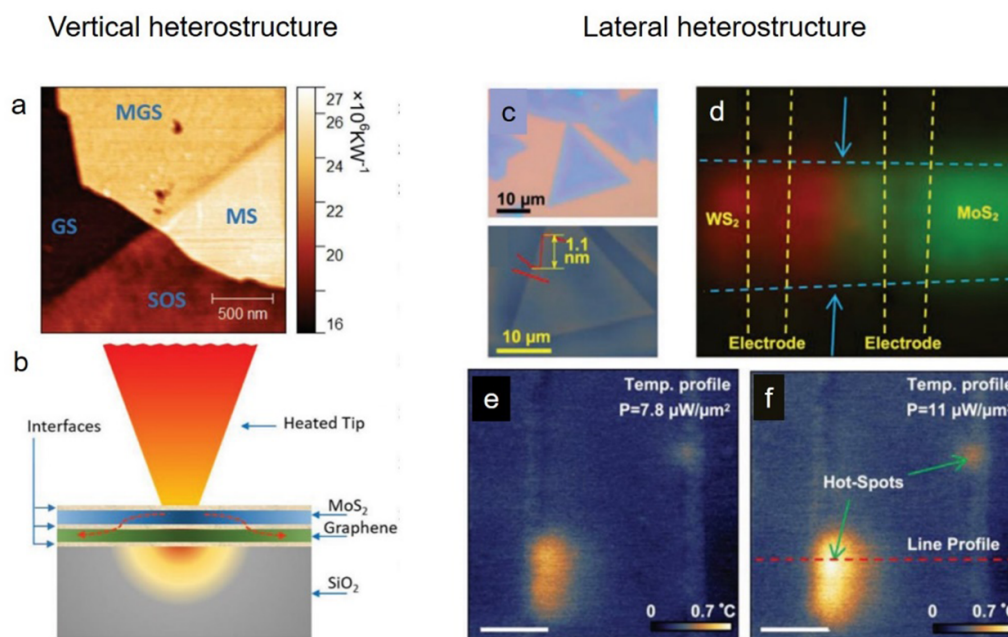


Figure 37. (a) Heater-sample thermal contact resistance (R_X) image acquired at $T_S = 220$ K for different areas of interest. (b) Schematic of the heat transport from the tip to the substrate through 2D structures. [200] John Wiley & Sons. [© 2019 WILEY-VCH Verlag GmbH & Co. KGaA, Weinheim]. (c) Optical and AFM images of a MoS_2 - WS_2 heterostructure. (d) Raman map of the MoS_2 - WS_2 heterostructure device. (e), (f) Temperature rise profiles in this device at different dissipated electrical power at $V_G = +60$ V. The heating predominantly occurs on the WS_2 -metal vertical junction, and the lateral interface does not contribute to heat localization. The green arrows in (f) show the hot-spot position. [201] John Wiley & Sons. [© 2019 WILEY-VCH Verlag GmbH & Co. KGaA, Weinheim].

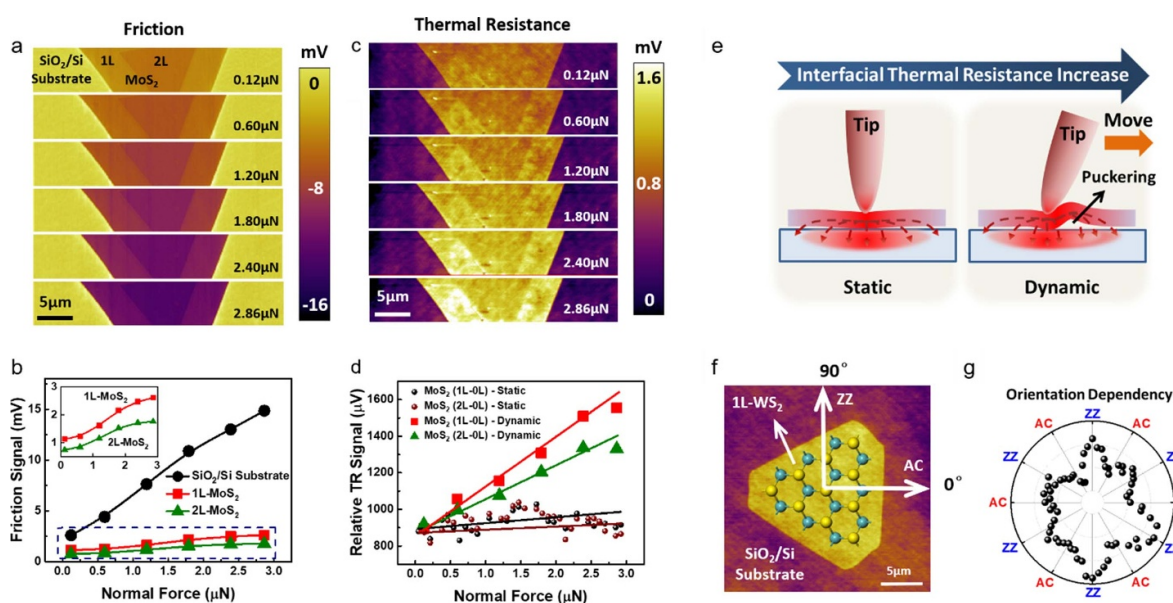


Figure 38. (a) Series of friction images of the MoS_2 with increasing normal force. (b) The curves of the friction signals of the sample and substrate vs. normal forces. Data are extracted from (a). Inset is the enlarged view of the dashed rectangle. The 0L, 1L, and 2L represent the substrate, monolayer film, and bilayer film, respectively. (c) Series of *in-situ* TR images of the MoS_2 with increasing normal force, corresponding to (a). (d) Relative dynamic/static thermal resistances vs. normal forces. Data are extracted from (c). Resistance values are the difference values of the sample and substrate. (e) Schematic illustration of static and dynamic TR principle. (f) Thermal resistance image of WS_2 . The crystallographic orientations of armchair (AC) and zigzag (ZZ) based on the primitive growth edges of WS_2 are marked. (g) Polar diagram of the relative dynamic thermal resistance vs. crystallographic orientation of 1L- WS_2 . The relative dynamic TR values are extracted from SThM images by changing the scan angles. Reproduced from [53] with permission from the Royal Society of Chemistry.

TRs of 1L- and 2L-MoS₂ rapidly increases with increasing normal forces. The results suggest that puckering deformations modulated by normal forces contribute to increasing dynamic TRs.

The principle of static and dynamic TR is illustrated in figure 38(e). After contact, the thermal contact area increases with increasing normal force owing to the elastic compression, which reduces the static and dynamic TR. However, as the dynamic contact scan can induce puckering deformation, a slight interface gap exists between the top layer and substrate, which impacts longitudinal heat transfer with additional dynamic interfacial TR. Therefore, dynamic TR is higher than static TR (with no puckering deformation) under the same normal force.

Furthermore, the crystallographic orientation-dependent anisotropy of the puckering effect in the atomically thin 2D crystal was demonstrated using SThM (figures 38(f) and (g)). The puckering deformation causes in-plane stress redistribution, thus breaking the original in-plane stiffness. These findings are significant to optimize the nanoscale tribological/thermal design and dynamic mechanical-thermal management of 2D materials in nanoelectronics.

3. Conclusion and perspectives

This review highlighted the principles of functional AFM methods and their applications in 2D materials. AFM-based physical characterization methods require the researchers to have clear natural science concepts and electronic circuit knowledge. In TSM, the enhanced sensitivity to elastic deformation properties of crystals can reveal the crystallographic orientation of samples. The nonlinear sample information can be obtained using multifrequency force microscopy. KPFM can detect the sample work function, whereas EFM can explore the carrier concentration, electrostatic gradient, and MCC. In sMIM, the dielectric constant, doping density, conductivity, and permittivity of the sample surface and sub-surface can be obtained (semi-) quantitatively when combined with FEA analysis.

The AFM modes require further development and improvement in the applied research on the surface/interface of 2D materials. For example, (i) the single physical property measurement method has limitations because the electrical properties are coupled with other properties. Therefore, a method that can explore the mechanical-thermal-electrical-optical coupling is needed. (ii) The functional AFM technology under vacuum conditions needs further improvement. Obtaining quantitative data is difficult as AFM detection in the atmospheric environment is inevitably affected by the water molecules. In addition, the functional AFM technology involves complex signal transmission of microwave or light waves, which results in unsatisfactory manufacturing costs and stability of functional AFM technology under vacuum conditions. (iii) Improving the application of 2D materials and optimizing device performance requires understanding the properties under work conditions. A method that can measure physical properties under work conditions is crucial for

future research. With the development of AFM technology and 2D material preparation, we expect increased achievements in this field.

Acknowledgments

This project was supported by the National Natural Science Foundation of China (NSFC) (Nos. 61911540074, 61674045, 11604063, 11622437, 11974422, and 12172047), the Ministry of Science and Technology (MOST) of China (Nos. 2016YFA0200700 and 2018YFE0202700). Z H C acknowledges the support of the Strategic Priority Research Program of the Chinese Academy of Sciences (CAS) (No. XDB30000000). Z H C and W J received Fundamental Research Funds for the Central Universities and Research Funds of Renmin University of China (Nos. 21XNLG27 and 19XNQ025).

ORCID iD

Zhihai Cheng  <https://orcid.org/0000-0003-4938-4490>

References

- [1] Voigtlander B 2019 *Atomic Force Microscopy* (Berlin: Springer) (<https://doi.org/10.1007/978-3-030-13654-3>)
- [2] Bhushan B 2010 *Handbook of Nanotechnology* (Berlin: Springer) (<https://doi.org/10.1007/978-3-642-02525-9>)
- [3] Binnig G, Rohrer H, Gerber C and Weibel E 1982 Surface studies by scanning tunneling microscopy *Phys. Rev. Lett.* **49** 57–61
- [4] Binnig G, Rohrer H, Gerber C and Weibel E 1983 7×7 reconstruction on Si (111) resolved in real space *Phys. Rev. Lett.* **50** 120–3
- [5] Belianinov A, Kalinin S V and Jesse S 2015 Complete information acquisition in dynamic force microscopy *Nat. Commun.* **6** 6550
- [6] Jang S K, Youn J, Song Y J and Lee S 2016 Synthesis and characterization of hexagonal boron nitride as a gate dielectric *Sci. Rep.* **6** 30449
- [7] Zheng Z, Xu R, Ye S, Hussain S, Ji W, Cheng P, Li Y, Sugawara Y and Cheng Z 2017 High harmonic exploring on different materials in dynamic atomic force microscopy *Sci. China Technol. Sci.* **61** 446–52
- [8] Benstetter G, Biberger R and Liu D P 2009 A review of advanced scanning probe microscope analysis of functional films and semiconductor devices *Thin Solid Films* **517** 5100–5
- [9] Horcas I, Fernandez R, Gomez-Rodriguez J M, Colchero J, Gomez-Herrero J and Baro A M 2007 WSXM: a software for scanning probe microscopy and a tool for nanotechnology *Rev. Sci. Instrum.* **78** 013705
- [10] Binnig G, Quate C F and Gerber C 1986 Atomic force microscope *Phys. Rev. Lett.* **56** 930
- [11] Albrecht T R, Grütter P, Horne D and Rugar D 1991 Frequency modulation detection using high-Q cantilevers for enhanced force microscope sensitivity *J. Appl. Phys.* **69** 668–73
- [12] Bettac A, Koeble J, Winkler K, Uder B, Maier M and Feltz A 2009 QPlus: atomic force microscopy on single-crystal insulators with small oscillation amplitudes at 5 K *Nanotechnology* **20** 264009

- [13] Groning O *et al* 2018 Engineering of robust topological quantum phases in graphene nanoribbons *Nature* **560** 209–13
- [14] Ruffieux P *et al* 2016 On-surface synthesis of graphene nanoribbons with zigzag edge topology *Nature* **531** 489–93
- [15] Zhang J, Chen P, Yuan B, Ji W, Cheng Z and Qiu X 2013 Real-space identification of intermolecular bonding with atomic force microscopy *Science* **342** 611–4
- [16] Yacoot A and Koenders L 2008 Aspects of scanning force microscope probes and their effects on dimensional measurement *J. Phys. D: Appl. Phys.* **41** 103001
- [17] Hussain S *et al* 2020 Strain-induced hierarchical ripples in MoS₂ layers investigated by atomic force microscopy *Appl. Phys. Lett.* **117** 153102
- [18] Xu K *et al* 2019 Shear anisotropy-driven crystallographic orientation imaging in flexible hexagonal two-dimensional atomic crystals *Appl. Phys. Lett.* **115** 063101
- [19] Hussain S *et al* 2021 Toplayer-dependent crystallographic orientation imaging in the bilayer two-dimensional materials with transverse shear microscopy *Front. Phys.* **16** 53504
- [20] Garcia R and Herruzo E T 2012 The emergence of multifrequency force microscopy *Nat. Nanotechnol.* **7** 217–26
- [21] Yablon D G 2013 *Scanning Probe Microscopy in Industrial Applications* (New York: Wiley)
- [22] Shaw J E, Perumal A, Bradley D D C, Stavrinou P N and Anthopoulos T D 2016 Nanoscale current spreading analysis in solution-processed graphene oxide/silver nanowire transparent electrodes via conductive atomic force microscopy *J. Appl. Phys.* **119** 195501
- [23] Houz   F, Meyer R, Schneegans O and Boyer L 1996 Imaging the local electrical properties of metal surfaces by atomic force microscopy with conducting probes *Appl. Phys. Lett.* **69** 1975–7
- [24] Yang J, Gordiichuk P, Zheliuk O, Lu J, Herrmann A and Ye J 2017 Role of defects in tuning the electronic properties of monolayer WS₂ grown by chemical vapor deposition *Phys. Status Solidi* **11** 1700302
- [25] Zhang L and Mitani Y 2006 Structural and electrical evolution of gate dielectric breakdown observed by conductive atomic force microscopy *Appl. Phys. Lett.* **88** 032906
- [26] Mi S, Guo J, Wang H, Xia T and Cheng Z 2022 Scanning kelvin probe microcopy study of magnetic topological insulators MnBi₂Te₄(Bi₂Te₃)_n *Chin. J. Vac. Sci. Technol.* **42** 585–92
- [27] Filleter T, Emtsev K V, Seyller T and Bennewitz R 2008 Local work function measurements of epitaxial graphene *Appl. Phys. Lett.* **93** 133117
- [28] Wen H F, Li Y J, Arima E, Naitoh Y, Sugawara Y, Xu R and Cheng Z H 2017 Investigation of tunneling current and local contact potential difference on the TiO₂(110) surface by AFM/KPFM at 78K *Nanotechnology* **28** 105704
- [29] Shen Y, Zhang X Q, Wang Y, Zhou X J, Hu J, Guo S W and Zhang Y 2013 Charge transfer between reduced graphene oxide sheets on insulating substrates *Appl. Phys. Lett.* **103** 053107
- [30] Xu R *et al* 2018 Nanoscale charge transfer and diffusion at the MoS₂/SiO₂ interface by atomic force microscopy: contact injection versus triboelectrification *Nanotechnology* **29** 355701
- [31] Wen H F, Adachi Y, Zhang Q Z, Miyazaki M, Sugawara Y and Li Y J 2019 Identification of atomic defects and adsorbate on rutile TiO₂(110)-(1 × 1) surface by atomic force microscopy *J. Phys. Chem. C* **123** 25756–60
- [32] Wen H F, Sugawara Y and Li Y J 2020 Multi-channel exploration of O adatom on TiO₂(110) surface by scanning probe microscopy *Nanomaterials* **10** 1506
- [33] Wen H F, Sugawara Y and Li Y J 2021 Exploring the nature of hydrogen of rutile TiO₂(110) at 78 K *Surf. Interfaces* **26** 101339
- [34] Yan L, Punckt C, Aksay I A, Mertin W and Bacher G 2011 Local voltage drop in a single functionalized graphene sheet characterized by Kelvin probe force microscopy *Nano Lett.* **11** 3543–9
- [35] Lucchesi M, Privitera G, Labardi M, Prevosto D, Capaccioli S and Pingue P 2009 Electrostatic force microscopy and potentiometry of realistic nanostructured systems *J. Appl. Phys.* **105** 054301
- [36] Datta S S, Strachan D R, Mele E J and Johnson A T C 2009 Surface potentials and layer charge distributions in few-layer graphene films *Nano Lett.* **9** 7–11
- [37] Oliveira C K, Matos M J S, Mazzoni M S C, Chacham H and Neves B R A 2012 Anomalous response of supported few-layer hexagonal boron nitride to DC electric fields: a confined water effect? *Nanotechnology* **23** 175703
- [38] Collins L, Kilpatrick J I, Weber S A L, Tselev A, Vlasiouk I V, Ivanov I N, Jesse S, Kalinin S V and Rodriguez B J 2013 Open loop Kelvin probe force microscopy with single and multi-frequency excitation *Nanotechnology* **24** 475702
- [39] Li C, Ding X D and Lin G C 2013 Study on multi-frequency method for electrostatic force microscopy in air *Integr. Ferroelectr.* **145** 59–67
- [40] Jiang Y, Qi Q, Wang R, Zhang J, Xue Q K, Wang C, Jiang C and Qiu X H 2011 Direct observation and measurement of mobile charge carriers in a monolayer organic semiconductor on a dielectric substrate *ACS Nano* **5** 6195–201
- [41] Wu D *et al* 2015 Thickness-dependent dielectric constant of few-layer In₂Se₃ nanoflakes *Nano Lett.* **15** 8136–40
- [42] Feng Y *et al* 2015 Synthesis of large-area highly crystalline monolayer molybdenum disulfide with tunable grain size in a H₂ atmosphere *ACS Appl. Mater. Interfaces* **7** 22587
- [43] Liu Y *et al* 2015 Thermal oxidation of WSe₂ nanosheets adhered on SiO₂/Si substrates *Nano Lett.* **15** 4979–84
- [44] Kundhikanjana W, Lai K, Wang H, Dai H, Kelly M A and Shen Z-X 2009 Hierarchy of electronic properties of chemically derived and pristine graphene probed by microwave imaging *Nano Lett.* **9** 3762–5
- [45] Berweger S, Blanchard P T, Brubaker M D, Coakley K J, Sanford N A, Wallis T M, Bertness K A and Kabos P 2016 Near-field control and imaging of free charge carrier variations in GaN nanowires *Appl. Phys. Lett.* **108** 073101
- [46] Brinciotti E *et al* 2015 Probing resistivity and doping concentration of semiconductors at the nanoscale using scanning microwave microscopy *Nanoscale* **7** 14715–22
- [47] Lu A-Y *et al* 2017 Janus monolayers of transition metal dichalcogenides *Nat. Nanotechnol.* **12** 744–9
- [48] Kim S K, Bhatia R, Kim T-H, Seol D, Kim J H, Kim H, Seung W, Kim Y, Lee Y H and Kim S-W 2016 Directional dependent piezoelectric effect in CVD grown monolayer MoS₂ for flexible piezoelectric nanogenerators *Nano Energy* **22** 483–9
- [49] Park M, Hong S, Kim J, Hong J and No K 2011 Nanoscale ferroelectric switching behavior at charged domain boundaries studied by angle-resolved piezoresponse force microscopy *Appl. Phys. Lett.* **99** 142909
- [50] Kim S, Gopalan V and Gruverman A 2002 Coercive fields in ferroelectrics: a case study in lithium niobate and lithium tantalate *Appl. Phys. Lett.* **80** 2740–2
- [51] Hartmann U 1999 Magnetic force microscopy *Annu. Rev. Mater. Sci.* **29** 53–87

- [52] Sidles J A, Garbini J L, Bruland K J, Rugar D, Züger O, Hoen S and Yannoni C S 1995 Magnetic resonance force microscopy *Rev. Mod. Phys.* **67** 249–65
- [53] Xu K, Ye S, Lei L, Meng L, Hussain S, Zheng Z, Zeng H, Ji W, Xu R and Cheng Z 2018 Dynamic interfacial mechanical-thermal characteristics of atomically thin two-dimensional crystals *Nanoscale* **10** 13548–54
- [54] Maletinsky P, Hong S, Grinolds M, Hausmann B, Lukin M D, Walsworth R L, Loncar M and Yacoby A 2012 A robust scanning diamond sensor for nanoscale imaging with single nitrogen-vacancy centres *Nat. Nanotechnol.* **7** 320–4
- [55] Tetienne J-P, Rondin L, Spinicelli P, Chipaux M, Debuisschert T, Roch J-F and Jacques V 2012 Magnetic-field-dependent photodynamics of single NV defects in diamond: an application to qualitative all-optical magnetic imaging *New J. Phys.* **14** 103033
- [56] Huxter W S, Palm M L, Davis M L, Welter P, Lambert C-H, Trassin M and Degen C L 2022 Scanning gradiometry with a single spin quantum magnetometer *Nat. Commun.* **13** 3761
- [57] Grinolds M S, Hong S, Maletinsky P, Luan L, Lukin M D, Walsworth R L and Yacoby A 2013 Nanoscale magnetic imaging of a single electron spin under ambient conditions *Nat. Phys.* **9** 215–9
- [58] Song T *et al* 2021 Direct visualization of magnetic domains and moiré magnetism in twisted 2D magnets *Science* **374** 1140–4
- [59] Ariyaratne A, Bluvstein D, Myers B A and Jayich A C B 2018 Nanoscale electrical conductivity imaging using a nitrogen-vacancy center in diamond *Nat. Commun.* **9** 2406
- [60] Bian K, Zheng W, Zeng X, Chen X, Stohr R, Denisenko A, Yang S, Wrachtrup J and Jiang Y 2021 Nanoscale electric-field imaging based on a quantum sensor and its charge-state control under ambient condition *Nat. Commun.* **12** 2457
- [61] Appel P, Ganzhorn M, Neu E and Maletinsky P 2015 Nanoscale microwave imaging with a single electron spin in diamond *New J. Phys.* **17** 112001
- [62] Kucsko G, Maurer P C, Yao N Y, Kubo M, Noh H J, Lo P K, Park H and Lukin M D 2013 Nanometre-scale thermometry in a living cell *Nature* **500** 54–58
- [63] Dazzi A and Prater C B 2017 AFM-IR: technology and applications in nanoscale infrared spectroscopy and chemical imaging *Chem. Rev.* **117** 5146–73
- [64] Bazylewski P, Ezugwu S and Fanchini G 2017 A review of three-dimensional scanning near-field optical microscopy (3D-SNOM) and its applications in nanoscale light management *Appl. Sci.* **7** 973
- [65] Huth F, Govyadinov A, Amarie S, Nuansing W, Keilmann F and Hillenbrand R 2012 Nano-FTIR absorption spectroscopy of molecular fingerprints at 20 nm spatial resolution *Nano Lett.* **12** 3973
- [66] Choi J S *et al* 2011 Friction anisotropy-driven domain imaging on exfoliated monolayer graphene *Science* **333** 607–10
- [67] McNeill C 2011 Imaging the domain structure of organic semiconductor films *J. Polym. Sci.* **49** 909–19
- [68] Kalihari V, Tadmor E B, Haugstad G and Frisbie C D 2008 Grain orientation mapping of polycrystalline organic semiconductor films by transverse shear microscopy *Adv. Mater.* **20** 4033
- [69] Martinez-Martin D, Herruzo E T, Dietz C, Gomez-Herrero J and Garcia R 2011 Noninvasive protein structural flexibility mapping by bimodal dynamic force microscopy *Phys. Rev. Lett.* **106** 198101
- [70] Vasudevan R K, Okatan M B, Rajapaksa I, Kim Y, Marincel D, Trollet-mckinstry S, Jesse S, Valanoor N and Kalinin S V 2013 Higher order harmonic detection for exploring nonlinear interactions with nanoscale resolution *Sci. Rep.* **3** 2677
- [71] Tetard L, Passian A and Thundat T 2010 New modes for subsurface atomic force microscopy through nanomechanical coupling *Nat. Nanotechnol.* **5** 105
- [72] Cheng Z, Zheng Z and Xu R 2016 Multi-frequency atomic force microscopy *Sci. Sin. Technol.* **46** 437–50
- [73] Zheng Z-Y, Xu R, Xu K-Q, Ye S-L, Pang F, Lei L, Hussain S, Liu X-M, Ji W and Cheng Z-H 2019 Real-space visualization of intercalated water phases at the hydrophobic graphene interface with atomic force microscopy *Front. Phys.* **15** 23601
- [74] Nievergelt A P, Adams J D, Odermatt P D and Fantner G E 2014 High-frequency multimodal atomic force microscopy *Beilstein J. Nanotechnol.* **5** 2459
- [75] Dietz C, Schulze M, Voss A, Riesch C and Stark R W 2015 Bimodal frequency-modulated atomic force microscopy with small cantilevers *Nanoscale* **7** 1849–56
- [76] Zheng Z-Y *et al* 2020 Local probe of the interlayer coupling strength of few-layers SnSe by contact-resonance atomic force microscopy *Front. Phys.* **15** 63505
- [77] Rabe U and Arnold W 1994 Acoustic microscopy by atomic force microscopy *Appl. Phys. Lett.* **64** 1493–5
- [78] Yamanaka K and Nakano S 1996 Ultrasonic atomic force microscope with overtone excitation of cantilever *Jpn. J. Appl. Phys.* **35** 3787–92
- [79] Yamanaka K, Kobari K and Tsuji T 2008 Evaluation of functional materials and devices using atomic force microscopy with ultrasonic measurements *Jpn. J. Appl. Phys.* **47** 6070–6
- [80] Li Q, Jesse S, Tselev A, Collins L, Yu P, Kravchenko I, Kalinin S V and Balke N 2015 Probing local bias-induced transitions using photothermal excitation contact resonance atomic force microscopy and voltage spectroscopy *ACS Nano* **9** 1848–57
- [81] Yablon D G, Gannepalli A, Proksch R, Killgore J, Hurley D C, Grabowski J and Tsou A H 2012 Quantitative viscoelastic mapping of polyolefin blends with contact resonance atomic force microscopy *Macromolecules* **45** 4363–70
- [82] Gannepalli A, Yablon D G, Tsou A H and Proksch R 2011 Mapping nanoscale elasticity and dissipation using dual frequency contact resonance AFM *Nanotechnology* **22** 355705
- [83] Nonnenmacher M, Oboyle M P and Wickramasinghe H K 1991 Kelvin probe force microscopy *Appl. Phys. Lett.* **58** 2921–3
- [84] Jacobs H O, Leuchtmann P, Homan O J and Stemmer A 1998 Resolution and contrast in Kelvin probe force microscopy *J. Appl. Phys.* **84** 1168–73
- [85] Hsu J W P, Ng H M, Sergeant A M and Chu S N G 2002 Scanning Kelvin force microscopy imaging of surface potential variations near threading dislocations in GaN *Appl. Phys. Lett.* **81** 3579–81
- [86] Ren J, Liess H-D, Mackel R and Baumgartner H 1995 Scanning Kelvin microscope: a new method for surface investigations *Fresenius J. Anal. Chem.* **353** 303–6
- [87] Collins L, Jesse S, Balke N, Rodriguez B J, Kalinin S and Li Q 2015 Band excitation Kelvin probe force microscopy utilizing photothermal excitation *Appl. Phys. Lett.* **106** 104102
- [88] Guo S L, Kalinin S V and Jesse S 2012 Open-loop band excitation Kelvin probe force microscopy *Nanotechnology* **23** 125704
- [89] Melitz W, Shen J, Kummel A C and Lee S 2011 Kelvin probe force microscopy and its application *Surf. Sci. Rep.* **66** 1–27
- [90] Strelcov E, Arble C, Guo H X, Hoskins B D, Yulaev A, Vlaskiuk I V, Zhitenev N B, Tselev A and Kolmakov A

- 2020 Nanoscale mapping of the double layer potential at the graphene- electrolyte interface *Nano Lett.* **20** 1336–44
- [91] Hussain S, Xu K, Ye S, Lei L, Liu X, Xu R, Xie L and Cheng Z H 2019 Local electrical characterization of two-dimensional materials with functional atomic force microscopy *Front. Phys.* **14** 33401
- [92] Xu R *et al* 2019 Interfacial water intercalation-induced metal-insulator transition in NbS₂/BN heterostructure *Nanotechnology* **30** 205702
- [93] De Wolf P, Stephenson R, Trenkler T, Clarysse T, Hantschel T and Vandervorst W 2000 Status and review of two-dimensional carrier and dopant profiling using scanning probe microscopy *J. Vac. Sci. Technol. B* **18** 361–8
- [94] Girard P 2001 Electrostatic force microscopy: principles and some applications to semiconductors *Nanotechnology* **12** 485–90
- [95] Zhang K, Marzari N and Zhang Q 2013 Covalently functionalized metallic single-walled carbon nanotubes studied using electrostatic force microscopy and dielectric force microscopy *J. Phys. Chem. C* **117** 24570–8
- [96] Kimura K, Kobayashi K, Yamada H and Matsushige K 2003 Two-dimensional dopant profiling by scanning capacitance force microscopy *Appl. Surf. Sci.* **210** 93–98
- [97] Kobayashi K, Yamada H and Matsushige K 2004 Method and apparatus for measuring values of physical property *US Patent* 6823724B1
- [98] Ding X D, An J, Xu J B, Li C and Zeng R Y 2009 Improving lateral resolution of electrostatic force microscopy by multifrequency method under ambient conditions *Appl. Phys. Lett.* **94** 223109
- [99] Fumagalli L, Esteban-Ferrer D, Cuervo A, Carrascosa J L and Gomila G 2012 Label-free identification of single dielectric nanoparticles and viruses with ultraweak polarization forces *Nat. Mater.* **11** 808–16
- [100] Li N, Shang Y, Xu R, Jiang Q, Liu J, Wang L, Cheng Z and Ding B 2019 Precise organization of metal and metal oxide nanoclusters into arbitrary patterns on DNA origami *J. Am. Chem. Soc.* **141** 17968–72
- [101] Collins L, Kilpatrick J I, Vlasiouk I V, Tselev A, Weber S A L, Jesse S, Kalinin S V and Rodriguez B J 2014 Dual harmonic Kelvin probe force microscopy at the graphene-liquid interface *Appl. Phys. Lett.* **104** 133103
- [102] Martin Y, Abraham D W and Wickramasinghe H K 1988 High-resolution capacitance measurement and potentiometry by force microscopy *Appl. Phys. Lett.* **52** 1103–5
- [103] Lai K, Ji M B, Leindecker N, Kelly M A and Shen Z X 2007 Atomic-force-microscope-compatible near-field scanning microwave microscope with separated excitation and sensing probes *Rev. Sci. Instrum.* **78** 063702
- [104] Lai K, Kundhikanjana W, Kelly M and Shen Z X 2008 Modeling and characterization of a cantilever-based near-field scanning microwave impedance microscope *Rev. Sci. Instrum.* **79** 063703
- [105] Yang Y, Lai K, Tang Q, Kundhikanjana W, Kelly M A, Zhang K, Shen Z-X and Li X 2012 Batch-fabricated cantilever probes with electrical shielding for nanoscale dielectric and conductivity imaging *J. Microelect. Microeng.* **22** 115040
- [106] Lai K, Kundhikanjana W, Kelly M A and Shen Z X 2008 Calibration of shielded microwave probes using bulk dielectrics *Appl. Phys. Lett.* **93** 123105
- [107] Seabron E, MacLaren S, Xie X, Rotkin S V, Rogers J A and Wilson W L 2016 Scanning probe microwave reflectivity of aligned single-walled carbon nanotubes: imaging of electronic structure and quantum behavior at the nanoscale *ACS Nano* **10** 360–8
- [108] Lai K, Peng H, Kundhikanjana W, Schoen D T, Xie C, Meister S, Cui Y, Kelly M A and Shen Z-X 2009 Nanoscale electronic inhomogeneity in In₂Se₃ nanoribbons revealed by microwave impedance microscopy *Nano Lett.* **9** 1265–9
- [109] Lai K, Nakamura M, Kundhikanjana W, Kawasaki M, Tokura Y, Kelly M A and Shen Z-X 2010 Mesoscopic percolating resistance network in a strained manganite thin film *Science* **329** 190–3
- [110] Kundhikanjana W, Lai K, Kelly M A and Shen Z-X 2011 Cryogenic microwave imaging of metal-insulator transition in doped silicon *Rev. Sci. Instrum.* **82** 033705
- [111] Lai K, Kundhikanjana W, Kelly M A, Shen Z-X, Shabani J and Shayegan M 2011 Imaging of coulomb-driven quantum Hall edge states *Phys. Rev. Lett.* **107** 176809
- [112] Ma E Y, Bryant B, Tokunaga Y, Aeppli G, Tokura Y and Shen Z-X 2015 Charge-order domain walls with enhanced conductivity in a layered manganite *Nat. Commun.* **6** 7595
- [113] Ma E Y, Cui Y-T, Ueda K, Tang S, Chen K, Tamura N, Wu P M, Fujioka J, Tokura Y and Shen Z-X 2015 Mobile metallic domain walls in an all-in-all-out magnetic insulator *Science* **350** 538
- [114] Ponath P *et al* 2015 Carrier density modulation in a germanium heterostructure by ferroelectric switching *Nat. Commun.* **6** 6067
- [115] Lei L *et al* 2018 Local characterization of mobile charge carriers by two electrical AFM modes: multi-harmonic EFM vs. sMIM *J. Phys. Commun.* **2** 025013
- [116] Tsai Y *et al* 2017 Tailoring semiconductor lateral multijunctions for giant photoconductivity enhancement *Adv. Mater.* **29** 1703680
- [117] Wu D *et al* 2016 Uncovering edge states and electrical inhomogeneity in MoS₂ field-effect transistors *Proc. Natl Acad. Sci. USA* **113** 8583–8
- [118] Xu R, Zheng Z Y, Ji W and Cheng Z H 2015 Advance scanning microwave microscopy *Prog. Phys.* **35** 241–56
- [119] Barber M E, Ma E Y and Shen Z-X 2022 Microwave impedance microscopy and its application to quantum materials *Nat. Rev. Phys.* **4** 61–74
- [120] Williams C C and Wickramasinghe H K 1986 Scanning thermal profiler *Appl. Phys. Lett.* **49** 1587–9
- [121] Majumdar A 1999 Scanning thermal microscopy *Annu. Rev. Mater. Res.* **29** 505–85
- [122] Lai J, Chandrachud M, Majumdar A and Carrejo J P 1995 Thermal detection of device failure by atomic-force microscopy *IEEE Electron Device Lett.* **16** 312–5
- [123] Fiege G B M, Feige V, Phang J C H, Maywald M, Gorlich S and Balk L J 1998 Failure analysis of integrated devices by scanning thermal microscopy (SThM) *Microelectron. Reliab.* **38** 957–61
- [124] Kwon O and Majumdar A 2003 Cross-sectional thermal imaging of a metal-oxide-semiconductor field-effect transistor *Microscale Thermophys. Eng.* **7** 349–54
- [125] Boroumand F A, Voigt M, Lidzey D G, Hammiche A and Hill G 2004 Imaging Joule heating in a conjugated-polymer light-emitting diode using a scanning thermal microscope *Appl. Phys. Lett.* **84** 4890–2
- [126] Luo K, Herrick R W, Majumdar A and Petroff P 1997 Scanning thermal microscopy of a vertical-cavity surface-emitting laser *Appl. Phys. Lett.* **71** 1604–6
- [127] Shi L, Plyasunov S, Bachtold A, McEuen P L and Majumdar A 2000 Scanning thermal microscopy of carbon nanotubes using batch-fabricated probes *Appl. Phys. Lett.* **77** 4295–7
- [128] Shi L, Zhou J, Kim P, Bachtold A, Majumdar A and McEuen P L 2009 Thermal probing of energy dissipation in current-carrying carbon nanotubes *J. Appl. Phys.* **105** 104306

- [129] Gomès S, Assy A and Chapuis P-O 2015 Scanning thermal microscopy: a review *Phys. Status Solidi a* **212** 477–94
- [130] Majumdar A, Lai J, Chandrachud M, Nakabeppu O, Wu Y and Shi Z 1995 Thermal imaging by atomic-force microscopy using thermocouple cantilever probes *Rev. Sci. Instrum.* **66** 3584–92
- [131] Suzuki Y 1996 Novel microcantilever for scanning thermal imaging microscopy *Jpn. J. Appl. Phys.* **35** L352–4
- [132] Luo K, Shi Z, Lai J and Majumdar A 1996 Nanofabrication of sensors on cantilever probe tips for scanning multiprobe microscopy *Appl. Phys. Lett.* **68** 325–7
- [133] Rangelow I W, Gotszalk T, Abedinov N, Grabiec P and Edinger K 2001 Thermal nano-probe *Microelectron. Eng.* **57–58** 737–48
- [134] Pytki R J, Moyer P J and West P E 1994 Scanning near-field optical microscopy and scanning thermal microscopy *Jpn. J. Appl. Phys.* **33** 3785–90
- [135] Edinger K, Gotszalk T and Rangelow I W 2001 Novel high resolution scanning thermal probe *J. Vac. Sci. Technol. B* **19** 2856–60
- [136] Zhang Y, Dobson P S and Weaver J M R 2011 Batch fabricated dual cantilever resistive probe for scanning thermal microscopy *Microelectron. Eng.* **88** 2435–8
- [137] Aigouy L, Tessier G, Mortier M and Charlot B 2005 Scanning thermal imaging of microelectronic circuits with a fluorescent nanoprobe *Appl. Phys. Lett.* **87** 184105
- [138] Aigouy L, Saidi E, Lalouat L C, Labéguerie-Egée J, Mortier M, Low P and Bergaud C 2009 AC thermal imaging of a microwire with a fluorescent nanocrystal: influence of the near field on the thermal contrast *J. Appl. Phys.* **106** 074301
- [139] Nakabeppu O, Chandrachud M, Wu Y, Lai J and Majumdar A 1995 Scanning thermal imaging microscopy using composite cantilever probes *Appl. Phys. Lett.* **66** 694–6
- [140] Chung J, Kim K, Hwang G, Kwon O, Choi Y K and Lee J S 2012 Quantitative temperature profiling through null-point scanning thermal microscopy *Int. J. Therm. Sci.* **62** 109–13
- [141] Chung J, Kim K, Hwang G, Kwon O, Jung S, Lee J, Lee J W and Kim G T 2010 Quantitative temperature measurement of an electrically heated carbon nanotube using the null-point method *Rev. Sci. Instrum.* **81** 114901
- [142] Hwang G, Chung J and Kwon O 2014 Enabling low-noise null-point scanning thermal microscopy by the optimization of scanning thermal microscope probe through a rigorous theory of quantitative measurement *Rev. Sci. Instrum.* **85** 114901
- [143] Kim K, Chung J, Hwang G, Kwon O and Lee J S 2011 Quantitative measurement with scanning thermal microscope by preventing the distortion due to the heat transfer through the air *ACS Nano* **5** 8700–9
- [144] Yoon K, Hwang G, Chung J, Kim H G, Kwon O, Kihm K D and Lee J S 2014 Measuring the thermal conductivity of residue-free suspended graphene bridge using null point scanning thermal microscopy *Carbon* **76** 77–83
- [145] Gotsmann B and Lantz M A 2013 Quantized thermal transport across contacts of rough surfaces *Nat. Mater.* **12** 59–65
- [146] Kim K, Jeong W, Lee W and Reddy P 2012 Ultra-high vacuum scanning thermal microscopy for nanometer resolution quantitative thermometry *ACS Nano* **6** 4248–57
- [147] Novoselov K, Geim A, Morozov S, Jiang D, Zhang Y, Dubonos S, Grigorieva I and Firsov A 2004 Electric field effect in atomically thin carbon films *Science* **306** 666–9
- [148] Novoselov K S, Mishchenko A, Carvalho A and Castro Neto A H 2016 2D materials and van der Waals heterostructures *Science* **353** 9439
- [149] Wang Q H, Kalantar-Zadeh K, Kis A, Coleman J N and Strano M S 2012 Electronics and optoelectronics of two-dimensional transition metal dichalcogenides *Nat. Nanotechnol.* **7** 699–712
- [150] Liu L, Kumar S B, Ouyang Y and Guo J 2011 Performance limits of monolayer transition metal dichalcogenide transistors *IEEE Trans. Electron Devices* **58** 3042–7
- [151] Xu R *et al* 2020 Atomically asymmetric inversion scales up to mesoscopic single-crystal monolayer flakes *ACS Nano* **14** 13834–40
- [152] Dai Z *et al* 2019 Mechanical responses of boron-doped monolayer graphene *Carbon* **147** 594–601
- [153] Lei L *et al* 2021 Size-dependent strain-engineered nanostructures in MoS₂ monolayer investigated by atomic force microscopy *Nanotechnology* **32** 465703
- [154] Xu R *et al* 2022 Visualization of strain-engineered nanopattern in center-confined mesoscopic WS₂ monolayer flakes *J. Phys. Chem. C* **126** 7184–92
- [155] Ahn G H, Amani M, Rasool H, Lien D-H, Mastandrea J P, Ager Iii J W, Dubey M, Chrzan D C, Minor A M and Jave A 2017 Strain-engineered growth of two-dimensional materials *Nat. Commun.* **8** 608
- [156] Pang F *et al* 2021 Strain-engineered rippling and manipulation of single layer WS₂ by atomic force microscopy *J. Phys. Chem. C* **125** 8696–703
- [157] Peimyoo N, Shang J Z, Cong C X, Shen X N, Wu X Y, Yeow E K L and Yu T 2013 Nonblinking, intense two-dimensional light emitter: monolayer WS₂ triangles *ACS Nano* **7** 10985–94
- [158] Kim M S, Yun S J, Lee Y, Seo C, Han G H, Kim K K, Lee Y H and Kim J 2016 Biexciton emission from edges and grain boundaries of triangular WS₂ monolayers *ACS Nano* **10** 2399–405
- [159] Gutierrez H R, Perea-Lopez N, Elias A L, Berkdemir A, Wang B, Lv R, Lopez-Urias F, Crespi V H, Terrones H and Terrones M 2013 Extraordinary room-temperature photoluminescence in triangular WS₂ monolayers *Nano Lett.* **13** 3447–54
- [160] Jeong H Y, Jin Y, Yun S J, Zhao J, Baik J, Keum D H, Lee H S and Lee Y H 2017 Heterogeneous defect domains in single-crystalline hexagonal WS₂ *Adv. Mater.* **29** 1605043
- [161] Ghorbani-Asl M, Borini S, Kuc A and Heine T 2013 Strain-dependent modulation of conductivity in single-layer transition-metal dichalcogenides *Phys. Rev. B* **87** 235434
- [162] Meng L, Zhang Y, Hu S, Wang X, Liu C, Guo Y, Wang X and Yan X 2016 Two dimensional WS₂ lateral heterojunctions by strain modulation *Appl. Phys. Lett.* **108** 263104
- [163] Yun W S, Han S W, Hong S C, Kim I G and Lee J D 2012 Thickness and strain effects on electronic structures of transition metal dichalcogenides: 2H-M X₂ semiconductors (M = Mo, W; X = S, Se, Te) *Phys. Rev. B* **85** 033305
- [164] Cerda E and Mahadevan L 2003 Geometry and physics of wrinkling *Phys. Rev. Lett.* **90** 074302
- [165] Vandeparre H, Piñeirua M, Brau F, Roman B, Bico J, Gay C, Bao W, Lau C N, Reis P M and Damman P 2011 Wrinkling hierarchy in constrained thin sheets from suspended graphene to curtains *Phys. Rev. Lett.* **106** 224301
- [166] Zhang D-B, Akatyeva E and Dumitrică T 2011 Bending ultrathin graphene at the margins of continuum mechanics *Phys. Rev. Lett.* **106** 255503
- [167] Pocivavsek L, Dellsy R, Kern A, Johnson S, Lin B H, Lee K Y C and Cerda E 2008 Stress and fold localization in thin elastic membranes *Science* **320** 912–6
- [168] Cai S, Breid D, Crosby A J, Suo Z and Hutchinson J W 2011 Periodic patterns and energy states of buckled films on compliant substrates *J. Mech. Phys. Solids* **59** 1094–114
- [169] Thi Q H, Wong L W, Liu H, Lee C-S, Zhao J and Ly T H 2020 Spontaneously ordered hierarchical two-dimensional

- wrinkle patterns in two-dimensional materials *Nano Lett.* **20** 8420–5
- [170] Quereda J, San-Jose P, Parente V, Vaquero-Garzon L, Molina-Mendoza A J, Agrait N, Rubio-Bollinger G, Guinea F, Roldan R and Castellanos-Gomez A 2016 Strong modulation of optical properties in black phosphorus through strain-engineered rippling *Nano Lett.* **16** 2931
- [171] Lee J, Yun S J, Seo C, Cho K, Kim T S, An G H, Kang K, Lee H S and Kim J 2021 Switchable, tunable, and directable exciton funneling in periodically wrinkled WS₂ *Nano Lett.* **21** 43–50
- [172] Nolte A J, Young Chung J, Davis C S and Stafford C M 2017 Wrinkling-to-delamination transition in thin polymer films on compliant substrates *Soft Matter* **13** 7930–7
- [173] Naumis G G, Barraza-Lopez S, Oliva-Leyva M and Terrones H 2017 Electronic and optical properties of strained graphene and other strained 2D materials: a review *Rep. Prog. Phys.* **80** 1–62
- [174] Lee C, Wei X, Kysar J W and Hone J 2008 Measurement of the elastic properties and intrinsic strength of monolayer graphene *Science* **321** 385–8
- [175] Bertolazzi S, Brivio J and Kis A 2011 Stretching and breaking of ultrathin MoS₂ *ACS Nano* **5** 9703–9
- [176] Tran Khac B-C, DelRio F W and Chung K-H 2018 Interfacial strength and surface damage characteristics of atomically thin h-BN, MoS₂, and graphene *ACS Appl. Mater. Interfaces* **10** 9164–77
- [177] Ye S *et al* 2019 Nanoscratch on single-layer MoS₂ crystal by atomic force microscopy: semi-circular to periodical zigzag cracks *Mater. Res. Express* **6** 025048
- [178] Lu C-P, Li G H, Mao J H, Wang L-M and Andrei E Y 2014 Bandgap, mid-gap states, and gating effects in MoS₂ *Nano Lett.* **14** 4628–33
- [179] Najmaei S, Lei S D, Burke R A, Nichols B M, George A, Ajayan P M, Franklin A D, Lou J and Dubey M 2016 Enabling ultrasensitive photodetection through control of interface properties in molybdenum disulfide atomic layers *Sci. Rep.* **6** 39465
- [180] Tran M D, Kim J-H, Kim H, Doan M H, Duong D L and Lee Y H 2018 Role of hole trap sites in MoS₂ for inconsistency in optical and electrical phenomena *ACS Appl. Mater. Interfaces* **10** 10580–6
- [181] Liu J, Goswami A, Jiang K, Khan F, Kim S, McGee R, Li Z, Hu Z, Lee J and Thundat T 2018 Direct-current triboelectricity generation by a sliding Schottky nanocontact on MoS₂ multilayers *Nat. Nanotechnol.* **13** 112–6
- [182] Kim S, Kim T Y, Lee K H, Kim T-H, Cimini F A, Kim S K, Hinchet R, Kim S-W and Falconi C 2017 Rewritable ghost floating gates by tunnelling triboelectrification for two-dimensional electronics *Nat. Commun.* **8** 15891
- [183] Burgo T A D L, Rezende C A, Bertazzo S, Galembeck A and Galembeck F 2011 Electric potential decay on polyethylene: role of atmospheric water on electric charge build-up and dissipation *J. Electrostat.* **69** 401–9
- [184] Galembeck F, Burgo T A L, Balestrin L B S, Gouveia R F, Silva C A and Galembeck A 2014 Friction, tribochemistry and triboelectricity: recent progress and perspectives *RSC Adv.* **4** 64280–98
- [185] Ding S, Xiao X, Liu S, Wu J, Huang Z, Qi X and Li J 2019 Detection of interfacial charge transfer in MoS₂/PbI₂ heterostructures via Kelvin probe force microscope *Appl. Phys. A* **125** 287
- [186] Bediako D K, Rezaee M, Yoo H, Larson D T, Zhao S Y F, Taniguchi T, Watanabe K, Brower-Thomas T L, Kaxiras E and Kim P 2018 Heterointerface effects in the electrointercalation of van der Waals heterostructures *Nature* **558** 425–9
- [187] Mertens S F, Hemmi A, Muff S, Groning O, De Feyter S, Osterwalder J and Greber T 2016 Switching stiction and adhesion of a liquid on a solid *Nature* **534** 676
- [188] Ducke J, Riss A, Paz A P, Seufert K, Schwarz M, Garnica M, Rubio A and Auwärter W 2018 Layered insulator/molecule/metal heterostructures with molecular functionality through porphyrin intercalation *ACS Nano* **12** 2677–84
- [189] Al Balushi Z Y *et al* 2016 Two-dimensional gallium nitride realized via graphene encapsulation *Nat. Mater.* **15** 1166–71
- [190] Lee H, Ko J-H, Song H C, Salmeron M, Kim Y-H and Park J Y 2018 Isotope- and thickness-dependent friction of water layers intercalated between graphene and mica *Tribol. Lett.* **66** 36
- [191] Hong Y, Wang S, Li Q, Song X, Wang Z, Zhang X, Besenbacher F and Dong M 2019 Interfacial icelike water local doping of graphene *Nanoscale* **11** 19334–40
- [192] Velasco-Velez J-J, Wu C H, Pascal T A, Wan L F, Guo J, Prendergast D and Salmeron M 2014 The structure of interfacial water on gold electrodes studied by x-ray absorption spectroscopy *Science* **346** 831–4
- [193] Dollekamp E, Bampoulis P, Siekman M H, Kooij E S and Zandvliet H J W 2019 Tuning the friction of graphene on mica by alcohol intercalation *Langmuir* **35** 4886–92
- [194] Zhang Y, Zhu W, Hui F, Lanza M, Borca-Tasciuc T and Muñoz Rojo M 2019 A review on principles and applications of scanning thermal microscopy (SThM) *Adv. Funct. Mater.* **30** 1900892
- [195] Hwang G and Kwon O 2016 Measuring the size dependence of thermal conductivity of suspended graphene disks using null-point scanning thermal microscopy *Nanoscale* **8** 5280–90
- [196] Menges F, Riel H, Stemmer A, Dimitrakopoulos C and Gotsmann B 2013 Thermal transport into graphene through nanoscopic contacts *Phys. Rev. Lett.* **111** 205901
- [197] Yalon E *et al* 2017 Temperature-dependent thermal boundary conductance of monolayer MoS₂ by raman thermometry *ACS Appl. Mater. Interfaces* **9** 43013–20
- [198] Yasaei P *et al* 2017 Interfacial thermal transport in monolayer MoS₂ — and graphene-based devices *Adv. Mater. Interfaces* **4** 1700334
- [199] Chen Z, Jang W, Bao W, Lau C N and Dames C 2009 Thermal contact resistance between graphene and silicon dioxide *Appl. Phys. Lett.* **95** 161910
- [200] Evangeli C, Spiece J, Sangtarash S, Molina-Mendoza A J, Mucientes M, Mueller T, Lambert C, Sadeghi H and Kolosov O 2019 Nanoscale thermal transport in 2D nanostructures from cryogenic to room temperature *Adv. Electron. Mater.* **5** 1900331
- [201] Yasaei P, Murthy A A, Xu Y, Dos Reis R, Shekhawat G S and Dravid V P 2019 Spatial mapping of hot-spots at lateral heterogeneities in monolayer transition metal dichalcogenides *Adv. Mater.* **31** 1808244